MICRO/NANO-MECHANICAL STUDY OF DEFORMATION MECHANISMS AND STRUCTURE IN AMORPHOUS METAL

JIFANG ZENG

Ph.D

The Hong Kong Polytechnic University

2013

The Hong Kong Polytechnic University

Department of Mechanical Engineering

Micro/nano-Mechanical Study of Deformation Mechanisms and Structure in Amorphous Metal

Jifang Zeng

A thesis submitted in partial fulfillment of the requirements for

the degree of Doctor of Philosophy

September 2012

CERTIFICATE OF ORIGINALITY

I hereby declare that this thesis is my own work and that, to the best of my knowledge and belief, it reproduces no material previously published or written, nor material that has been accepted for the award of any other degree or diploma, except where due acknowledgement has been made in the text.

_____(Signed)

ZENG Jifang (Name of student)

Dedication

This dissertation is dedicated with love to my mother, father and younger brother, who always support my research studies and brings the greatest joy and encouragement into my life.

Abstract

In this thesis, micro- and nano-mechanical experiments combined with theoretical analyses were performed to investigate the mechanical heterogeneity in metallic glasses (MGs). Firstly, the anelastic deformation of MGs at ambient temperature was studied through spherical nanoindentation. The anelastic deformations in MGs were successfully revealed experimentally before shear banding occurs at room temperature. A general rheological model was proposed to rationalize the experimental results. Through the fitting of the experimental data to the model, we are able to quantify the structural inhomogeneity intrinsic to MGs in terms of local modulus and viscosity. The outcome of this investigation provides an important insight into the structure-property relation in MGs, and also shed light on the overall atomic packing in them.

Secondly, we developed an experimental scheme to investigate the structural and mechanical origin of shear-banding-induced softening in a Zr-based BMG. Three BMG plates were plastically bent to different curvatures by using the mandrels of different diameter. The Young's modulus was measured via the Joslin-Oliver based Berkovich nanoindentation approach at a spatially resolved scale, of which the magnitudes remain nearly at a constant across the width of the BMG bent bars; in contrast, the hardness varies with the indentation location. As compared to the hardness measured before bending, the post-bending hardness is reduced significantly on the compressive side of the bend bars while remains almost unchanged on the tensile side. Interestingly, from the compression of micropillars, we didn't find any prominent change of the yield strengths and moduli of the BMG bend bars regardless of the pillar location.

These findings suggest that residual stress plays a vital role in the plasticity-induced softening in the BMGs.

In the last part of my thesis, we present our recent findings obtained through the high-resolution atomic force microscopy (HRAFM) on the evolution of the nanoscale structures in a metallic glass (MG) thin film. To reach the unprecedented spatial resolution of ~ 1nm, we have developed an experimental scheme to correct the possible AFM artifacts arising from surface adhesion and topography. After that, we systematically investigated the fractal growth of the dense-packing phases during the atomic packing evolves in an annealed Zr-Ni MG thin film. Through our HRAFM experiments, the annealing process of MGs was found to be associated with a fractal growth of some dense-packing phases. Based on these findings an important implication can be drawn that, with decreasing the cooling rate, the atomic structure of MGs become denser with a fractal packing of dense-packing phases. This fractal packing of the dense-packing phases constitutes the major overall structure feature of MGs and might dictate their structural revolution when subjected to mechanical deformation.

List of Publications

1. Yang Y, **Zeng JF**, Ye JC, Lu J. Structural inhomogeneity and anelastic deformation in metallic glasses revealed by spherical nanoindentation. Appl. Phys. Lett. (2010) vol. 97 (26) pp. 261905
2. Y. Yang, **J.F. Zeng**, A. Volland, J.J. Blandin, S. Gravier, C.T. Liu. Fractal growth of the dense-packing phase in annealed metallic glass imaged by high-resolution atomic force microscopy. Acta Materialia (2012)vol.60 pp.5260-5272
3. **J.F. Zeng**, J.P. Chu, Y.C. Chen, G. Sebastien, Y. Yang. Nano-scale Structural Mapping of Thin Film Metallic Glass with Dynamic Atomic Force Microscopy. Thin Solid Films, (2013) (submitted)

Acknowledgements

Firstly, I would like to express my great appreciation to my chief supervisor Prof. Sanqiang Shi, who gave me great help during the important stage of my study in the Hong Kong Polytechnic University. Meanwhile, sincere appreciation goes to my co-supervisor Dr. Yong Yang for his constant guidance, encouragement and providing many chances to improve my research abilities in the past three years. I am so grateful to my another co-supervisor Prof. C. T. Liu and collaborators, Dr. Jianchao Ye and Mr. Hao Jiang, Song Wang from the department of mechanical engineering, the Hong Kong Polytechnic University, Dr. Qing Wang, Long Liu, Seng Guo from the department of mechanical and Biomedical Engineering, City University of Hong Kong.

Next, I wish to thank the technicians: Mr. Ng, in Department of Mechanical Engineering, Mr. M.N. Yeung and Hardy in the Materials Research Center of the Hong Kong Polytechnic University, and the staffs in the Electron Microscope Unit of the Hong Kong University including Frankie, Amy, who provided technical supports to my research.

I also want to take this opportunity to express my deepest appreciation to my family. Besides, I am deeply indebted to my friends: Mr. Hao Xu, Edward Cheuk, Peter Zhang, Harry Wu, Jiangang Chen and his wife, Stephen JP, Prof. Yifan Han et al., who gave me a lot of help and enjoyed the wonderful days over the past years in Hong Kong. At last, I am extremely grateful to my bosom friends.

Abbreviations

2-D	Two-Dimensional
AFM	Atomic Force Microscopy
AM	Amplitude-Modulation
BMG	Bulk Metallic Glass
BMGs	Bulk Metallic-Glasses
CRN	Continuous Random Network
DAFM	Dynamic Atomic Force Microscopy
DLA	Diffusion Limited Aggregation
DLC	Diamond-Like Carbon
DRPHS	Dense Random Packing of Hard Spheres
DSC	Differential Scanning Calorimetry
ECP	Efficient Cluster Packing
EXAFS	Extended X-ray Absorption Fine Structure Spectroscope
FIB	Focused Ion Beam
HRAFM	High-Resolution Atomic Force Microscopy
HRTEM	High-Resolution Transmission Electron Microscopy
MC	Monte Carlo
MD	Molecular Dynamics
MG	Metallic Glass
MGs	Metallic Glasses
MRO	Medium Range Order

NMR	Nuclear Magnetic Resonance
PAS	Positron Annihilation Spectroscopy
PEL	Potential Energy Landscape
RMC	Reverse Monte-Carlo
RMS	Root-Mean-Square
RSP	Rapid Solidification Processing
SADPs	Selective Area Diffraction Patterns
SANS	Small Angle Neutron Scattering
SAXS	Small Angle X-ray Scattering
SEM	Scanning Electron Microscopy
SRO	Short Range Ordering
STZ	Shear Transformation Zone
SYS	Stone-Yoder-Sproul
TEM	Transmission Electron Microscopy
TFMGs	Thin Film Metallic-Glasses
TM-metalloid	Transition-Metal-metalloid
XRD	X-Ray Diffraction

Contents

List of Tables

List of Figures

1 Literature Review

1.1 History of Bulk Metallic Glass

The first reported metallic glass ($Au_{75}Si_{25}$) was synthesized by W. Klement (Jr.), Willens and Duwez at the California Institute of Technology in 1960. At that time, the cooling rate was extremely large (not less than 10^6 K/s) to solidify the glassy state, and the forms of these metallic glasses were limited to ribbons, foils or wires (Klement W., Willens R. H. et al. 1960).

In 1969, $Pd_{77.5}Cu_6Si_{16.5}$ was synthesized successfully with a critical cooling rate between 100 and 1000 K/s. But the origins of BMGs go back to 1974, when Chen (Chen H.S. 1974) produced different ternary BMGs with the compositions of $(Pd_{1-x}M_x)_{0.835}Si_{0.165}$ (M stands for Fe, Co, Ni, Cu, Ag and Au), Pt-Ni-P and Pd-Ni-P in the form of rod, 1-3mm in diameter and several centimeters in length.

In the early 1980s, $Pd_{55}Pb_{22.5}Sb_{22.5}$ glassy ingots were produced with (A. Peker 1993; Angell 1995; Egami 1997; H. W. Sheng 2006) the diameter of 5mm by surface etching and heating-cooling cycles. In the late 1980s, the RSP (rapid solidification group) group at Tohoku University in Sendai, Japan, performed a systematical investigation on the glass-forming ability of different alloy systems and successfully obtained BMGs in some of the systems at the solidification rates of 10^3K/s or lower. In 1988, alloys of lanthanum, aluminium, and copper were found to be highly glass-forming (Oscar Belart Bayo 2008).

In 1992, Peker and Johnson synthesized the first commercial amorphous alloy, Vitreloy 1 (41.2% Zr, 13.8% Ti, 12.5% Cu, 10% Ni, and 22.5% Be), in 14mm diameter at Caltech, as a part of Department of Energy and NASA research of new aerospace materials. Since then, there is an explosion in the BMG research all over the world and 'tons' of publications can be found in the literature during that period (A. Peker and W. L. Johnson 1993; C. A. Angell 1995; A. Inoue, N. Nishiyama et al. 1996; A. Inoue, T. Zhang et al. 1997; T. Egami 1997; W. L. Johnson 1999; B. L. Shen, H. Koshiba et al. 2000; H. Habazaki, H. Ukai et al. 2001).

1.2 Structural Model

The structure of amorphous alloys or metallic glasses is different from that of crystalline metals which can be distinctively characterized by several parameters (lattice type, parameter and so on). Therefore, it has been remaining as a hot topic to understand the structure of metallic glasses with their emergency. Nowadays, the most common used methods for the structural investigation of metallic glasses are: X-Ray Diffraction (XRD), Transmission Electron Microscopy (TEM), High-Resolution Transmission Electron Microscopy (HRTEM), Small Angle Neutron Scattering (SANS), Small Angle X-ray Scattering (SAXS), Positron Annihilation Spectroscopy (PAS), Nuclear Magnetic Resonance (NMR), molecular dynamics simulations and so on. In this section, a brief introduction for some structural models of amorphous alloys is presented.

1.2.1 Model of Dense Random Packing of Hard Spheres (DRPHS)

The dense random packing of hard sphere model was the first proposed to describe the structure of non-crystalline alloys. In this model, the nature of structural amorphousness is interpreted as the gathering of some homogeneous, continuous, dense-packed, disordered and random atomic

hard spheres. Here "randomness" means that there is no long-range translational and orientational order in the metallic bonds while "dense-packing" suggests that the atoms are arranged too dense to have an adequate space for another hard sphere. The correlation of two spheres is weak when their distance is larger than five times of their average diameter.

In the early 1960's, J.D. Bernal (Bernal J. D. 1959; J. D. Bernal 1960) used steel balls with the same diameter to simulate the structure of a liquid. Afterwards, M.H. Cohen et al. (M. H. Cohen and Turnbull 1961) adopted the same model to describe the structure of non-crystalline metals. The procedure of building this model is listed as below:

1. put the steel balls into the container with irregular or soft walls;

2. shake or compress the container to condense the steel balls;

3. fix the balls and remove them one by one; and

4. measure the coordinate of each ball center and then calculate the radial distribution function, density and so on.

Bernal (Bernal 1959) suggested that the structure of dense random packing was composed of five kinds of polyhedrons, which were named as Bernal polyhedron and shown in Fig. 1.1. Among the five polyhedrons, those shown in Figs. 1.1 (c), (d) and (e) were thought to be the unique structural cells in non-crystalline alloys, because the implicit incorporation of pentagon into these cells frustrates any long range ordering. Apart from Bernal, Scott (G. D. Scott 1960), Cohen and Turnbull (Cohen M. H. and Turnbull D 1964) also believed that the DPRHS model can be adapted to describe the structure of a hypothetical non-crystalline alloy.

To improve the DRPHS model, Sadoc et al. (Sadoc J. F., Dixmier J. et al. 1973) constructed a local heterogeneous structure by introducing icosahedrons into the model. Connel (Connel G.A.N. 1975) found that the weak potential of atomic interaction was the cause for the obvious movement of radial distribution function, when he selected the compressible soft spheres to constitute the amorphous structure.

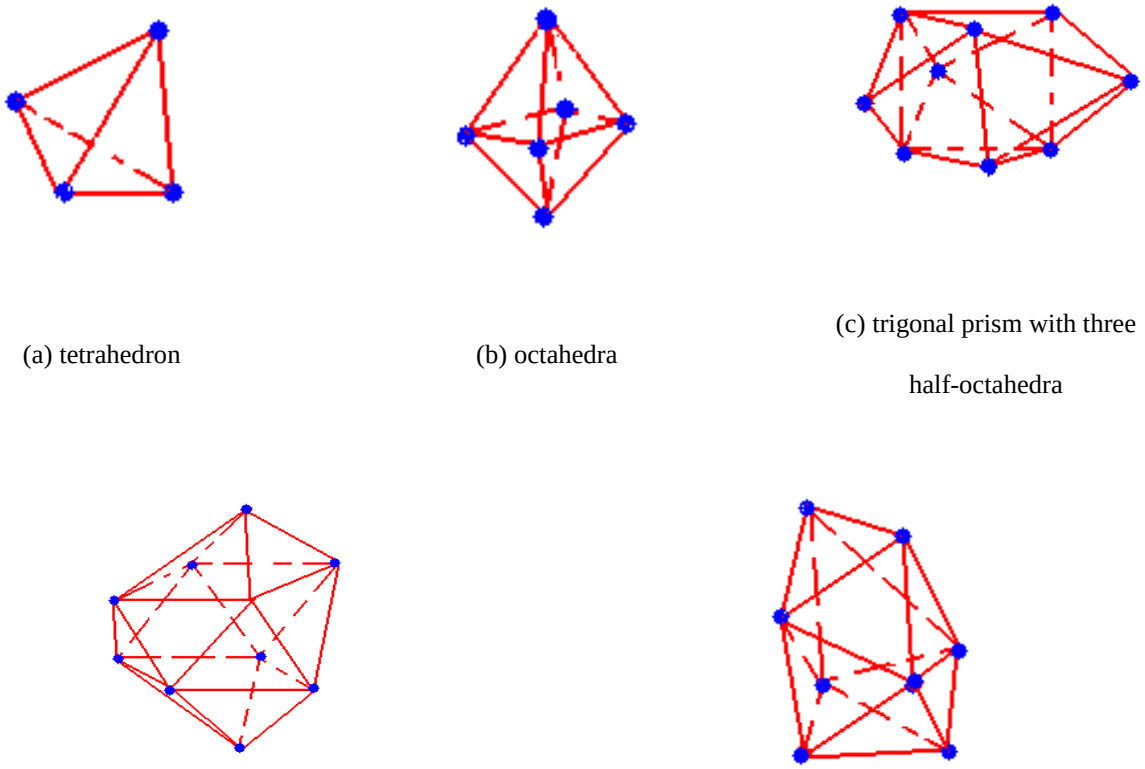

(a) tetrahedron

(b) octahedra

(c) trigonal prism with three half-octahedra

(d)Archimedes prism with two half-octahedra

(e) Quads dodecahedron

Figure 1.1 Schematic drawing of Bernal polyhedron

1.2.2 Micro-crystal Model

The micro-crystal model was proposed by Bragg et al. (G.S. Cargill 1970). In this model, the amorphous alloy was composed of very tiny micro-crystal (about ten or a few tens angstrom). So the short range order of the micro-crystalline was the same with the crystalline and the long range disorder was the results of the random distribution of the micro-crystals. But the disadvantage of this model is that it is invalid to clearly describe the distribution of the atomic arrangements in a grain boundary. Meanwhile, the radial distribution function (or pair correlative function) calculated by this model quantitatively disagrees with experimental results.

1.2.3 Continuous Random Network Model (CRN)

In the CRN model, the balls are used to represent the atoms and connected by the rod. The number of rod connected to the ball is equal to the atomic valence, the length of the rod stands for the bond distance. The separation angle between any two adjacent rods stands for the bond angle. The network made up of these balls and rods can continually fill the space without forming crystalline long-range periodicity.

Polk (D.E. Polk 1971) manually built a CNR model to simulate the atomic distribution of non-crystalline silica (α-Si) and germanium (α-Ge) in1971 and obtained some promising results. Since then on, the CRN model has been improved and accepted to describe the structure of non-crystal semiconductor. In particular, with the aid of super-computers, additional dynamic features, such as structural relaxation, have been added to refine this model.

In the framework of CRN model, P. H. Gaskell (P. H. Gaskell 1978) came up with an idea in 1978 that local structures in a glass were crystal like. From this idea, the unit cell of a non-crystal was regarded as similar to the Si-O tetrahedron and these tetrahedrons connected randomly to form a non-crystal network. Figure 1.2 is the sketch of this model; (a) shows the coordination of conventional triangular prism and (b) is for a edge-sharing of polyhedrons observed in the Fe_3C.

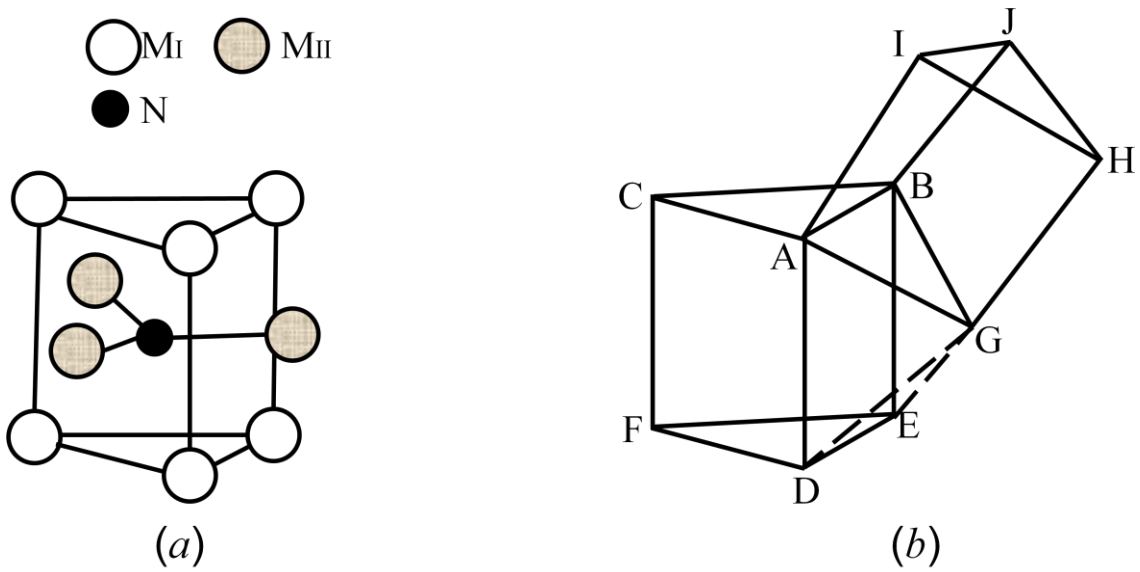

Figure 1.2 (a) Regular trigonal prismatic coordination; and (b) edge-sharing of polyhedral observed in the Fe_3C, cementite structure. Note that the M_I atom G for the upper prism occupies an M_{II} site in relation to lower prism(P. H. Gaskell 1978).

Dubois (Dubois J. M., Gaskell P. H. et al. 1985; Dubois J. M., Gaskell P. H. et al. 1985) brought forth the non-crystal structural model based on the chemical twins theory. The starting point of this model is the location-correlation domain structure of 1~2nm in the non-crystalline. Within each domain, a single type of structural operation (simple chemical twinning) acting in a

prescribed direction governs positional order. But positions of atoms in the interface between domains are determined by at least two operations which are appropriate to each of the bounding domains. As a result of above rules, the structure configuration is highly homogeneous. For a number of typical amorphous transition-metal-metalloid (TM-metalloid) alloys, computed properties from this model agree well with experimental structural data. In addition, a well agreement also appears between experimental and calculated partial pair-correlation functions and structure factors, proven the existence of extensive local and medium-range positional order in these alloys. But the discrepancies between model data and experimental results show that the model is less ordered than a real glass. In a word, this model also shed light on the nature of local geometrical distortions of structural units, coupling between positional and compositional fluctuations and the relative stability of glassy and microcrystalline alloys.

1.2.4 FCC\HCP Close-packed Cluster Model

In 2004, Miracle D. B. (D.B. Miracle 2004) proposed a model by putting solute-centered atomic clusters to the lattice point similar to that in a crystal for characterizing the structure and topology of metallic glasses, which was named as close-packed cluster model or efficient cluster packing (ECP) model since then. In the inter-cluster regions, solvent-rich noncrystalline structures were arranged to fill the space. He used this model to build binary and ternary metallic glass structures. The advantage of this model is that it does not only consider the atoms of the 1^{st} nearest shell, but also include those of the 2^{nd} and even 3^{rd} nearest shells. Figure 1.3 is the illustration of close-packed cluster model constituted by a single cluster unit. From the above explanation, the middle range order in the amorphous alloys can be described with the crystalline

method. In the below figure, the atomic arrangement is $\alpha - \Omega - \beta - \Omega - \alpha, \alpha - \Omega - \alpha - \Omega - \alpha$ and $\alpha - \Omega - \gamma - \Omega - \beta - \Omega - \beta - \Omega - \alpha$ in the atomic direction <100>, <110> and <111>.

Miracle D. B. summarized his dense cluster-packing model by these features: (i) efficiently packed solute-centred atomic clusters with solvent atoms only in the first coordination shell are densely packed to form a structure of overlapping clusters; (ii) three topologically distinct solutes exist: primary cluster-forming solutes (α), cluster-octahedral solutes (β) and cluster-tetrahedral solutes (γ); (iii) all solutes posses radius ratios relative to the solvent, R^*, that enable efficient atomic packing in the first coordination shell; (iv) face-sharing of adjacent clusters is preferred to minimize volume, but edge- and vertex-sharing may exist to reduce internal strains; (v) solutes with atomic radii within ±2% of one another are considered topologically equivalent; and (vi) no orientational order exists between clusters.

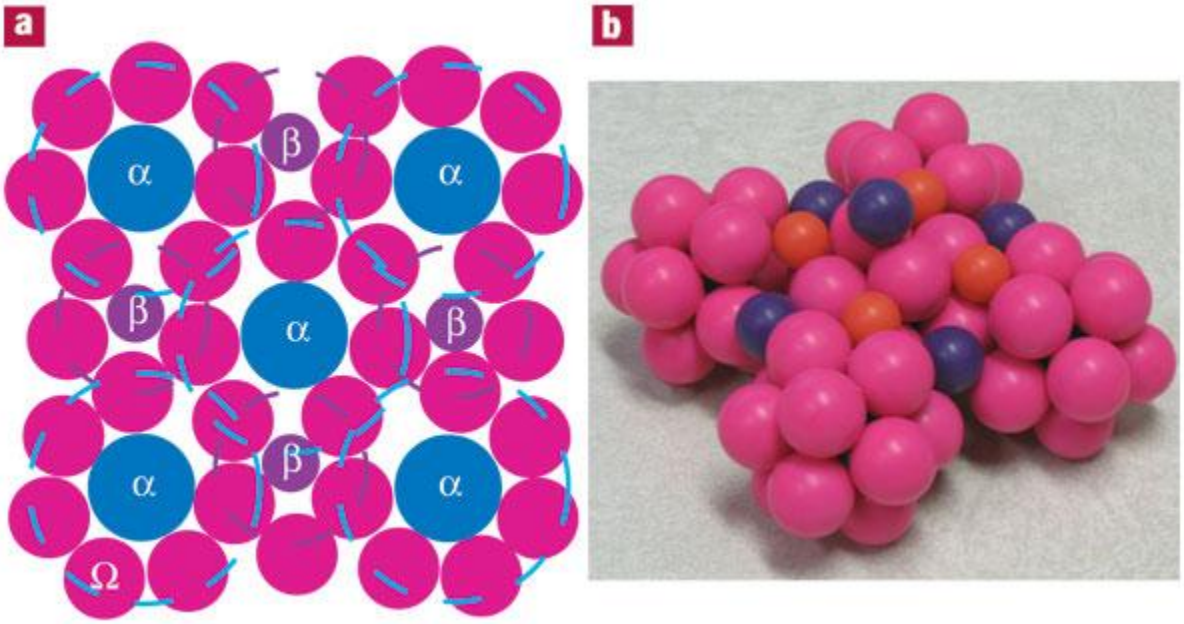

Figure 1.3 Illustrations of portions of a single cluster unit cell for the dense cluster packing model. (a), A two-dimensional representation of a dense cluster-packing structure in a (100) plane of clusters illustrating the features of interpenetrating clusters and efficient atomic packing around each solute. Relaxations outside the plane of view cannot be shown in this two-dimensional representation. (b), A portion of a cluster unit cell of a <12-10-9> model system representing a Zr-(Al,Ti)-(Cu,Ni)-Be alloy. The α sites are occupied by blue spheres, the β sites are occupied by purple spheres and the γ sites are occupied by orange spheres. Pink Zr solvent spheres form relaxed icosahedra around each ∝solute. There is no orientational order amongst the icosahedral clusters (D.B. Miracle 2004)

In this topological model, the short range ordering (SRO) clusters are packed together in an FCC/HCP arrangement resulting in the greatest packing density with accounting for the medium range order (MRO) in some alloys. This model is successful in the prediction of glass forming compositions. Meanwhile, the idea of packing clusters in efficient configurations had been proven experimentally. The disadvantage of this model is that there is no consideration in the chemical interactions and the atoms are considered as hard spheres with soft inter-atomic potentials.

Although this model shows the atomic dense-packing arrangement just qualitatively. In this model, the shared atoms of clusters are disorder in the atomic structure of FCC/ HCP unit cell and the exact atom position is not calculated quantitatively.

Based on the above, this model is a qualitative one to describe atomic dense arrangement. During the configuration, the location of shared atoms between clusters is disorder, according FCC or HCP unit cell. The limitation of this model is that the location of these atoms is not quantitatively defined.

1.2.5 Quasi-equivalent Cluster Model

Through the use of synchrotron radiation techniques and first-principles molecular dynamics simulations, Sheng and E. Ma (H. W. Sheng, W. K. L UO et al. 2006) proposed a new structural model for TM-metalloid, TM-TM and metal-TM. Figure 1.4 shows the structural feature of the $Ni_{80}P_{20}$ metallic glass obtained by the extended X-ray absorption fine structure spectroscope (EXAFS) and reverse Monte-Carlo (RMC) simulation. This figure shows that the EXAFS of simulation agrees with the experimental EXAFS.

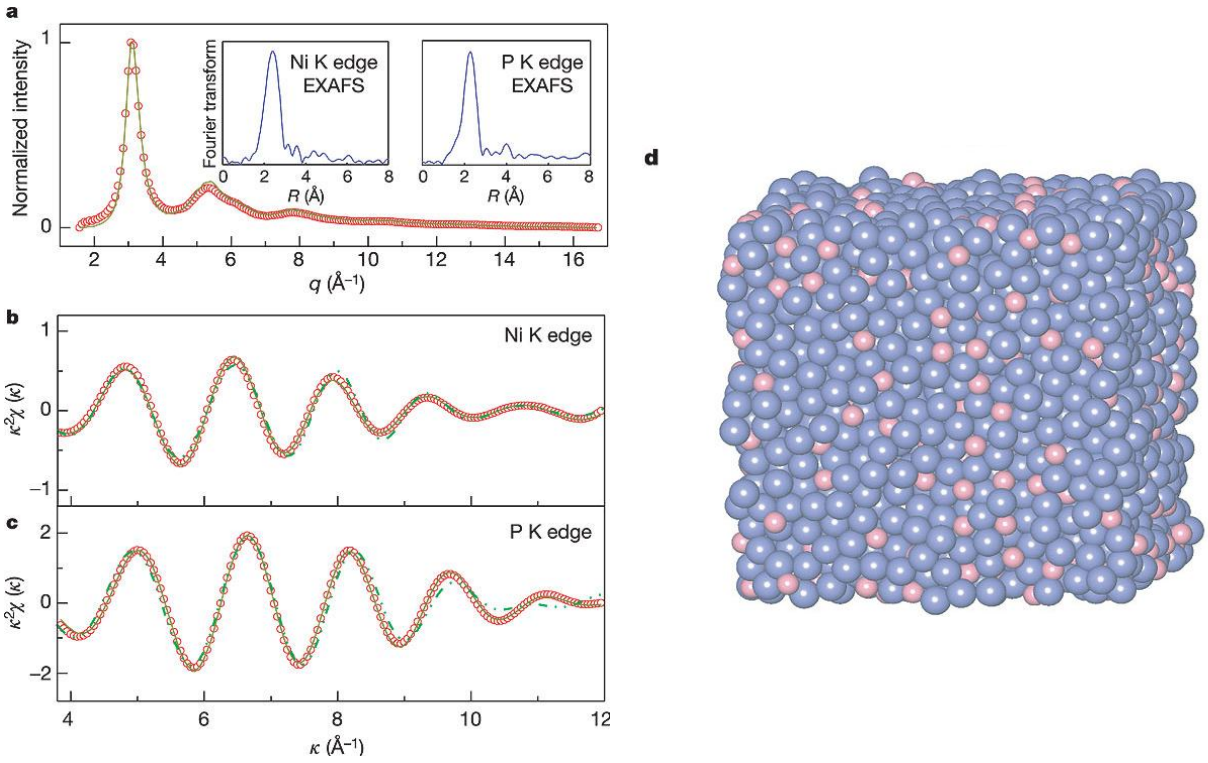

Figure 1.4 Reverse Monte Carlo modeling to reproduce the experimental X-ray diffraction and absorption data. (a), Solid lines are the experimental XRD and Fourier-transformed EXAFS spectra for the $Ni_{80}P_{20}$ amorphous alloy. The circles are for the XRD pattern calculated for the eventual RMC configuration. (b), (c), the solid lines present the inverse Fourier transforms of the first peaks in the Fourier-transformed EXAFS data in a. $\chi(\chi)$ is the EXAFS, where χ is the photoelectron wave vector. R is the distance between atoms. The EXAFS spectra calculated for the RMC configuration (circles) and for the *ab* initio molecular dynamics configuration (green line) are in good agreement with the experimental data. (d), A view of the final RMC configuration. The blue and pink balls represent Ni and P atoms, respectively (H. W. Sheng, W. K. L UO et al. 2006).

1.2.6 Tight-bond Cluster Model

In 2006, C. Fan et al. (C. Fan, P. K. Liaw et al. 2006; C. Fan 2009) proposed the tight-bond cluster model to consider shear transformation zone (STZ) activation controlled by the co-

operative shearing of individual atoms. This model composed of three distinct parts: tightly bound clusters with small atomic separation distances, free volume regions between clusters and interconnecting zones between the clusters, illustrated in Fig.1.5 suggests that it is the rearrangement of critical clusters. In this model, mechanical deformation is controlled by the rotation of SRO clusters (loosely bonded in comparison to strong bonds within the cluster). Free volume in this model is considered as accommodated between clusters rather than within them. The limitation of this model is that this conceptual model does not give specifics of cluster rearrangement under shear and without considering the sharing of atoms between clusters.

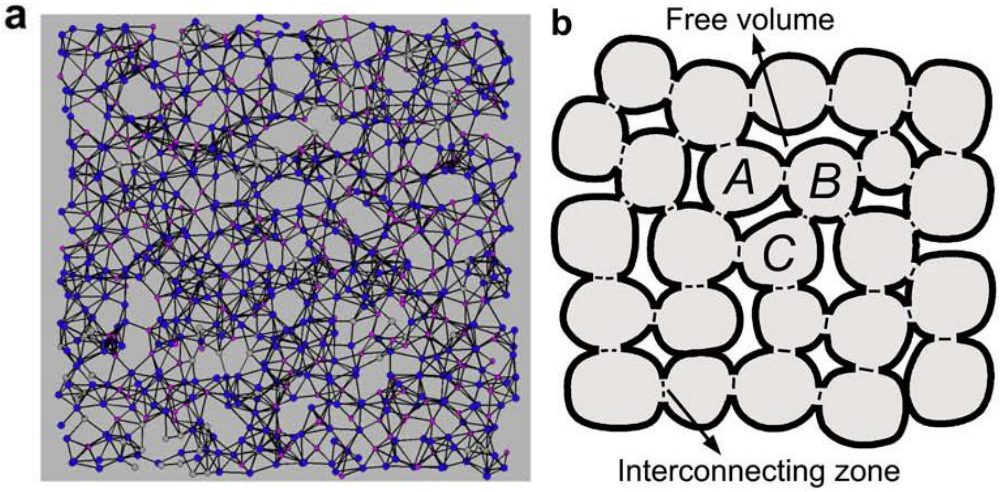

Figure 1.5 (a) A layer inside the rebuilt three-dimensional atomic structure (icosahedral cell thickness) by RMC simulations for as-cast $Zr_{55}Cu_{35}Al_{10}$ BMG (blue: Zr, pink: Cu and gray: Al); (b) tightly bonded clusters randomly and tightly connected to each other by interconnecting zones (dashed lines) and separated by free volume at $T < T_g$ (C. Fan, P.K. Liaw et al. 2009)

1.2.7 Core-shell Model

The core-shell model (J. C. Ye, C. T. Liu et al. 2010) was developed based on the observation of strain hysteresis during the compression of nanopillars. The cluster density of "cores" is much

lower than the “shell” and the “cores” is surrounded by an elastic “shell”. The deformation of metallic glass is the summation of the response from the “soft” core and “hard” shell. The sketch of this model is shown in the following figure.

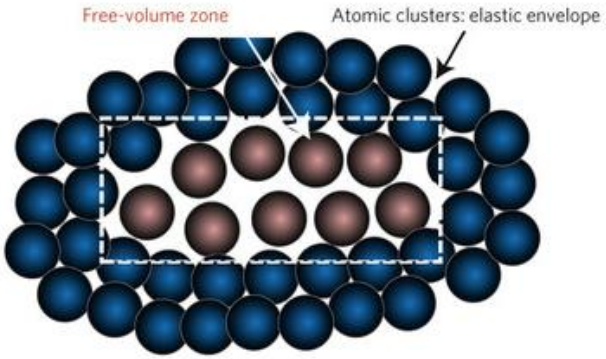

Figure 1.6 Sketch of the core–shell atomistic model in metallic glasses (J. C. Ye, C. T. Liu et al. 2010)

Based on the combination of XRD and reverse Monte Carlo, X. J. Liu et al. (X. J. Liu, G. L. Chen et al. 2008) extrapolated the 3-D structure of the atomic structure of BMGs and their results were presented in the following figure. Their results confirmed that regions containing a high and low density of free volume co-exist and the core-shell model is reasonable to explain the deformation of metallic glass in a certain degree.

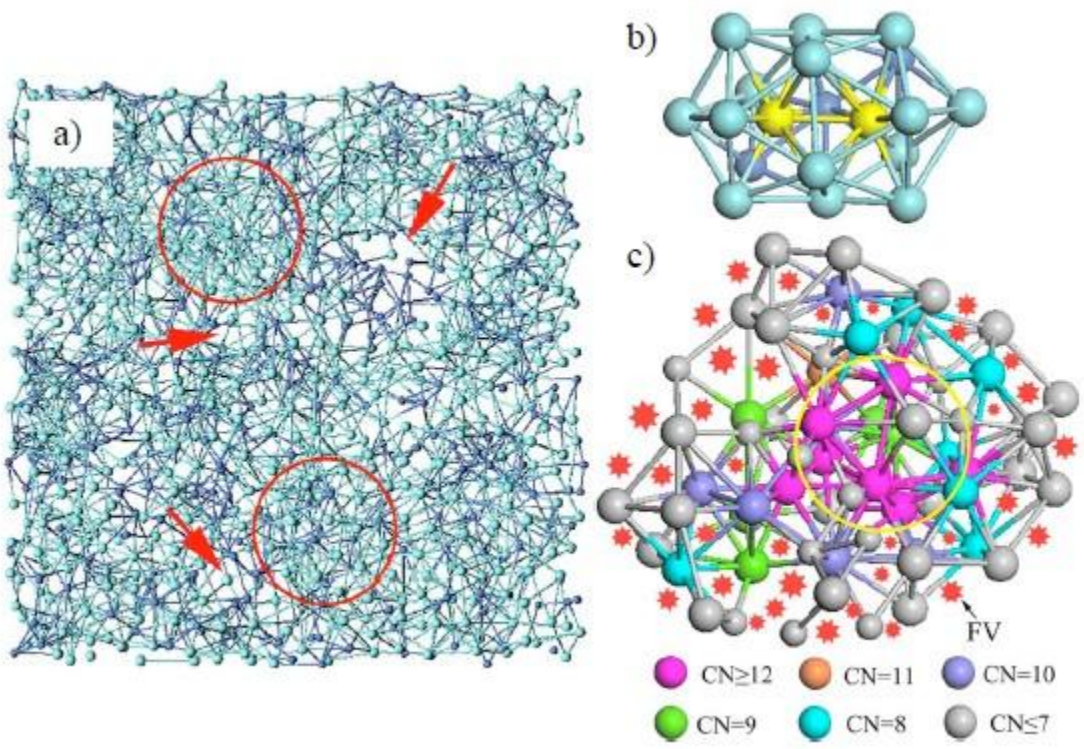

Figure 1.7 Reverse Monte Carlo generated 3-D atomistic structure of a model Zr2Ni metallic glass. a) regions high and low in free volume are indicated by arrows and circles respectively, b) an MRO cluster, and c) a dense packed unit with an MRO cluster at the centre (circled region), where the red stars are free volume sites (X. J. Liu, G. L. Chen et al. 2008).

1.3 Deformation Mechanism

The absence of sharp Bragg peaks in diffraction experiments constitutes the prominent feature characteristic of the amorphous alloys; however, more structural details are needed to understand the deformation mechanisms in amorphous materials. For metallic glasses, these further structural details include the local ordered structures, such as the short- and medium-range order (SRO & MRO), which originate from the clustering of dense-packing atoms and can be revealed

by static means, such as X-ray or neutron diffraction(Cang Fan, P. K. Liaw et al. 2006; D. Ma, A.D. Stoica et al. 2009; W. Dmowski, T. Iwashita et al. 2010) and high-resolution transmission electron microscopy (TEM) (Akihiko Hirata, Pengfei Guan et al. 2010) and the local disordered structures, such as the proposed free-volume and shear transformation zone (STZ).

1.3.1 Free volume Theory

The free volume theory was first proposed by Turnbull and Cohen (M. H. Cohen and Turnbull 1959) for liquid and then extended by Spaepen (Spaepen 1977) for metallic glasses. The definition of free volume in Turnbull and Cohen's theory was the open space or volume having the size approximately equal to that of the basic structural unit. Once this space reaches a critical value, a defect forms and thereby it requires no or just little energy in addition to thermal fluctuation for moving atoms in and out of this space. As a result, the existence of these open spaces or free volume can lead to atomic diffusion and flow. However, the size of the so-called free volume was measured to be about 10% of the atomic volume for metallic glasses (J. M. Ziman 1961). So the probability for an atom to have a free volume with a size between ν and ν + *d*ν is:

$$p(v)dv = \frac{v_f}{\gamma} exp\left(-\frac{\gamma v}{v_f}\right) \tag{1.1}$$

Where γ is a constant of the order of unity that takes into account overlap of free volume between neighboring atoms and v_f is the average free-volume per atom. Then, the diffusivity is given as:

$$D = D(v^*)\int_{v^*}^{\infty} p(v)\,dv = D(v^*)\exp\left(-\frac{\gamma v^*}{v_f}\right) \tag{1.2}$$

Here γ is a constant of order of unity. Different with crystalline, the structure and volume of MGs is high temperature dependent. The changes in the structure with temperature change increase quicker when temperature is above glass transition temperature T_g, compared with them below T_g. So, annealing the MGs below T_g is a slowly structural relaxation process, from an higher metastable energy state towards an lower one with a decrease of free volumes and correlated topological and chemical changes. Annealing below T_g of a Zr-Ni thin film is discussed in details in chapter 5.

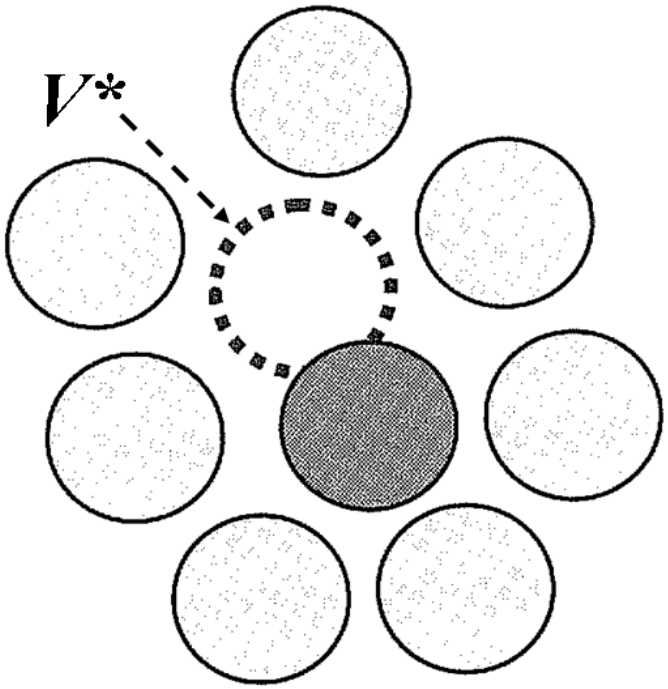

Figure 1.8 Schematic representation of free volume for an atom to move into. v^* is marked in the figure.

Because of the fast cooling procedure for the metallic glass synthesis, the atoms in the metallic liquid were frozen and there is no crystalline structure to be generated. The content of free volume is related to the cooling rate. The faster the cooling rate used the more free volume included. Meanwhile, if the metallic glass is annealed, the content of free volume is reduced as a result of the structure relaxation.

1.3.2 Shear Transformation Zone Theory

The theory of shear transformation zones (STZ) was developed by Ali Argon(A.S. Argon 1979; A.S. Argon and H.Y. Kuo 1979) based on the bubble shaft experiments . Argon used the term "shear transformation zone" to describe the metallic glass deformation with a mathematic formalism similar to the free volume theory developed by Frans Spaepen (F. Spaepen 1977). The STZ theory was based on the following assumptions:

A: the localize defects in the metallic glass are STZs which can undergo stress induced transformation by releasing the elastic energy;

B: these defects have an orientation which is determined by the stress. This stress is most properly to induce the transformation of the STZ.

C: the STZs are inherently two-state systems. Once an STZ transforms, transformation cannot be activated in the same direction but a reverse transformation is allowed;

D: STZ activities are a transient process. At a finite mechanical load and temperature, they are constantly generated and annihilated from place to place.

The STZs deformation mechanism is illustrated in Fig. 1.9 (E.R. Homer and C.A. Schuh 2009). Usually the STZs are the spatially and temporally heterogeneous plastic deformation field in the metallic glasses when the temperature is less than their glass transition temperature. Chen M. W.'s group proposed a quantitative experimental methodology (D. Pan, A. Inoue et al. 2008) to characterize of STZ size. Their results showed that the measured STZ volumes were in good conformity with the prediction by theoretical analysis (Johnson WL and Samwer K 2005) and MD simulation (Mayr SG 2006).

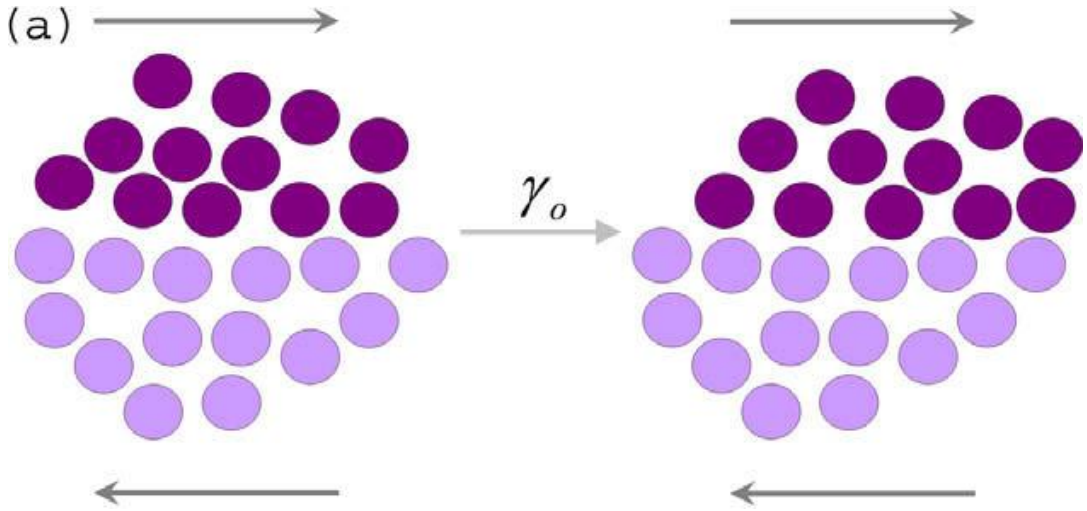

Figure 1.9 Shear transformation zone (STZ), where several dozen atoms shear inelastically under an applied shear stress

1.4 Deformation Behaviors

The study of mechanical behavior of metallic glasses started in the early 1970s. Under the uniaxial tensile force, the metallic glasses deformed elastically and fractured suddenly with very slightly plastic strain (<0.5%). But for compression, the metallic glasses showed some significant

plastic strain (about 1.5% for Cu44Zr48Al7Fe (Xu Hong-wei, Du Yu-lei et al. 2012)). All these plastic strains are generated by the nucleation and propagation of shear bands which are localized.

1.4.1 Elastic and Anelastic Deformation Behaviors

Metallic glasses deform elastically to an applied force before yielding, the same as their competing crystalline. The elastic deformation behavior can be characterized by their elastic modulus. During this deformation, there may be some small and isolated local yielding events which are not sufficient to cause the elastoplastic transition at the macroscopic scale (T. Egami 2008). Interestingly, the Young's modulus and the shear modulus of metallic glasses were found to be approximately 30% less than those of crystalline metal alloys with the same composition, but the bulk modulus to be just reduced by only 6% (C. A. Schuh, T. C. Hufnagel et al. 2007). Chen (H. S. Chen 1978) argued that the cause of this reduction was a lower bond density associated with less efficient space filling. Suzuki et al. (Suzuki Y. and T. Egami 1985) suggested that these differences were attributed to anelasticity, which was originated from the relaxation of atomic configurations and has been experimentally proved by Argon (A. Argon 1982). Argon found that the strain could be completely recovered after the removal of stress and elevation of higher temperature. The systematic investigation on anelasticity of metallic glasses is studied in chapter 3 by fast nanoindentation at room temperature.

1.4.2 Yielding Criterion

The asymmetric yield behaviors of metallic glasses were captured in several experiments (T. Mukai, T. G. Nieh et al. 2002; Z.F. Zhang and J. E. L. Schultz 2003), which are reflected by the

tension-compression strength asymmetry. Furthermore, the shear-off angles of a test sample under tension and compression are about 56° and 42 ° respectively. Donovan (P. E. Donovan 1989) suggested that the yielding of metallic glasses obeys the Mohr-Coulomb criterion based on study of a $Pd_{40}Ni_{40}P_{20}$ alloy.

The stress (σ_n) normal to the shear displacement and applied shear stress (τ) play a vital role in the Mohr-Coulomb criterion. The expression of the Mohr-Coulomb criterion is listed below:

$$\tau_y = \tau_0 + \alpha\sigma_n \tag{1.3}$$

where, τ_y is the effective shear yield stress, τ_0 a constant and α(sensitive to pressure) a system-specific coefficient that controls the strength of the normal stress effect. Schuh and Lund (C. A. Schuh and A. C. Lund 2003) confirmed the asymmetric strength of metallic glasses in tension and compression and verified the efficiency of the Mohr-Coulomb criterion for the yielding behavior on the metallic glasses based on the atomistic calculation. For the value of $\alpha = 0.123 \pm 0.004$ found in their articles, the prediction of a compressive shear angle is $\theta = 41.5 \pm 0.15°$ and agrees with previous experiment results with a range of $\theta = 39.5 - 43.7°$ for a variety of metallic glasses.

Apart from the tension-compression asymmetry, a size effect is also evident in the measurement of yielding strength. The previous work showed that the yield strength of metallic glasses was slightly increased by decreasing the specimen size. This phenomenon was first

interpreted by Weibull statistics (M. Calvo 1989; Lee C. J., J. C. Huang et al. 2007) based on the assumption of that the yield strength is determined by the weakest point in a brittle material. So the fracture probability P_f can be described as:

$$P_f = 1 - exp\left[-V\left(\frac{\sigma-\sigma_u}{\sigma_0}\right)^m\right] \quad (1.4)$$

Here, σ_0 is a scaling parameter, m is the Weibull modulus, σ is the applied uniaxial stress, V is the specimen volume and σ_u denotes the stress at which there is a zero failure probability, and is usually taken to be zero. For a fixed fracture probability by assuming the characteristic defects determining fracture, the above equation can be reduced to:

$$d^3\sigma^m = const \quad (1.5)$$

Where d is the diameter of the compression sample. The above equation shows that the compression stress increases with decreasing sample size, which somewhat agrees with the experimental results.

Usually, the Weibull modulus of ductile crystalline metals is larger than 100 and brittle ceramics is less than 10. But the estimated Weibull modulus m is scattered from 20 to 80 (M. Calvo 1989; Lee C. J., J. C. Huang et al. 2007). There are two issues which should be considered when using this equation to describe the relation of fracture probability and applied stress. The first one is defects. In fact, there are many possible defects in metallic glasses, such as casting-induced voids, inclusions, surface irregularities and contaminations, chemical/structural

heterogeneity. The size and distribution of these defects are difficult to be exactly measured. Apart from that, the influential factors induced during the experiment are also very complex and inevitable. Considering the above reasons, the Weibull function should be modified to including the influence of above factors.

1.4.3 Plastic Deformation Behaviors: Shear Bands

The deformation of metallic glasses is localized in the shear bands at the ambient temperature. Specifically, the duration of shear band propagating is typically about 10^{-5} s (T. C. Hufnagel, T. Jiao et al. 2002) and shear band nucleation is a rate controlling process. The observation of stress serration during the compression has been reported for several times (H. Kimura and T. Masumoto 1983; W. J. Wright, R. Saha et al. 2001) and was attributed to the emission of shear bands. Because of the above reason, the discrete "pop-in" events are observed in the load-displacement curve of nanoindentation. Meanwhile, Schuh et al. (C. A. Schuh, T. G. Nieh et al. 2002; C. A. Schuh, A. S. Argon et al. 2003; C. A. Schuh and T. G. Nieh 2003) also reported the stepped load-displacement curve punctuated by discrete bursts of plasticity during the characterization of mechanical properties of different metallic glass alloy system. They suggested that these discrete "pop-in" events correspond to the activation of individual shear bands and the character of serrations were strongly loading rate dependent. That means that for slower loading rate serrations are more obvious and for rapid the load-displacement curve becomes smooth. The similar phenomenon was captured during the stress serration in the micro-pillar compression test(Yang Y, Ye JC et al. 2011).

Schuh et al. (C. A. Schuh, T. G. Nieh et al. 2002) systematically explored the loading rate dependence of serrated flow during nanoindentation. He found that at sufficiently low indentation rates plastic deformation occurred entirely in discrete events of isolated shear banding and at the highest rates deformation was continuous (no evidence of discrete events at any size scale). In other words, at high rates, multiple shear bands operated simultaneously, because a single shear band cannot accommodate the imposed stain rapidly enough. After that, Schuh et al. proposed the presence of a second homogeneous deformation regime by investigation of nanoindentation at high temperatures. At high deformation rates, the second homogeneous regime occurs even well below the glass transition. When deformation rates exceed the characteristic rate for shear band nucleation, it raises kinetically forcing strain distribution. They quantitatively rationalized the second regime and extracted the natural frequency of shear band nucleation of 6×10^4 s^{-1}. At last, the critical radius of a shear band (transition from nucleation to propagation) was estimated to be in submicron range.

During the localized shear band nucleation and propagation, the estimated temperature of shear band rise is ranging from less than 0.1 to a few thousand Kelvin (T. Masumoto and R. Maddin 1975; A.S. Argon 1979; P. E. Donovan 1989; W. J. Wright, R. Saha et al. 2001; Z.F. Zhang and J. E. L. Schultz 2003) in the references and remains as a controversial topic. The main cause of this so extremely discrepancy is difficult to directly measure the temperature in such small distance (the width of shear band is about 10nm (P. Lowhaphandu, S. L. Montgomery et al. 1999; T. Mukai, T. G. Nieh et al. 2002)) and short time scales (shear band propagation is in 10^{-5}s (C. A. Schuh and A. C. Lund 2003)). To visualize the temperature rise of shear band during its propagation, Lewandowski and Greer (P. Wesseling, T. G. Nieh et al. 2004) bent a Zr-based

BMG coated with indium and observed the melting process of the coating near shear bands. Based on their heat conduction analysis, they found that shear band operation was not fully adiabatic. Accompanied by the shear band operation, the viscosity drops rapidly and significant softening occurs once the temperature reaches the glass transition temperature.

Yang et al. (B. Yang, C. T. Liu et al. 2006) used the STZ model to calculate the temperature increase inside the shear band. By balancing the mechanical work and heat generation within a STZ unit, the equation for temperature rise within a shear band can be expressed as:

$$\Delta T_s = \frac{\alpha \sigma_f}{2\rho C_p} \tag{1.6}$$

Here, ρ is the density, C_p is the heat capacity, σ_f is the nominal fracture strength and $\alpha \approx 0.9$ is the ratio of plastic work converted to heat. Apart from that, Yang et al. (B. Yang, C. T. Liu et al. 2006) also measured the heat generated by shear band emission with a high-speed infrared thermo-graphic camera. Based on these heat measurements, they calculated the temperature rise within a shear band which was in great agreement with the theoretical predictions.

In addition, the structure of shear bands is also investigated systematically. Chen et al. (H. Chen, Y. He et al. 1994) firstly reported the crystallization within the shear bands of a bent $Al_{90}Fe_5Gd_5$ metallic glass by the transmission electron microscopy (TEM) investigations. These crystals, located in thin plastic strain region, were face-centered cubic Al and 7-10 nm in diameter. Meanwhile, Jiang et al. (W. H. Jiang, F. E. Pinkerton et al. 2003; W. H. Jiang and M.

Atzmon 2006) also investigated the formation of nanocrystals in the same alloy. They carefully examined the microstructure of the bending sample at a temperature of -40℃ by TEM. There was a high density of nanocrystals within the shear bands caused by the deformation-assisted atomic transport.

The same phenomenon was observed on a Zr-based BMG during nanoindentation at ambient temperature. Kim et al. (J. J. Kim 2002) reported the nanocrystalline nucleation in and around shear bands near indentation marks just the same as thermal annealing induced nanocrystallines. Chen et al. (M. Chen, A. Inoue et al. 2006) also reported plastic flow induced nanocrystallization in Zr-Cu metallic glasses. But Li et al. (J. Li 2002; J. Li, X. Gu et al. 2003) found a larger number of nano voids, as a result of coalescence of excess free-volume, of approximately 1nm diameter in the shear bands.

1.5 Thermal Annealing

The structure of metallic glasses is thermodynamically metastable compared with the ideal glassy state. By structural rearrangement, the metallic glasses can reach the ideal glassy state or transform to an equilibrium crystalline structure. These continuous transformations induced by external energies, such as heat treatments and external stresses, lead to continuous changes in physical, chemical and mechanical properties.

According to the above descriptions about the structural rearrangement, the nanocrystalline/glass composites of metallic glasses can be produced by annealing treatment(W. Dmowski, C. Fan et al. 2007). Based on these promoting applications, the microstructural

evolution during annealing has been intensively studied (H. S. Chen 1978; L.Q Xing, C Bertrand et al. 1998; W. H. Jiang, F. E. Pinkerton et al. 2003; Y.F. Gao, B. Yang et al. 2007; P.N. Zhang, J.F. Li et al. 2009).

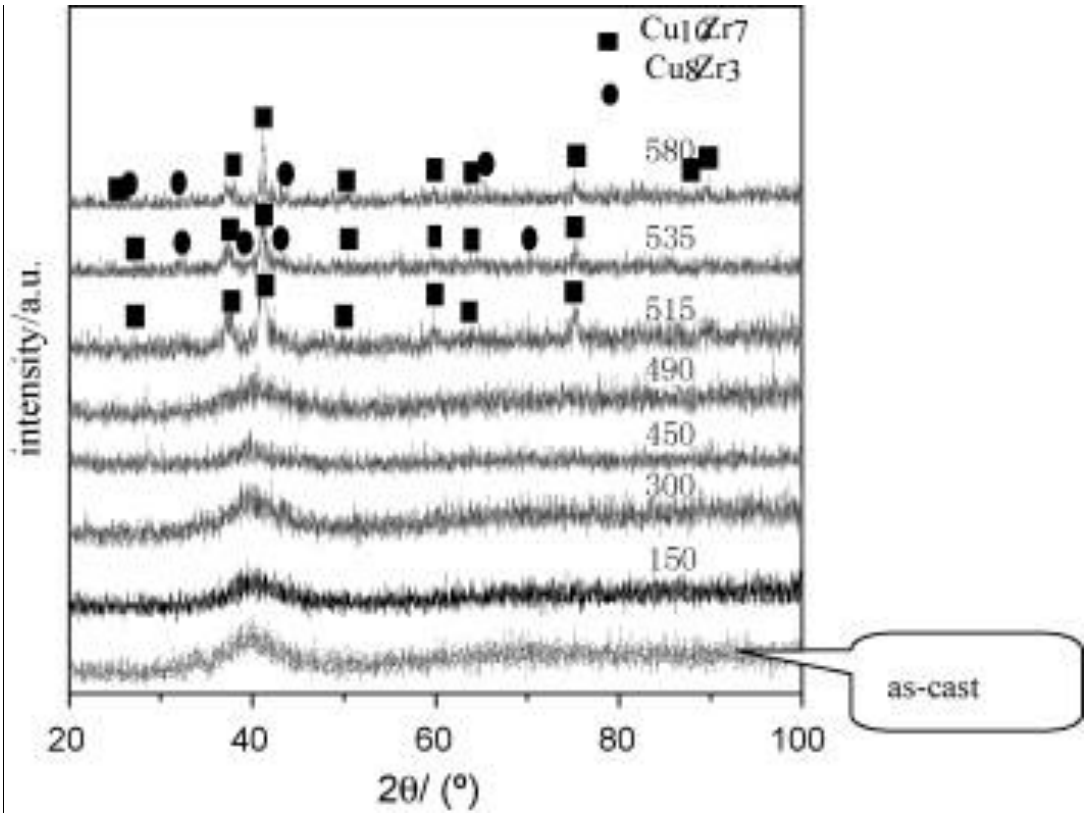

Figure 1.10 XRD patterns of $Cu_{58.1}Zr_{35.9}Al_6$ BMG and its alloys annealed at different temperature.

In 2010, Ping Li et al. (Ping Li, Jingyan Hao et al. 2010) studied the crystallization behavior and the elastic properties of $Cu_{58.1}Zr_{35.9}Al_6$ bulk metallic glass using ultrasonic pulse focusing method. The XRD patterns of its as-cast and annealed alloys are shown in Fig. 1.10. From this figure, there is no structural change when the annealing temperature is below glass transition temperature (T_g =487℃) and no obvious crystalline peaks in the XRD pattern even when it is annealed at 490℃ just above T_g. when the annealed temperature is reached 515℃

(between T_g and T_x), the $Cu_{10}Zr_7$ phase appeared. A small amount of Cu_8Zr_3 peaks is observed at 535℃ slightly above T_x. The same phenomenon is reported in the previous studies (J. Z. Jiang, Y. X. Zhuang et al. 2001; F.X. Qin, X.M. Wang et al. 2007; Mihai Stoica, Nele Van Steenberge et al. 2010).

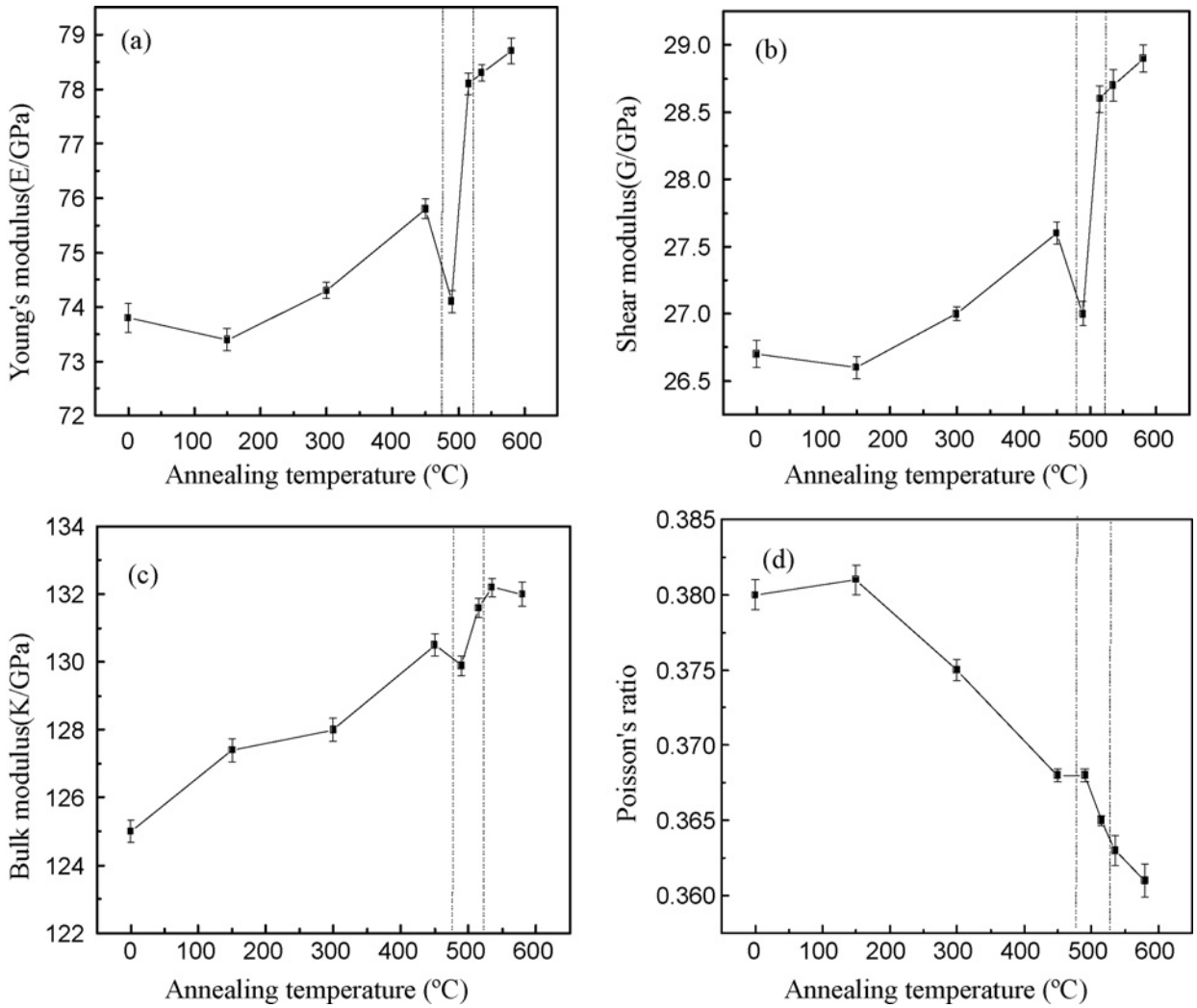

Figure 1.11 Variations of elastic parameters during annealing of Cu58.1Zr35.9Al6 alloy.

The Fig.1.11 (Ping Li, Jingyan Hao et al. 2010) shows their results for the annealing effect on elastic properties: the elastic constants have a progressive trend but Poisson's ratio

decreases; Young's modulus and shear modulus increases by 5–6% and bulk modulus increases by 8%. Similar results are reported in previous studies (M.W.CHEN, A. INOUE et al. 2000; Vaillant M., V. Keryvin et al. 2002; F.X. Qin, X.M. Wang et al. 2007).

Except the mechanical properties are influenced by the annealing temperature, the pressure during annealing is also an important factor for the structure evolution. J. Z. Jiang et al. (J. Z. Jiang, Y. X. Zhuang et al. 2001) investigated the effect of pressure on the formation of quasicrystals and amorphous-to-quasicrystalline phase transformation kinetics in the supercooled liquid region for a $Zr_{65}Al_{7.5}Ni_{10}Cu_{7.5}Ag_{10}$ metallic glass by in situ high-pressure and high-temperature *nonisothermal* and *isothermal* X-ray powder diffraction measurements using Synchrotron radiation. They found that the pressure increased the onset temperature for the formation of quasicrystals with a slope of 9.4K/GPa and reduced the average grain size of quasicrystals.

The above is focused on the structure evolution and mechanical properties change induced by thermal annealing. These results are important for a number of aspects, such as the understanding of the nucleation and growth in the metallic supercooled liquid, the evaluation of the glass-forming ability of the melts and thermal stability of metallic glasses, the production of bulk nanocrystalline and composites (M. Yousuf and K.G. Rajan 1984; J. Schroers, R. Busch et al. 1999; J. Schroers, W.L. Johnson et al. 2000; T.A. Waniuk, J. Schroers et al. 2001; J. J. Kim, Y. Choi et al. 2002; Z. Zhang, L. Xia et al. 2002). Based on these potential functions, annealing is an extensive method to investigate the structure evolution and produce composites. To well investigate structure evolution of a Zr-based thin film, high-resolution atomic force microscopy

(AFM) is used to characterize the as-deposited and annealed ones. The details for the structure characterization of the alloys annealed slightly below the glass transition temperature are in chapter 5.

1.6 Applications

The mechanical properties of materials play a very important role for their applications. Because of high strength exhibited as a result of lack of dislocations, metallic glasses possess wider application areas compared with their crystalline counterparts.

The high toughness makes the BMGs be used in a number of areas, ranging from medical instruments to electronic devices. Sport equipments are their useful applications, such as ski equipment, baseball bats, and golf clubs and so on.

Medical implants are their potential applicant areas. Because of the lightweight, tough, high corrosion resistance and cheaper than high-quality steels, the BMGs are the acceptable implant materials.

Besides of the above areas, the BMGs are also useful in the microscale electronic components. Table 1.1 (W.H. Wang, C. Dong et al. 2004) is the summary of the present and potential applications with their corresponding mechanical properties.

Table 1.1 Possible application fields for BMGs

Properties	Application field
High strength	Machinery structural materials
High hardness	Cutting materials
High fracture toughness	Die materials
High impact fracture energy	Tool materials
High fatigue strength	Bonding materials
High elastic energy	Sporting goods materials
High corrosion resistance	Corrosion resistance materials
High wear resistance	Writing appliance materials
High reflection ratio	Optical precision materials
High hydrogen storage	Hydrogen storage materials
Good soft magnetism	Soft magnetic materials
High frequency permeability	High magnetostrictive materials
Efficient electrode	Electrode materials
High viscous flowability	Composite materials
High acoustic attenuation	Acoustic absorption materials
Self-sharping property	Penetrator
High wear resistance and manufacturability	Medical devices materials

1.7 Motivation and Objectives

Although, the BMGs exhibit a high quality performance, such as high yield strength, corrosion resistance, large elastic limitation, and have attracted extensive scientific and technological

interest, their poor plasticity limits the applicability and needs to be further improved. For this reason, it is necessary to study the relation between the governing structural factors or material properties and their structures.

Till now, the free-volume theory, short-range order and medium-range order are used to characterize the atomic structure of BMGs and be related to their mechanical properties. But in some publications, the free volume was described by the distribution of SRO atomic clusters. Indeed, the free volume, SRO and MRO are difficult to detect or measure experimentally. So, the molecular dynamics (MD) and Monte Carlo (MC) simulations are selected to clarify the correlation between above structural factors and the mechanical properties and to search methods of improving the mechanical properties and dimensions.

After nearly a half century of investigation, it is still lack of a systematic and thorough understanding of the micro-/nano-mechanical deformation mechanism of BMGs. So, in my research, nanoindentaion is used to test the BMGs mechanical behaviors with different tips, such as, Berkovich (standard one), spherical, flat-ended (for micro-pillars) and etc; the surface imaging techniques (SEM, TEM, AFM) are also employed for the structural and mechanical characterization; the analytical models are also derived to explain the correlation between the structural factors and the mechanical properties.

Based on the above reasons, my research will focus on the investigation of metallic glass structure. In chapter 3, the structure heterogeneity and anleastic deformation are revealed through spherical nanoindentation. The experimental and theoretical results are a successful exploration

of the relation between the nano-scale mechanical property and structure in metallic glasses. In chapter 4, the plastic bending tests are used to investigate the structure evolution under the condition of continuous plastic deformation. In chapter 5, the technique of high-resolution atomic-force-microscopy is employed to capture the nano-scale structural heterogeneity and reveal their evolution after thermal annealing. In chapter 6, the major factors which can influence the structural contrast in the DAFM images are systematically investigated by a comparative study of different TFMGs and single-crystal silicon.

1.8 References

A. Argon (1982). "Mechanisms of inelastic deformation in metallic glasses." Phys. Chem. Solids **43**: 7.

A. Inoue, N. Nishiyama and T. Matsuda (1996). "Preparation of bulk glassy Pd40Ni10Cu30P20 alloy of 40 mm in diameter by water quenching." Mater. Trans. JIM **37**: 4.

A. Inoue, T. Zhang and A. Takeuchi (1997). "Bulk amorphous alloys with high mechanical strength and good soft magnetic properties in Fe-TM-B (TM=IV-VIII group transition metal) system." Appl. Phys. Lett. **71**(4): 3.

A. Peker and W. L. J. (1993). "A highly processable metallic glass $Zr_{41.2}Ti_{13.8}Cu_{12.5}Ni_{10.0}Be_{22.5}$." Appl. Phys. Lett. **63**(17): 3.

A.S. Argon (1979). "Plastic deformation in metallic glasses." Acta Metall. **27**(1): 12.

A.S. Argon and H. Y. Kuo. (1979). "Plastic flow in a disordered bubble raft (an analog of a metallic glass)." Materials Science and Engineering **39**(1): 9.

Akihiko Hirata, Pengfei. Guan., Takeshi Fujita, Yoshihiko Hirotsu, Akihisa Inoue, Alain Reza Yavari, Toshio Sakurai and Mingwei Chen, (2010). "Direct observation of local atomic order in a metallic glass." Nature Materials Letters **10**: 6.

B. L. Shen, H. Koshiba, T. Mizushima and A. Inoue (2000). "Bulk amorphous Fe-Ga-P-B-C alloys with a large supercooled liquid region." Mater. Trans. JIM **41**(7): 4.

B. Yang, C. T. Liu., T.G. Nieh, M. Morrison, P. K. Liaw and R.A. Buchanan (2006). "Localized heating and fracture criterion for bulk metallic glasses." J. Mater. Res. **21**(4): 8.

Bernal, J. D. (1959). "A geometrical approach to the structure of liquids." Nature **183**: 7.

C. A. Angell (1995). "Formation of glasses from liquids and biopolymers." Science **267**(5206): 12.

C. A. Schuh and A. C. Lund. (2003). "Atomistic basis for the plastic yield criterion of metallic glass." Nature Mater. **2**(7): 4.

C. A. Schuh, A. S. Argon., T.G. Nieh and J. Wadsworth (2003). "The transition from localized to homogeneous plasticity during nanoindentation of an amorphous metal." Philos. Mag. A **83**(22): 13.

C. A. Schuh, T. C. Hufnagel and U. Ramamurty (2007). "Mechanical Behavior of Amorphous Alloys." Acta Mater. **55**: 43.

C. A. Schuh and T. G. Nieh. (2003). "A nanoindentation study of serrated flow in the bulk metallic glasses." Acta Mater. **51**(1): 13.

C. A. Schuh, T. G. Nieh and Y. Kawamura (2002). "Rate dependence of serrated flow during nanoindentation of a bulk metallic glass." J. Mater. Res. **17**(7): 4.

C. Fan, P. K. Liaw., C. T. Liu, (2009). "Atomistic model of amorphous materials." Intermetallics **17**: 2.

C. Fan, P. K. Liaw., V. Haas, J. J. Wall, H. Choo, A. Inoue, C. T. Liu (2006). "Bulk Amorphous Alloys at Ambient and Cryogenic Temperatures." Phys. Rev. B **74**(1): 6.

Cang Fan, P. K. L., T. W. Wilson, W. Dmowski, Th. Proffen, H. Choo, C.T. Liu, (2006). "Structural Model for Bulk Amorphous Alloys." Appl. Phys. Lett. **89**(11): 3.

Chen H.S. (1974). "Thermodynamic considerations on the formation and stability of metallic glasses." Acta Metall. **22**: 7.

Cohen M. H. and Turnbull D. (1964). "Metastability of amorphous structures." Nature **203**: 1.

Connel G.A.N. (1975). "Dense random packings of hard and compressible spheres." Solid State Commun **16**(1): 4.

D. Ma, A. D. Stoica, X.L. Wang, (2009). "Power-law scaling and fractal nature of medium-range order in metallic glasses." Nature Mater. **8**(1): 5.

D. Pan, A. Inoue, T. Sakurai, M. W. Chen (2008). "Experimental characterization of shear transformation zones for plastic flow of bulk metallic glasses." PNAS **105**(39): 4.

D.B. Miracle (2004). "A structural model for metallic glasses." Nature Materials **3**: 6.

D.E. Polk (1971). "Structural model for amorphous silicon and germanium." Journal of Non-Crystalline Solids **5**(5): 12.

Dubois J. M., Gaskell P. H. and Le Caer. G. (1985). "A Model for the Structure of Metallic Glasses Based on Chemical Twinning." Proc. R. Soc, Lond. A **402**: 35.

Dubois J. M., Gaskell P. H. and Le Caer. G. In Proc (1985). "In Proc, 5th Intl. Conf. On Rapidly Quenched Metals (eds S. Steeb and H. Warlimont)." Elsevier.

E.R. Homer and C.A. Schuh (2009). "Mesoscale Modeling of Amorphous Metals by Shear Transformation Zone Dynamics." Acta Materialia **57**: 11.

F. Spaepen (1977). "A microscopic mechanism for steady state inhomogeneous flow in metallic glasses." Acta Metall. **25**(4): 9.

F.X. Qin, X. M. Wang and A. Inoue (2007). "Effect of annealing on microstructure and mechanical property of a TieZreCuePd bulk metallic glass." Intermetallics **15**: 6.

G. D. Scott (1960). "Packing of Spheres." Nature **188**: 2.

G.S. Cargill (1970). "Structural Investigation of Noncrystalline Nickel - Phosphorus Alloys " J. Appl. Phys. **41**: 18.

H. Chen, Y. He, G. J. Shiflet and S. J. Poon (1994). "Deformation-induced nanocrystal formation in shear bands of amorphous alloys." Nature **367**: 3.

H. Habazaki, H. Ukai, K. Izumiya and K. Hashimoto (2001). "Corrosion behaviour of amorphous Ni-Cr-Nb-P-B bulk alloys in 6M HCl solution." Mater. Sci. Eng. A **318**(1-2): 10.

H. Kimura, T. Masumoto (1983). "A model of the mechanics of serrated flow in an amorphous alloy." Phys. Rev. Lett. **96**: 1.

H. S. Chen (1978). "The influence of structural relaxation on the density and Young's modulus of metallic glasses " J. Appl. Phys. **49**: 3.

H. W. Sheng, W. K. Luo, F. M. Alamgir, J. M. Bai and E. Ma (2006). "Atomic Packing and Short-to-medium Range Order in Metallic Glasses." Nature **439**: 7.

J. C. Ye, C. T. Liu, Q. Wang and Y. Yang (2010). "Atomistic Free-Volume Zones and Inelastic Deformation of Metallic Glasses." Nature Materials **9**(8): 5.

J. D. Bernal (1960). "Geometry of the Structure of Monatomic Liquids." Nature **185**: 3.

J.J. Kim, Y. Choi, S. Suresh and A.S. Argon (2002). "Nanocrystallization during nanoindentation of a bulk amorphous metal alloy at room temperature." Science **295**: 4.

J. J. Kim, Y. C., S. Suresh, A.S. Argon (2002). "Nanocrystallzation during nanoindentation of a bulk amorphous metal alloy at room temperature " Science **295**(5555): 4.

J. Li, F. S., T. C. Hufnagel (2002). "Nanometer-scale defects in shear bands in a metallic glass." Philos. Mag. A **82**(13): 8.

J. Li, X. Gu, T. C. Hufnagel (2003). "Using fluctuation microscopy to characterize structural order in metallic glasses." Microsc. Microanal **6**: 7.

J. M. Ziman (1961). "A theory of the electrical properties of liquid metals - The monovalent metals." Philos. Mag. A **6**: 22.

J. Schroers, R. Busch, A. Masuhr and W.L. Johnson (1999). "Continuous Refinement of the Microstructure During Crystallization of Supercooled $Zr_{41}Ti_{14}Cu_{12}Ni_{10}Be_{23}$ Melts." Appl. Phys. Lett. **74**(19): 3.

J. Schroers, W. L. Johnson and R. Busch, (2000). "Crystallization kinetics of the bulk-glass-forming $Pd_{43}Ni_{10}Cu_{27}P_{20}$ melt." Appl. Phys. Lett. **77**(8): 3.

J. Z. Jiang, Y. X. Zhuang, H. Rasmussen, J. Saida and A. Inoue (2001). "Formation of quasicrystals and amorphous-to-quasicrystalline phase transformation kinetics in $Zr_{65}Al_{7.5}Ni_{10}Cu_{7.5}Ag_{10}$ metallic glass under pressure." Physical Review B **64**: 10.

Johnson WL and Samwer K. (2005). "A universal criterion for plastic yielding of metallic glasses with a $(T/T_g)^{2/3}$ temperature dependence." Phys Rev Lett **95**: 4.

Klement W., Willens R. H. and Duwez POL, (1960). "Non-crystalline Structure in Solidified Gold-Silicon Alloys." Nature(187): 2.

L.Q Xing, C. Bertrand, J.-P Dallas and M Cornet (1998). "Nanocrystal evolution in bulk amorphous Zr57Cu20Al10Ni8Ti5 alloy and its mechanical properties." Materials Science and Engineering: A **241**(1-2): 10.

Lee C. J., J. C. Huang and T. G. Nieh (2007). "Sample size effect and microcompression of $Mg_{65}Cu_{25}Gd_{10}$ metallic glass." Applied Physics Letters **91**(16): 3.

M. Calvo (1989). "Application of the Weibull statistics to the characterization of metallic-glass ribbons " J Mater Sci. **24**: 8.

M. Chen, A. Inoue, W. Zhang and T. Sakurai (2006). "Extraordinary plasticity of ductile bulk metallic glasses." Phys Rev Lett **96**.

M. H. Cohen and D. Turnbull (1959). "Molecular transport in liquids and glasses." J. Chem. Phys. **31**: 6.

M. H. Cohen and D. Turnbull (1961). "Composition Requirements for Glass Formation in Metallic and Ionic Systems." Nature **189**: 2.

M. Yousuf and K. G. Rajan (1984). "Pressure induced structural relaxation in amorphous solids — example of $Fe_{40}Ni_{40}P_{14}B_6$ " J. Mater. Sci. Lett. **3**(2): 4.

M.W.Chen, A. Inoue, T. Zhang, A. Sakai, T. Sakurai (2000). "Formation of icosahedral quasicrystals in an annealed $Zr_{65}Al_{7.5}Ni_{10}Cu_{12.5}Ag_5$ metallic glass." Philosophical Magazine Letters **80**(4): 7.

Mayr SG (2006). "Activation energy of shear transformation zones: A key for understanding rheology of glasses and liquids." Phys Rev Lett **97**(19): 4.

Mihai Stoica, Nele Van Steenberge, Jozef Bednarˇcik, Norbert Mattern, Hermann Franz and Jurgen Eckert, (2010). "Changes in short-range order of $Zr_{55}Cu_{30}Al_{10}Ni_5$ and $Zr_{55}Cu_{20}Al_{10}Ni_{10}Ti_5$ BMGs upon annealing." Journal of Alloys and Compounds **506**: 3.

Oscar Belart Bayo (2008). "Production and Characterization of Mechanical Properties of Metallic Glasses."

P. E. Donovan (1989). "A yield criterion for $Pd_{40}Ni_{40}P_{20}$ metallic glass." Acta Mater. **37**(2): 12.

P. H. Gaskell (1978). "A new structural model for transition metal–metalloid glasses." Nature **276**: 2.

P. Lowhaphandu, S. L. Montgomery and J. J. Lewandowski (1999). "Effects of superimposed hydrostatic pressure on flow and fracture of a Zr-Ti-Ni-Cu-Be bulk amorphous alloy." Scripta Materialia **41**(1): 6.

P. Wesseling, T. G. Nieh, W. H. Wang and J. J. Lewandowski (2004). "Preliminary assessment of flow, notch toughness, and high temperature behavior of $Cu_{60}Zr_{30}Hf_{10}Ti_{10}$ bulk metallic glass." Scripta Materialia **51**(2): 4.

P.N. Zhang, J. F. Li, Y. Hu and Y.H. Zhou (2009). "Microstructural evolution during annealing and rolling Zr52.5Cu17.9Ni14.6Al10Ti5 bulk metallic glass." Materials Science and Engineering A **499**: 5.

Ping Li, Jingyan Hao, Jialong Tan and Qing Wang (2010). "Influence of annealing on the elastic properties and microstructure of Cu58.1Zr35.9Al6 bulk metallic glass." Materials Science and Engineering A **527**: 4.

Sadoc J. F., Dixmier J. and Guinier A. (1973). "Theoretical calculation of dense random packings of equal and non-equal sized hard spheres applications to amorphous metallic alloys." Journal of Non-Crystalline Solids **12**: 15.

Spaepen, F. (1977). "A microscopic mechanism for steady state inhomogeneous flow in metallic glasses." Acta Metallurgica **25**: 9.

Suzuki Y. and T. Egami (1985). "Shear Deformation of Glassy Metals - Breakdown of Cauchy Relationship and Anelasticity." Journal of Non-Crystalline Solids **75**(1-3): 6.

T. C. Hufnagel, T. Jiao, Y. Li, L. Q. Xing and K. T. Ramesh (2002). "Deformation and failure of $Zr_{57}Ti_5Cu_{20}Ni_8Al_{10}$ bulk metallic glass under quasi-static and dynamic compression." J. Mater. Res. **17**(6): 5.

T. Egami (1997). "Universal criterion for metallic glass formation." Mater. Sci. Eng. A **226-228**: 7.

T. Egami (2008). "Atomistic theory of metallic liquids and glasses." Springer-Verlag: 30.

T. Masumoto and R. Maddin (1975). "Structural stability and mechanical properties of amorphous metals." Mater. Sci. Eng. **19**(1): 24.

T. Mukai, T. G. Nieh, Y. Kawamura. A Inoue and K. Higashi (2002). "Dynamic response of a $Pd_{40}Ni_{40}P_{20}$ bulk metallic glass in tension." Scripta Materialia **46**(1): 5.

T. Mukai, T. G. Nieh, Y. Kawamura. A Inoue and K. Higashi (2002). "Influence of strain rate on compressive mechanical behavior of $Pd_{40}Ni_{40}P_{20}$ bulk metallic glass." Intermetallics **10**(11-12): 7.

T.A. Waniuk, J. Schroers and W.L. Johnson (2001). "Critical cooling rate and thermal stability of Zr–Ti–Cu–Ni–Be alloys." Appl. Phys. Lett. **78**: 3.

Vaillant M., V. Keryvin, T. Rouxel and Y. Kawamura (2002). "Changes in the mechanical properties of a Zr55Cu30Al10Ni5 bulk metallic glass due to heat treatments below 540 degrees C " Scripta Materialia **47**(1): 5.

W. Dmowski, C. Fan, M.L. Morrison, P.K. Liaw and T. Egami (2007). "Structural changes in bulk metallic glass after annealing below the glass-transition temperature." Materials Science and Engineering: A **471**(1-2): 5.

W. Dmowski, T. Iwashita, C.-P. Chuang, J. Almer and T. Egami, (2010). "Elastic Heterogeneity in Metallic Glasses." Phys. Rev. Lett. **105**.

W. H. Jiang, F. E. Pinkerton and M. Atzmon (2003). "Deformation-induced nanocrystallization in an Al-based amorphous alloy at a subambient temperature " Scripta Materialia **48**(8): 6.

W. H. Jiang and M. Atzmon (2006). "Mechanically- assisted nanocrystallization and defects in amorphous alloys: A high-resolution transmission electron microscopy study." Scripta Materialia **54**: 4.

W. J. Wright, R. Saha and W. D. Nix (2001). "Deformation mechanisms of the $Zr_{40}Ti_{14}Ni_{10}Cu_{12}Be_{24}$ bulk metallic glass." Mater. Trans. JIM **42**(4): 8.

W. L. Johnson (1999). "Bulk glass-forming metallic alloys: Science and technology." MRS Bulletin **24**(10): 15.

W.H. Wang, C. Dong and C.H. Shek (2004). "Bulk metallic glasses." Materials Science and Engineering R **44**: 45.

X. J. Liu, G. L. Chen, X. Hui, T. Liu and Z. P. Lu (2008). "Ordered clusters and free volume in a Zr-Ni metallic glass." Applied Physics Letters **93**: 3.

Xu Hong-wei, Du Yu-lei and Deng Yu (2012). "Effect of minor-addition of Fe on structural and mechanical properties of CuZrAl bulk metallic glass." Trans. Nonferrous Met. Soc. China **22**: 4.

Y.F. Gao, B. Yang and T.G. Nieh, (2007). "Thermomechanical instability analysis of inhomogeneous deformation in amorphous alloys." Acta Mater. **55**: 9.

Yang Y, Ye JC, Lu J and Liu CT (2011). "Dual character of stable shear banding in bulk metallic glasses " Intermetallics **19**(7): 9.

Z. Zhang, L. Xia, R. J. Wang, B. C. Wei, M. X. Pan and W. H. Wang (2002). "Structure evolution and property changes in NdAlFeCo bulk metallic glass during crystallization." Appl. Phys. Lett. **81**(2002): 3.

Z.F. Zhang and J. E., L. Schultz (2003). "Difference in compressive and tensile fracture mechanisms of Zr59Cu20Al10Ni8Ti3 bulk metallic glass." Acta Materialia **51**(4): 13.

2 Methodologies

In this chapter, the equipments and techniques used to characterize the morphology, composition, structure and mechanical properties of metallic glasses are briefly introduced.

2.1 Nanoindentation

All nano-/micromechanical testing were performed using the Hysitron MultiRange NanoProbe®. The indentation was performed by actuating the probe with a pre-stressed piezo material. With the increasing voltage applied to the piezo, the probe is pushed into a sample and the force applied to the probe is measured by a load cell, which is placed in series with the actuator. Meanwhile, a capacitive displacement sensor is placed in parallel with them to measure the actual displacement of the indenter tip.

There are two basic operation modes: load control and displacement control. For load control, the loading function is the programmed curve of indenter force vs. time and the displacement is the result of measurement. For displacement control, the loading function is defined by the programmed indenter displacement as a function of time while force is the output signal of the transducer.

A typical MultiRange NanoProbe® head, the same as our high-load nanoindentation system, attached to a TriboIndenter is shown as following:

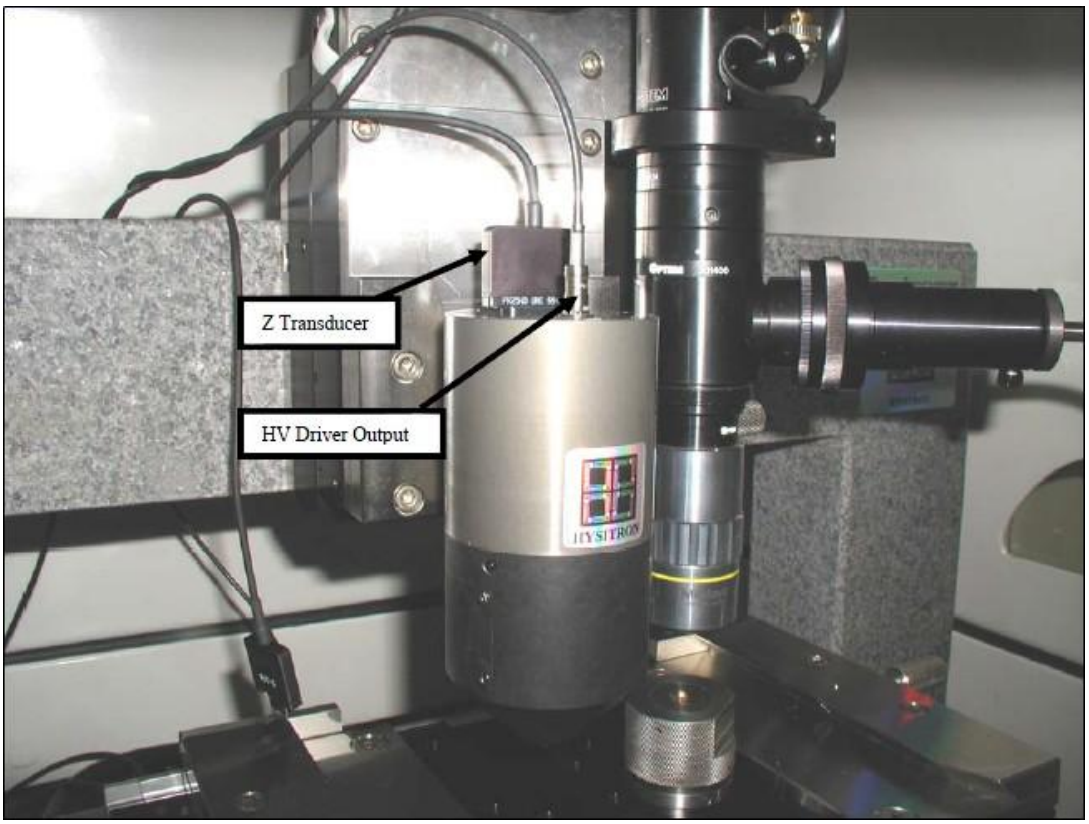

Figure 2.1 MultiRange NanoProbe® head attached to a TriboIndenter

The Hysitron MultiRange NanoProbe® is an extremely versatile tool for nanomechanical testing of a wide variety of samples due to its dynamic and static load capabilities. Depending on the application, different probes can be chosen to maximize the effectiveness of the tool in obtaining repeatable and reliable quantitative data. Usually, there is an extensive list of different geometries and sizes of probes available to accommodate almost any application. Detailed information for some of them is listed in table 2.1.

Table 2.1 The typical applications for some probes

Type of probe	Typical indentation applications	Typical scratch and wear applications
Berkovich Probes	• Bulk Ceramics and Glasses • Bulk Metals and Steels • Thin, Hard Films and Coatings Greater than 100nm Thick • Hard, Smooth Biomaterials (Polished Bone and Tooth Samples) • Hard Polymers (Modulus Greater than 1GPa)	• Scratch resistance of thin coatings (less than 100 nm) • Adhesion of thin coatings (less than 100 nm) • Scratch applications where imaging is important
90 Degree (Cube Corner)	• Ultra-thin coatings less than 100 nm thick • Micro/nano-composites • Fracture of samples • Micro/nano- structured materials	• Ultra-thin coatings less than 20 nm thick • Applications where high-resolution imaging is required
Imaging cono-spherical probes	• Harder polymers (modulus greater than 0.5 GPa) • Hard biomaterials	• Polymers with modulus greater than 0.5 GPa • Hard and soft coatings greater than 50 nm thick • Hard biomaterials • Measuring coefficient of friction
Non-Imaging Cono-Spherical Probes (radii > 10 μm)	• Soft polymers (modulus < 0.5GPa) • Soft biomaterials (tissue, skin, contact lenses, fluid cells) • Structured samples (nano-springs, posts, cantilevers) • MEMS/NEMS	• Soft polymers (modulus less than 0.5 GPa) • Soft biomaterials (tissue, skin, contact lenses, fluid cell) • Coefficient of friction

Note: the above specifications are adapted from the manual of Hysitron™ NanoIndenter system

For the specially designed probes, we have the flat ended and wedge. The flat ended probes are used for the compression test on micro-pillars and the wedge probes for compression and bending test on micro-beams. In addition to that, the wedge probes can be also used to cause delamination by indenting directly at the interface between a substrate and thin film.

To make sure that each measurement is precise and accurate, the equipment should be calibrated carefully before performing indentation testing. Meanwhile, their working parameters, which are listed in table 2.2, should be well understood, which set the limitation of the machine.

Table 2.2 Specifications of Z-axis of the transducer in nanoindentation system

	Low-Load System (TI950)	High-Load System
Maximum force	10 mN	7 N
Load resolution	1 nN	100 nN
Load Noise floor	100 nN	50 μN
Maximum displacement	5 μm	80 μm
Displacement resolution	0.04 nm	0.1 nm
Displacement noise floor	0.2 nm	1 nm
Thermal drift Data	< 0.05 nm/sec	< 1 nm/sec
Acquisition rate	up to 30 kHz	60 Points/sec

Nanoindentation is one of the methods commonly used for studying the nanomechanical behavior of materials (J. J. Kim 2002; C. A. Schuh 2003; J.E. Jakes 2009), and also the platform

for studying the structure-property correlation in BMGs. In my research, Berkovich Probes, the standard probes for Hystron MultiRange NanoProbe®, are selected for the characterization of the basic mechanical properties, i.e. Hardness and Young's Modulus, of BMGs; meanwhile, spherical and flat-end probes are also used to study their small-scale anelastic or microcompression behaviors (Y. Yang, J.C. Ye et al. 2009).

2.2 Atomic Force Microscopy

Atomic force microscopy (AFM) was developed by Gerd Binning and Heinrich Rohrer in the early 1980s at IBM Research – Zurich, which earned them the Nobel Prize for Physics in 1986 (G Binnig, CF Quate et al. 1986). But, the first commercial AFM was available in 1989. A typical commercial AFM is illustrated in figure 2.2 and the sketch of it in figure 2.3 (these two figures are from the manual of the Bruker Multimode™ AFM).

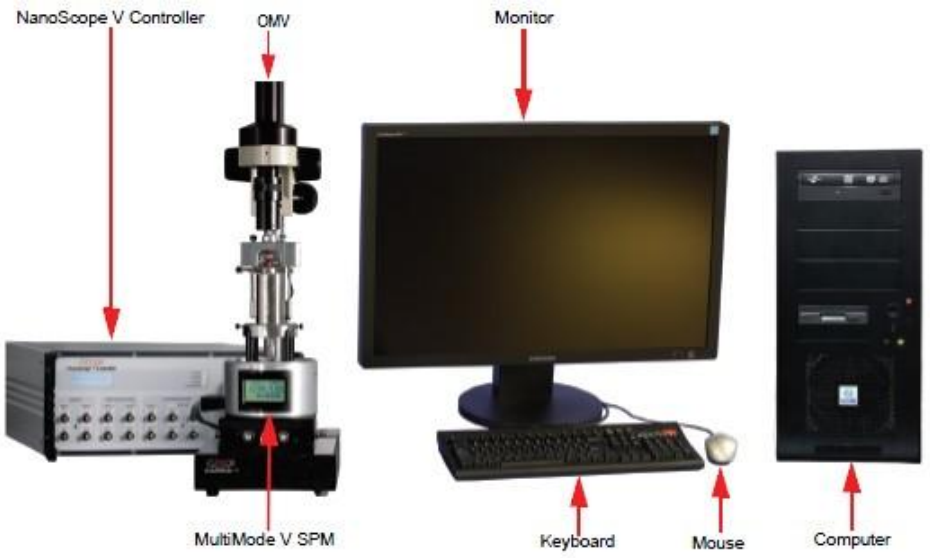

Figure 2.2 A commercial AFM setup

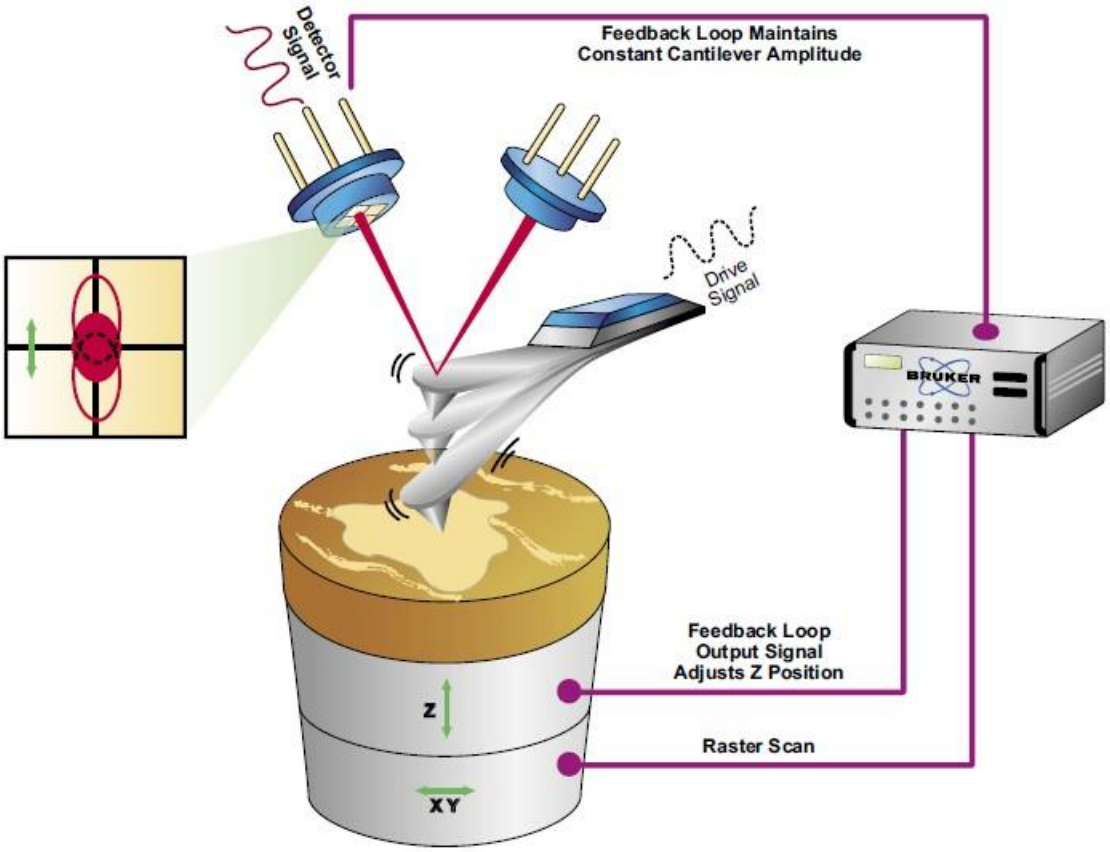

Figure 2.3 Block diagram of atomic force microscope

The AFM is one of the powerful tools for imaging, measuring and manipulating matter at nano-scale(Franz J. Giessibl 2003; Hans-Jurgen Butt, Brunero Cappell et al. 2005). AFM, with demonstrated resolution on the order of fractions of a nanometer, is a very high-resolution scanning probe microscopy (D. Rugar, H. J. Mamin et al. 1988; S. Alexander, L. Hellemans et al. 1989; Gerhard Meyer and Nabil M. Amer 1990; S. Manne, S. A. C. Gould et al. 1990; M. Radmacher 1997). The AFM collects the information by its probe. There are three standard operation modes: contact mode, tapping mode and non-contact mode, which are dependent on the distance between the probe and the sample surface as demonstrated in Fig. 2.4.

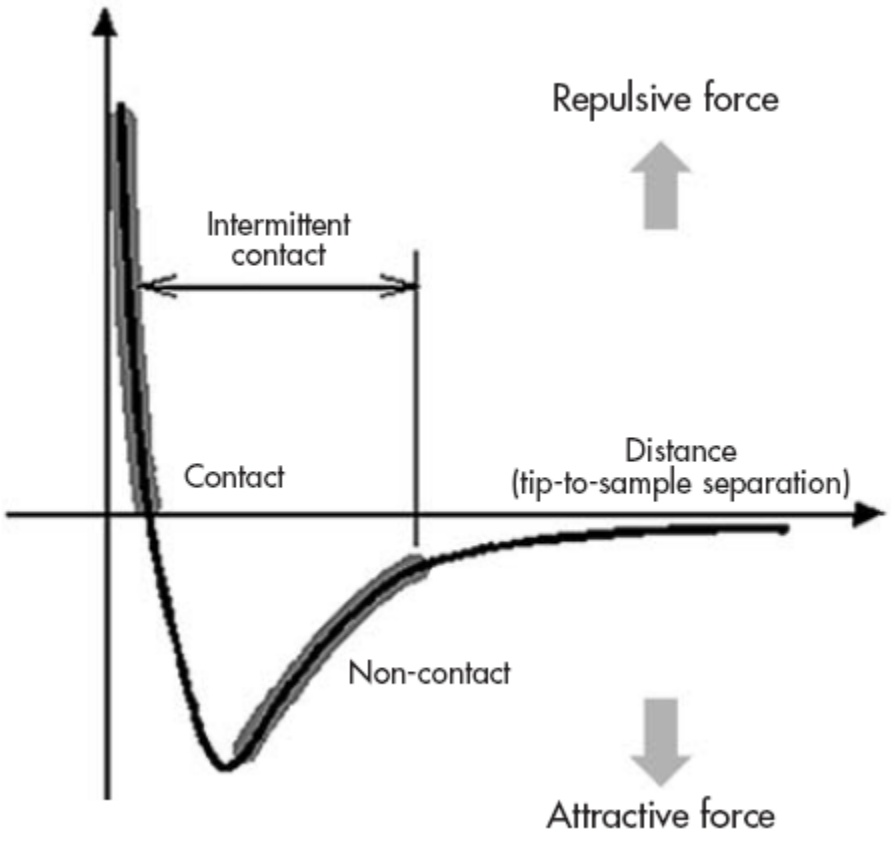

Figure 2.4 The relationship of force and distance between tip and sample surface

In the contact mode, the static tip deflection is used as a feedback signal. To magnify this static signal, a low stiffness cantilever is usually selected. Because the tip is so closed to the sample surface, the force between them is repulsive and is kept constant during scanning by maintaining a constant deflection.

In the non-contact mode, the tip of cantilever does not contact the sample surface and the force between them is attractive. Because of this separation, the quality of AFM images does not suffer from tip or sample degradation, especially for some soft or live biomaterials.

For the tapping mode or intermitted mode, the tip is oscillated at the near resonance frequency and the force between the tip and sample surface is changed all the time. Even if a liquid meniscus layer was developed in ambient conditions, this mode also prevented the tip from sticking to the sample surface which is a major problem for non-contact dynamic mode. In addition, tapping mode is gentle enough even for the visualization of adsorbed single polymer molecules. So, tapping mode is usually selected to capture the morphology of sample surface (Gerhard Meyer and Nabil M. Amer 1990), modulus (Yi Lin, XinCheng Shen et al. 2007), adhesion (D. Sarid, J.P. Hunt et al. 1998), inelastic etc.

In my research, the tapping mode is used to image the structure of thin film metallic glasses. In the tapping mode, the cantilever is excited in/ near the resonance frequency by a piezoelectric actuator. The oscillation amplitude is used as a feedback signal for measuring the topography of a sample and the phase lag (or phase shift) of the cantilever oscillation with respect to the free vibration of the cantilever is simultaneously recorded as a measure of local material properties, such as adhesion and viscoelasticity. The analytical relationship between phase imaging and energy dissipation by the tip-surface forces has been deduced by Cleveland et al (J. P. Cleveland, B. Anczykowski et al. 1998; B. Anczykowski, B. Gotsmann et al. 1999). They assumed that in the steady-state the average energy (E_{ext}) supplied to the cantilever per period must equal to the average energies via hydrodynamic viscous interactions with the environment (E_{med}) and by inelastic interactions at the tip-sample interface (E_{dis}), just as shown in the following equation:

$$E_{ext} = E_{med} + E_{dis} \tag{2.1}$$

Assuming a sinusoidal cantilever response, the relationship between phase shift and energy dissipation can be further cast as below:

$$sin\varphi = \frac{\omega}{\omega_0}\frac{A_{sp}(\omega)}{A_0} + \frac{QE_{dis}}{\pi k A_0 A_{sp}(\omega)} \tag{2.2}$$

Where ω and ω_0 are the excitation and natural frequencies of the cantilever, respectively; φ is the phase shift angle; A_0 and A_{sp} are the free-vibration and set-point amplitudes of the tip; respectively; Q is the damping factor and k is the spring constant.

Comparing experimental and theoretical phase shift dependence on the set-point amplitude on a purple membrane and on a graphite surface, Tamayo and Garc á (Javier Tamayo and Ricardo Garc á 1998) verified the above model. In a wide range of oscillating amplitudes, theoretical data agrees well with experimental data. Ricardo Garc á (R. Garcia, C. J. Go ́mez et al. 2006; Ricardo Garc á, Robert Magerle et al. 2007) derived an analytical relationships between the measured phase shifts and sample properties, which enabled the transformation of experimental phase shift into qualitative measurements of materials properties of silicon and polystyrene/polybutadiene blend (shown in Fig. 2.5). Based on the above relationship, the local structure of the tested thin film metallic glasses can be revealed at the nanoscale resolution, the details of which will be discussed in Chapter 5.

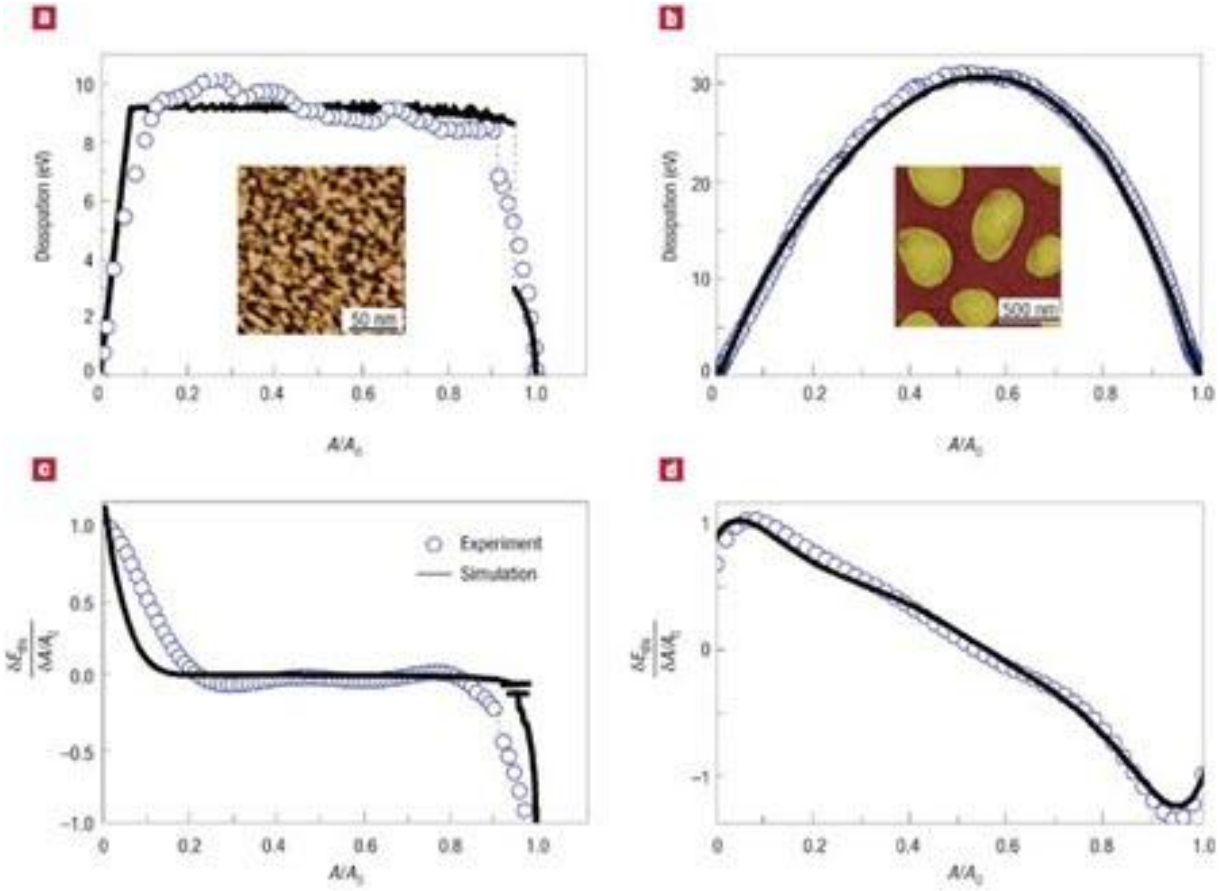

Figure 2.5 Energy dissipation curves of silicon and polystyrene. a, Measured and simulated dynamic-dissipation curves on silicon when there is surface-energy hysteresis and long-range interfacial interactions. b, Measured and simulated dynamic-dissipation curves on a polystyrene region of a polystyrene/polybutadiene blend. c,d, The derivatives of the normalized energy-dissipation curves shown in a and b respectively. The insets show the energy dissipation images taken on Si and on a PS region (R. Garcia, C. J. Go ́mez et al. 2006; Ricardo Garc á, Robert Magerle et al. 2007).

2.3 X-ray Diffraction and Transmission Electron Microscopy

XRD is short for X-ray diffraction, which is a versatile and non-destructive technique. The working principle of XRD is the classical Bragg's law. Usually, XRD is used for the

measurement of the average spacing between layers or rows of atoms, the determination of the orientation of a single crystal or grain, finding the crystal structure of an unknown material and measuring the size, shape and internal stress of small crystalline regions. But in my research, XRD is chosen mainly for the determination of the amorphous structures.

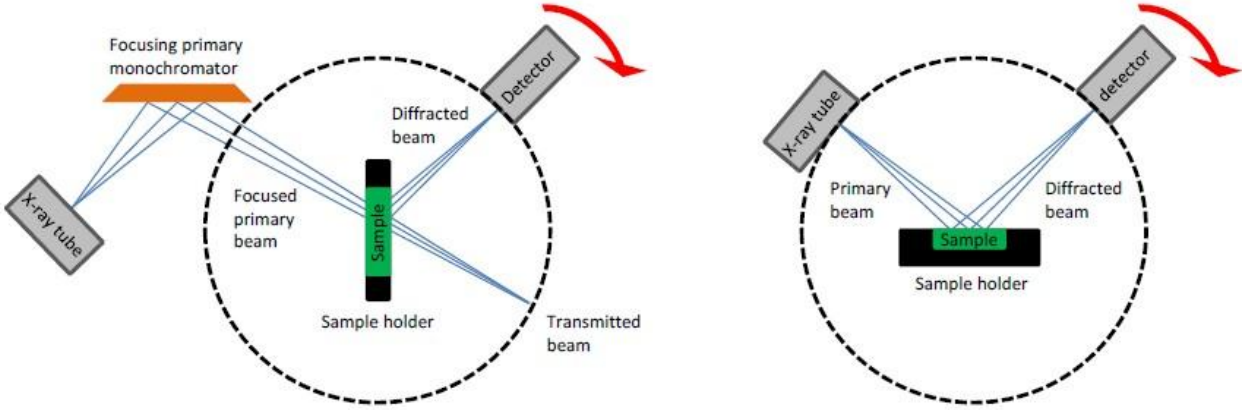

Figure 2.6 Sketches for X-ray Diffraction. The left is the classic transmission geometry (Debye-Scherrer geometry) and right is the classic reflection geometry (Bragg-Brentano geometry)(Sharon Mitchell and Javier P ́rez-Ram ́rez 2010).

Figure 2.6 show the sketches of two classical geometries of an X-ray diffractometer. In fact, the XRD also can be used on non-crystalline material. Usually an electron in an alternating electromagnetic field will oscillate with the same frequency as the field. The electrons around the atom hit by X-ray beam begin to oscillate with the same frequency as the incident X-ray beam. Because the XRD patterns are formed by the diffracted electrons and the atoms in BMGs are arranged in a random way, which is similar to the disorder structure of a liquid, there is a shallow and broaden peak instead of sharp peaks in the $\theta - 2\theta$ scan patterns. As XRD is not sensitive enough to the presence of a small volume fraction of crystalline phases in an amorphous

structure, sometimes the high-resolution transmission electron microscopy (TEM) is also used to confirm the amorphous structure of a BMG sample.

The first TEM was built by Max Knoll and Ernst Ruska in 1931. In 1933, they further developed the first TEM with a resolving power greater than that of light. The first commercial TEM emerged in 1939. The working principles of transmission electron microscope (TEM) are the same as the optical microscope but uses electrons instead of light. Because of this fabulous reduction in the wavelength, the resolution of a TEM is more than a thousand times better than that of an optical microscope. Now, the commercial TEM can image objects on the order of a few angstroms (0.1nm). This possibility for high magnifications makes TEM such important equipment to the research in the medical, biological and materials fields. The TEM images are formed from the interaction of the electrons transmitted through an ultra thin specimen. These extremely high resolution images give an atomic resolution. These images can be used for the analysis of material morphology, material defects, chemical composition and crystallographic structure. In my research, high resolution TEM images were also obtained for the analysis of structural change in BMGs.

2.4 Focused Ion Beam

The first focused ion beam (FIB) systems based on field emission technology were developed by Levi-Setti (Levi-Setti R. 1974; Orloff J. and Swanson L. 1975; W. H. Escovitz, T. R. Fox et al. 1975) in 1975. In the same year Orloff and Swanson (Orloff J. and Swanson L. 1975) developed the FIB systems based on the gas field ionization sources. In my research, the FIB system, which was produced commercially about twenty years ago, was used for the preparation of micro-scale

samples. A finely focused beam of ions (usually gallium) in the FIB system is operated at low beam currents for imaging or high beam currents for site specific milling. The working principles are illustrated in Fig. 2.7. The source of ion beam is liquid Ga. Uchic et al. (Michael D. Uchic, Dennis M. Dimiduk et al. 2004) firstly developed the fabrication process for single crystal micropillar specimens. Lee et al. (Lee 2007) adopted this technique into metallic glasses. From then on, lots of papers (Cheng, X. Wang et al. 2007; A. Dubach, R. Raghavan et al. 2009; C.Q. Chen, Y.T. Pei et al. 2009; Changqiang Chen, Yutao Pei et al. 2010; Kuzmin O. V., Pei Y. T. et al. 2011; O.V. Kuzmin, Y.T. Pei et al. 2012) are focused on the fabrication and mechanical properties measurements of metallic-glass micropillars. J.C. Ye et al. (Ye JC, Lu J et al. 2010) proposed a method to exactly extract the bulk metallic-glass yield strengths with tapered micropillars in micro-compression experiments.

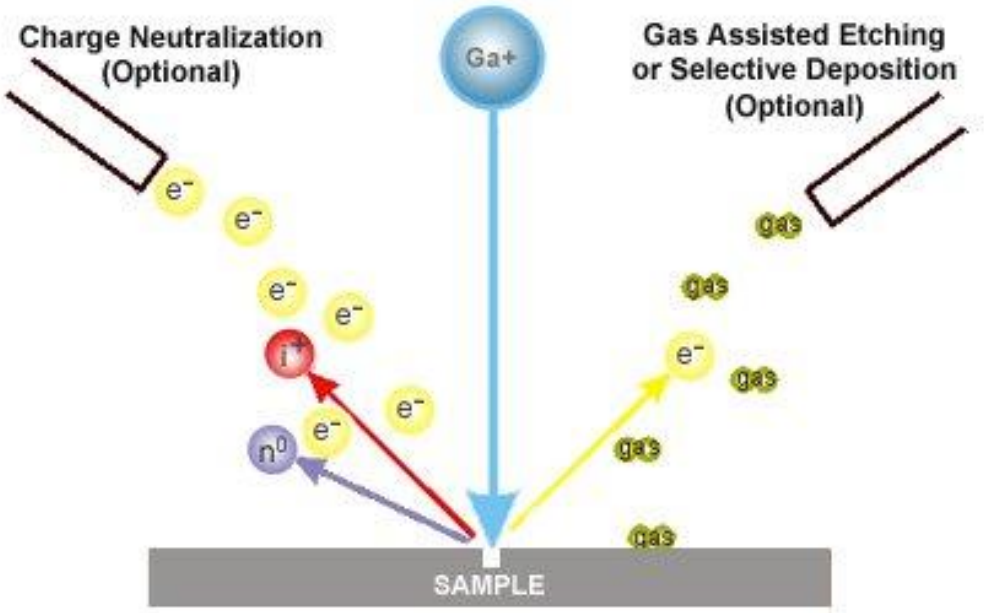

Figure 2.7 The work principle of FIB (this figure is from wiki)

2.5 References

A. Dubach, R. Raghavan, J.F. Loffler, J. Michler and U. Ramamurty (2009). "Micropillar compression studies on a bulk metallic glass in different structural states." Scripta Materialia **60**: 4.

B. Anczykowski, B. Gotsmann, H. Fuchs, J.P. Cleveland and V.B. Elings, (1999). "How to measure energy dissipation in dynamic mode atomic force microscopy." Applied Surface Science **140**: 7.

C.Q. Chen, Y. T. Pei and J.Th.M. De Hosson (2009). "Strength of submicrometer diameter pillars of metallic glasses investigated with in situ transmission electron microscopy." Philosophical Magazine Letters **89**(10): 8.

Changqiang Chen, Yutao Pei and Jeff.Th.M. De Hosson (2010). "A statistical physics consideration about the strength of small size metallic glass pillars." 15th International Conference on the Strength of Materials, Journal of Physics: Conference Series **240**: 5.

Cheng, S., X. Wang, H. Choo and P. Liaw (2007). "Global melting of $Zr_{57}Ti_5Ni_8Cu_{20}Al_{10}$ bulk metallic glass under microcompression " Appl. Phys. Lett. **91**(20): 3.

D. Rugar, H. J. Mamin, R. Erlandsson, J. E. Stern and B. D. Terris (1988). "Force microscope using a fiber-optic displacement sensor." Rev. Sci. lnstrum. **59**(11): 4.

D. Sarid, J. P. Hunt, R.K. Workman, X. Yao and C.A. Peterson, (1998). "The role of adhesion in tapping-mode atomic force microscopy " Applied Physics A: Materials Science & Processing **66**(S1): 4.

Franz J. Giessibl (2003). "Advances in atomic force microscopy." REVIEWS OF MODERN PHYSICS **75**: 35.

G Binnig, CF Quate and C Gerber, (1986). "Atomic force microscope." Phys. Rev. Lett. **56**(9): 4.

Gerhard Meyer and Nabil M. Amer (1990). "Optical-beam-deflection atomic force microscopy: The NaCl (001) surface." Applied Physics Letters **56**(21): 2.

Hans-Jurgen Butt, Brunero Cappell and Michael Kappl (2005). "Force measurements with the atomic force microscope: Technique, interpretation and applications." Surface Science Reports **59**: 152.

J. P. Cleveland, B. Anczykowski, A. E. Schmid and V. B. Elings, (1998). "Energy dissipation in tapping-mode atomic force microscopy." Appl. Phys. Lett. **72**(20): 3.

Javier Tamayo and Ricardo Garc á (1998). "Relationship between phase shift and energy dissipation in tapping-mode scanning force microscopy." Appl. Phys. Lett. **73**(20): 3.

Kuzmin O. V., Pei Y. T. and De Hosson J. T. M., (2011). "In situ compression study of taper-free metallic glass nanopillars." Applied Physics Letters **98**(23): 3.

Lee C. J., J. C. Huang, T. G. Nieh (2007). "Sample size effect and microcompression of $Mg_{65}Cu_{25}Gd_{10}$ metallic glass." Applied Physics Letters **91**(16): 3.

Levi-Setti R. (1974). "Proton scanning microscopy: feasibility and promise." Scanning Electron Microscopy.

M. Radmacher (1997). "Measuring the elastic properties of biological samples with the AFM." IEEE Eng Med Biol Mag **16**(2): 11.

Michael D. Uchic, Dennis M. Dimiduk, Jeffrey N. Florando and William D. Nix (2004). "Sample Dimensions Influence Strength and Crystal Plasticity." Science **305**(5686): 4.

O.V. Kuzmin, Y. T. Pei, C.Q. Chen and J.T.M. De Hosson (2012). "Intrinsic and extrinsic size effects in the deformation of metallic glass nanopillars." Acta Materialia **60**: 10.

Orloff J. and Swanson L. (1975). "Study of a field-ionization source for microprobe applications." J. Vac. Sci. Tech. **12**(6): 5.

R. Garcia, C. J. Gómez, N. F. Martinez, S. Patil, C. Dietz and R. Magerle, (2006). "Identification of Nanoscale Dissipation Processes by Dynamic Atomic Force Microscopy." Phys Rev. Lett. **97**: 4.

Ricardo Garcá, Robert Magerle and Ruben Perez, (2007). "Nanoscale compositional mapping with gentle forces." Nature Materials **6**: 7.

S. Alexander, L. Hellemans, O. Marti, J. Schneir, V. Eiings, P. K. Hansma, Matt Longmire and John Gurley (1989). "An atomic resolution atomicforce microscope implemented using an optical lever." J. Appl. Phys. **65**(1): 4.

S. Manne, H. J. B., S. A. C. Gould and P. K. Hansma (1990). "Imaging metal atoms in air and water using the atomic force microscope." Appl. Phys. Lett. **56**(18): 2.

Sharon Mitchell and Javier Pérez-Ramírez (2010). X-ray diffraction. Surface Science and Methods in Catalysis.

W. H. Escovitz, T. R. Fox and R. Levi-Setti (1975). "Scanning Transmission Ion Microscope with a Field Ion Source." Proceedings of the National Academy of Sciences of the United States of America **72**(5): 3.

Y. Yang, J. C. Ye, J. Lua, F.X. Liu and P.K. Liaw, (2009). "Effects of specimen geometry and base material on the mechanical behavior of focused-ion-beam-fabricated metallic-glass micropillars." Acta Materialia **57**: 11.

Ye JC, Lu J., Yang Y and Liaw PK (2010). "Extraction of bulk metallic-glass yield strengths using tapered micropillars in micro-compression experiments " Intermetallics **18**(3): 9.

Yi Lin, XinCheng Shen, JingJing Wang, Lei Bao, ZhiLing Zhang and DaiWen Pang (2007). "Measuring radial Young's modulus of DNA by tapping mode AFM." Chinese Science Bulletin **52**(23): 4.

3 Structural Inhomogeneity and Anelastic Deformation in Metallic Glasses Revealed by Spherical Nanoindentation

In this charpter, the anelastic deformation of metallic glasses (MGs) at ambient temperature is studied through spherical nanoindentation. A general rheological model, which is linked with the atomic structure of MGs, is proposed to explain the observed anelasticity. The experimental and theoretical results clearly indicate the existence of structural inhomogeneity intrinsic to MGs, which causes the anelastic deformation upon mechanical loading under high loading rates before shear banding occurs. The outcome of the current research provides an important insight into the property-structure relation of MGs.

3.1 Introduction

Since the advent of metallic glasses (MGs) in the 1960s (Klement W., Willens R. H. et al. 1960), understanding their inelastic deformation at ambient temperature has been the issue of intense research efforts (F. Spaepen 1977; A.S. Argon 1979; W.L. Johnson 2005; B. Yang 2006; A. Dubach 2009; J.C. Ye 2009; Y.Q. Cheng 2009; J. C. Ye 2010; Y. Yang 2010). Over the past decades, a variety of deformation models have been proposed to rationalize the observed deformation phenomena in MGs (F. Spaepen 1977; A.S. Argon 1979; W.L. Johnson and K. Samwer 2005; A. Dubach, F.H. Dalla Torre et al. 2009; Y.Q. Cheng, A.J. Cao et al. 2009). Despite the difference in the level of sophistication, all these models were almost built on the same notion that MGs possess intrinsic structural inhomogeneity at the atomic scale which

governs their overall mechanical properties (F. Spaepen 1977; A.S. Argon 1979; W.L. Johnson and K. Samwer 2005; A. Dubach, F.H. Dalla Torre et al. 2009; Y.Q. Cheng, A.J. Cao et al. 2009). Although these models have been successfully used for explaining the quasi-static yielding and post-yielding behaviors in MGs, however, it is still obscure how the inelastic deformation occurs in the apparent elastic deformation regime. Answering this question is not trivial, as the subcritical inelastic deformation events, which eventually trigger the critical yielding phenomena, are sensitive to the material's underlying atomic structure. Nevertheless, the atomic packing in MGs still poses a challenging issue today for materials scientists to resolve (D.B. Miracle, T. Egami et al. 2007; C. Fan, P.K. Liaw et al. 2009). In view of these, studying the subcritical inelastic deformation events that carry structural 'fingerprints' may help us decode the nature of atomic packing in MGs.

3.2 Material and Experiment

To unveil the pre-yielding inelastic deformation mechanism, a spherical nanoindentation approach is proposed in this study. A Zr-based MG sample, which has the chemical composition of $Zr_{55}Pd_{10}Cu_{20}Ni_5Al_{10}$ (in atomic %), was selected as the model material because of its availability. Prior to the indentation experiments, the amorphous nature of the MG alloy was confirmed using X-ray diffraction analyses (shown in Fig. 3.1) and the surface of the MG sample was mechanically polished by a paste with Al_2O_3 particles to a smooth finish with a roughness (usually less than 10nm) at the nanometer scale for nanoindentation. The nanoindentation experiments were subsequently performed with the low-load Hysitron™ NanoIndenter system (Hysitron Inc, Minneapolis, MN) with a 5-μm spherical nanoindenter, which possesses the resolution of ~ 1 nm in displacement and ~ 1 μN in load. Owing to its ultrafast data acquisition

rate, which is ~10,000 points per second, unusually high loading rates can be programmed and applied during nanoindentation. As a mechanical assembly, the damping factor of the whole system was characterized to be around ~0.014 kg s^{-1}. Such a machine damping factor will result in an 'artificial' viscosity of about ~0.05 MPa s when deforming a material volume with a microscopic dimension, which is negligibly small and would not affect the experimental results as can be seen later.

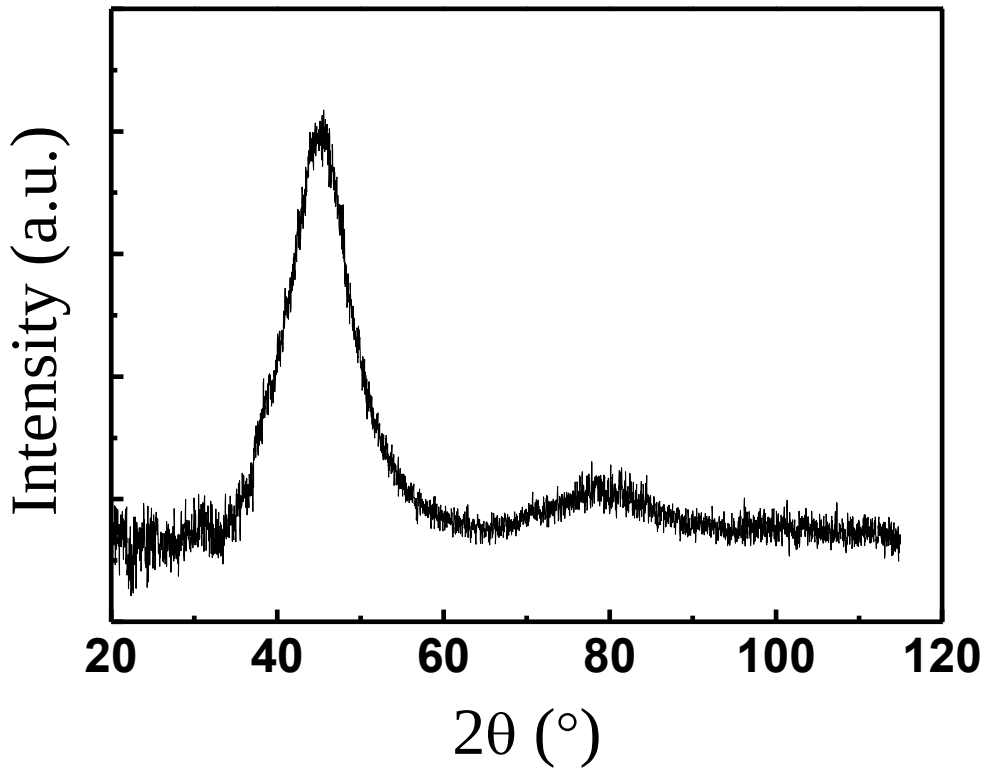

Figure 3.1 The XRD pattern of bulk metallic glass $Zr_{47}Cu_{46}Al_7$

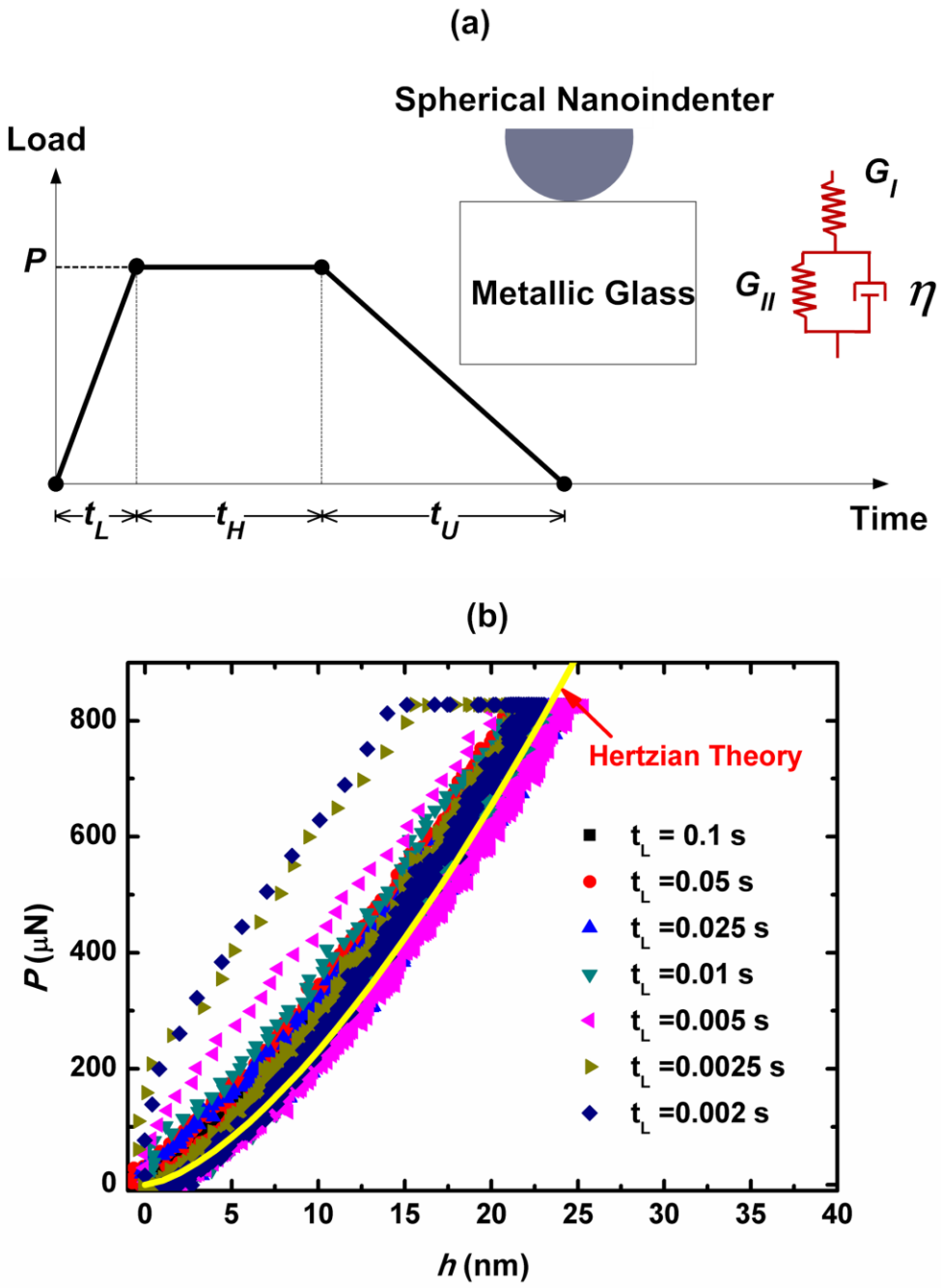

Figure 3.2 (a) The sketch of the indentation loading profile [the insets: the sketch of the spherical nanoindenter and MG sample (left) and the three-parameter rheological model for MGs (right)], and (b) the indentation load-displacement curves which show anelastic deformation occurring at fast loading rates (the quasi-static Hertzian response corresponds to a indenter tip radius of ~ 5 μm, a material's Young's modulus of ~ 76 GPa and a Poisson's ratio of ~0.365).

As shown in Fig.3.2a, a trapezoid-like loading profile was programmed for the nanoindentation experiments, which consists of three segments, namely, loading, holding and unloading, as in usual nanoindentation experiments. The loading time, t_L, was systematically varied to amplify the inelastic response of the MG, while the unloading time, t_U, was fixed at ~ 0.1 s to warrant its full recovery. In doing so, any residual plastic deformation can be detected after the unloading. The holding time, t_H, was set at a somewhat arbitrary value of ~ 0.1 s for monitoring the material's transient dynamic response. Figure 3.2b displays the typical load-displacement curves obtained from indenting the Zr-based MG at a constant load of 800 μN and varying t_L. From Fig. 3.2b, it is evident that all curves return to the zero displacement after unloading, implicative of the elastic nature of the material's response. For $t_L > 0.01$ s, the loading and unloading curves overlap obeying the classic Herztian theory (Fig. 3.2b). In contrast, the loading curves deviate significantly from the Herztian theory for fast loading at $t_L < 0.01$ s. During the holding time, the material 'creeps' all the way to the corresponding Herztian point and then follows the Herztian response in unloading. Based on the work of Packard et al (C.E. Packard and C.A. Schuh 2007), the yielding load, $P_{y,}$ for typical Zr-based MGs can be estimated around ~ 4000 μN in spherical indentation with a tip radius of ~ 5 μm, which means that the deformation under the indentation load less than P_y should be elastic in nature, as consistent with our experimental results.

3.3 Results and Discussion

Recent atomistic simulations and experiments suggest that MGs be a mixture of solid- and liquid-like atomic clusters (D.B. Miracle, T. Egami et al. 2007; C. Fan, P.K. Liaw et al. 2009;

M.D. Demetriou, W.L. Johnson et al. 2009; Y.Q. Cheng, A.J. Cao et al. 2009; J. C. Ye, C. T. Liu et al. 2010). Even in the apparent elastic deformation regime, their deformation mechanism still consists of the uncorrelated inelastic deformation of the liquid-like atomic clusters and the pure elastic deformation of the solid-like ones (M.D. Demetriou, W.L. Johnson et al. 2009; Y.Q. Cheng, A.J. Cao et al. 2009). Such a physical picture of deformation is close to the shear-transformation-zone (STZ) theory proposed by Argon (A.S. Argon 1979); however, the topological relation between the liquid- and solid-like atomic clusters is vague. According to the STZ theory (A.S. Argon 1979), the STZs behave essentially as the liquid-like atomic clusters, accommodating the inelastic deformation as an analogue of dislocations for crystalline materials. Furthermore, the STZs were postulated to be encaged by some kind of elastic media; nevertheless, the origin and structure of these elastic media were not clear then.

According to Ma and co-workers (D. Ma, A.D. Stoica et al. 2009), the solid-like atomic clusters, which are responsible for the short-range order in MGs, form a percolating system in MGs. In view of these, it is reasonable to propose that the solid-like atomic clusters act essentially as the elastic media. Therefore, the whole atomic structure of a MG alloy can be mechanistically simplified as a rheological three-parameter model, as shown by the inset of Fig. 3.1a. In the Kelvin unit, the dashpot is equivalent to the liquid-like atomic clusters or STZs, and the spring to the solid-like atomic clusters encaging STZs. For generality, a second spring connected in series to the Kelvin unit is also assumed, which physically corresponds to the solid-like atomic clusters, if there were any, not interacting with any STZs. It should be emphasized here that there may be other rheological models available for anelastic solids; however, the three-parameter model was found to have the widest range of application (L. Cheng, X. Xia et al.

2005). Furthermore, as the essential of the underlying physics has been captured by the current model, any attempts towards a higher level of sophistication in modeling may just further complicate the following derivation. In such a case, we will keep our analysis within the analytic framework of the three-parameter model for simplicity.

For an elastic Hertzian contact, the load-displacement relation can be expressed as $h^{3/2} = 3P(1-\nu)/8GR^{0.5}$, where h is the indent depth; P is the indentation load; ν is the material's Poisson's ratio, G is the shear modulus and R is the indenter tip radius. For an anelastic solid as shown by the inset of Fig. 3.1b, the loading curve can be derived from the Hertzian solution using the integral transform method (R.M. Christensen 1982), which is:

$$h(t)^{3/2} = h_0(t)^{3/2} - \frac{3\dot{P}(1-\nu)t_c}{8\sqrt{R}G_{II}}\left[1-\exp\left(-\frac{t}{t_c}\right)\right] \tag{3.1}$$

Where $\dot{P}$ is the loading rate; G_{II} is the shear modulus of the spring in the Kelvin unit; t_c is the material's relaxation time and equals η/G_{II} with η being the viscosity of the dashpot; and $h_0(t)$ is the Hertzian solution:

$$h_0(t)^{3/2} = \frac{3P(t)(1-\nu)}{8\sqrt{R}}\left(\frac{1}{G_I}+\frac{1}{G_{II}}\right) \tag{3.2}$$

Where G_I is the shear modulus of the spring connected with the Kelvin unit in series. It should be noted that Eq. (3.1) is only valid for the loading curve due to the limitation of the

integral transform method (R.M. Christensen 1982). For simplicity, a constant Poisson's ratio is assumed for both springs in deriving Eqs. (3.1) to (3.2). Details of the above formula derivation are shown in section 3.4.

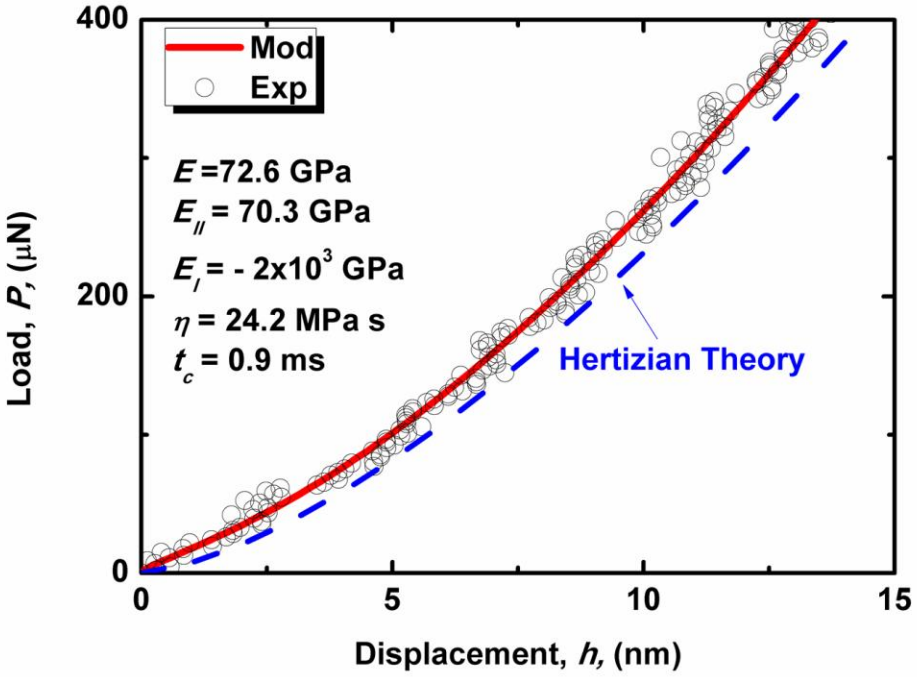

Figure 3.3 The comparison of the loading curves obtained from the experiment and theory corresponding to the loading time of 0.03 s (note that the Hertizian response corresponds to E = 72.6 GPa).

Treating G_I, G_{II} and t_c as the three unknowns, their values can be extracted from the experimental data through nonlinear data fitting. Note that Eq. (3.1) is a viscoelastic solution; however, any nonlinearity in the materials behavior can be detected if t_c or η obtained at different loading or loading rates differs. Figure 3.3 shows the comparison of the loading curves obtained from the experiments and the viscoelastic model. It is evident that the current model can fit the experimental results very well despite its simplicity. Interestingly, it was found that $1/G_{II}$

$\approx 1/G_I + 1/G_{II}$ through data fitting, which means that the overall shear modulus, G, of the MGs is close to that of the spring in the Kelvin unit. In such a case, the fitted value of G_I was either unreasonably high or even negative, which was just a numerical artifact resulting from the divergence of G_{II} (Fig. 3.3). Physically, this behavior implies that the atomic packing in MGs does not allow for the existence of such solid-like atomic clusters that can deform without disturbing any liquid-like atomic clusters. In other words, both types of atomic clusters are highly coupled in MGs and the liquid-like ones are well 'dispersed' in the amorphous structure, frustrating any long-range order brought about by the solid-like ones. Therefore, the whole atomic structure of the MGs can be further modeled just as the Kelvin unit, which agrees with the recent finding from the dynamic microcompression experiments (J. C. Ye, C. T. Liu et al. 2010).

Considering the possible nano-scale materials inhomogeneity (Y. Yang, J. C. Ye et al. 2010), the viscoelastic properties, which are capable of representing the whole MG alloy, was finally obtained by fitting a general trend as shown in Fig. 3.4, which presents the variations of the indentation depth, h_p, corresponding to a given indentation load, P, with different loading time, t_L, in comparison with the theoretical results. Note that the theoretical curves were obtained by directly fitting the experimental t_L-h_p data with Eq. (3.1). Evidently, the model captures the general trend of the experimental data very well. As the loading time is shortened, the MGs appear to be 'stiffer' because of the rate dependent deformation characteristics of the liquid-like atomic clusters 'dispersed' in the glassy atomic structure. The transition from the quasi-static to dynamic response occurs at the time of about ~0.01 s, which is about 10 times the average relaxation time of the MG. The fitted viscoelastic properties, such as E, η and t_c, are listed in

Table 3.1, from which it can be seen that the overall elastic moduli and viscosity of the MG exhibit the load independence, which indicates a Newtonian flow behavior of the liquid-like atomic clusters at ambient temperature.

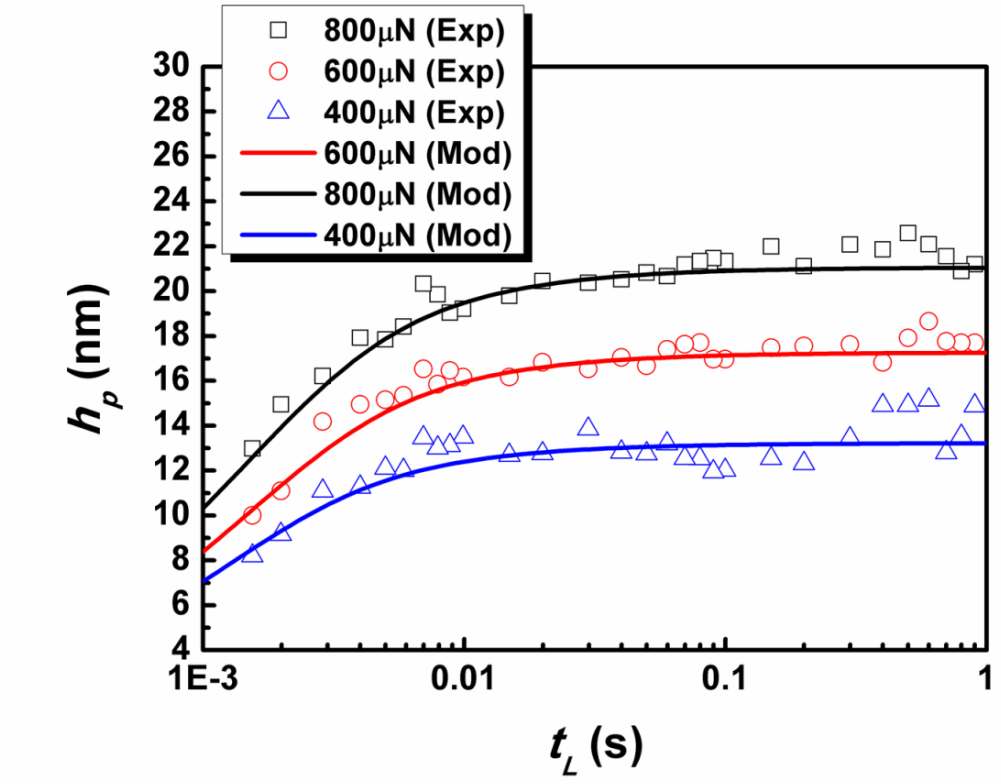

Figure 3.4 The variation of the indentation depth, h_p, with the loading time, t_L, at different indentation loads for $Zr_{55}Pd_{10}Cu_{20}Ni_5Al_{10}$ MG.

Table 3.1 The viscoelastic properties of $Zr_{55}Pd_{10}Cu_{20}Ni_5Al_{10}$ MGs were extracted by fitting the experimental data on Fig. 3.4.

	Zr-based MG (ν = 0.365)		
Load (μN)	400 μN	600 μN	800 μN
E (GPa)	76.5	76.9	76.2
t_c (ms)	0.9	1.1	1.1
η (MPa s)	25.9	31.6	31.2

From the viewpoint of potential energy landscape (PEL) (W.L. Johnson and K. Samwer 2005; J. C. Ye, C. T. Liu et al. 2010), the extracted viscosity, η, can be related to the concentration, χ, of the liquid-like atomic clusters, and their activation energy U_β for β relaxation. Such a relation can be simply expressed as $\eta \sim \chi \exp(U_\beta/RT)$, where R and T denotes the gas constant and ambient temperature, respectively (A.S. Argon 1979; J. C. Ye, C. T. Liu et al. 2010). According to the recent work of Yu et al. (H.B. Yu, W.H. Wang et al. 2010), $U_\beta \sim 26\ RT_g$ for MGs, where T_g is the glass transition temperature. As such, η can be expressed as $\chi \exp(26T_g/T)$. Therefore, the constancy of η indicates a steady concentration of the liquid-like atomic clusters prior to shear banding. Note that such a physical picture have long been provided by simulation results (Y.F. Gao, B. Yang et al. 2007; M.Q. Jiang 2009) but they have never been experimentally justified.

3.4 Summary

In summary, we devised a simple nanoindentation approach in this chapter to reveal and characterize the anelastic behavior of MGs. The experimental results clearly show that MGs consist of ‘soft’ and ‘hard’ phases at the atomic scale, which leads to the anelastic deformation behavior at ambient temperature. As such, MGs are better to be viewed as anelastic instead of elastic solids. Such a paradigmatic shift in the theoretical modeling of the pre-yielding behavior may provide insights into the atomic-scale deformation mechanism of plasticity in MGs.

Appendix: Theoretical Analyses of Viscoelastic/Anelastic Spherical Nanoindentation

In principle, there are many mechanical models one can choose for the study of viscoelasticity or anelasticity in solids. The simplest one is the Kelvin model, as shown in Fig. 3.5. It can be represented by a purely viscous damper and purely elastic spring connected in parallel with a constitutive relationship shown by Eq. 3.3. A much more general mechanical model is the three-parameter model, which consists of a Kelvin unit and a spring arranged in series (Fig 3.6) and has its constitutive relationship shown by Eq. 3.4.

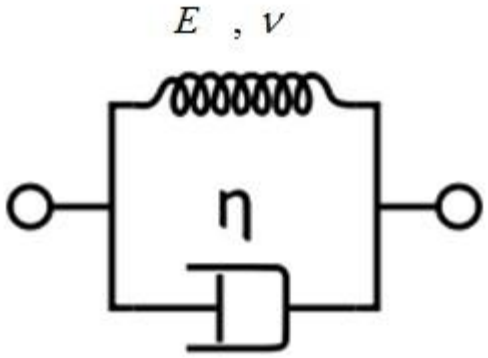

Figure 3. 5 Schematic representation of Kelvin model

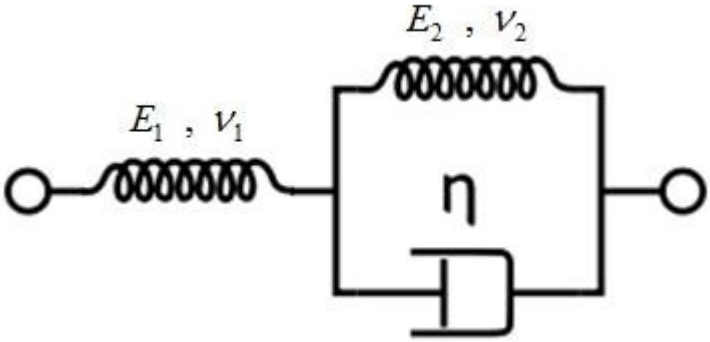

Figure 3. 6 Schematic representation of three-parameter model

$$\sigma = E\varepsilon + \eta\dot{\varepsilon} \tag{3.3}$$

$$\sigma + \frac{\eta}{E_1 + E_2}\dot{\sigma} = \frac{E_1 E_2}{E_1 + E_2}\varepsilon + \frac{E_1 \eta}{E_1 + E_2}\dot{\varepsilon} \tag{3.4}$$

For a Hertzian contact, the load-displacement relation is:

$$h^{3/2} = \frac{3P\left(1-\nu^2\right)}{4\sqrt{R}E} = \frac{3P\left(1-\nu\right)}{8\sqrt{R}G} \tag{3.5}$$

$$G = \frac{E}{2\left(1+\nu\right)}$$

In which the load function for the loading and holding segments can be written as:

$$P\left(t\right) = \begin{cases} \dfrac{P_0}{t_L} t & \left(t \le t_L\right) \\ \\ P_0 & \left(t \ge t_L\right) \end{cases} \tag{3.6}$$

where P_0 is the peak load and t_L is the loading time. Applying the integral transform principle (Lokenath Debnath and Dambaru Bhatta 2007), one can obtain the following formula for a viscoelastic material indented the same way as dictated by Eq. (3.6):

$$h\left(t\right)^{3/2} - h_0{}^{3/2} = \begin{cases} \dfrac{3\dot{P}_0\left(1-\nu_2^2\right)}{4\sqrt{R}E_2}\left[t - t_c\left(1-e^{-\frac{t}{t_c}}\right)\right] & \left(0 \le t < t_L\right) \\ \\ \dfrac{3\dot{P}_0\left(1-\nu_2^2\right)}{4\sqrt{R}E_2}\left[t_L - t_c e^{-\frac{t}{t_c}}\left(e^{\frac{t_L}{t_c}} - 1\right)\right] & \left(t_L < t\right) \end{cases}$$

$$h_0^{3/2} = \frac{3\dot{P}_0\left(1-\nu_1{}^2\right)t}{4\sqrt{R}E_1} \tag{3.7}$$

$$t_c = \frac{\eta}{G_2}$$

Here, h_0 is the response from the left spring, $\dot{P}_0$ is the loading rate. Likewise, we can also derive the following load-displacement relation for the Kelvin model:

$$h(t)^{3/2} = \begin{cases} \dfrac{3\dot{P}_0\left(1-\nu^2\right)}{4\sqrt{R}E}\left[t - t_c\left(1-e^{-\frac{t}{t_c}}\right)\right] & \left(0 \le t < t_L\right) \\ \dfrac{3\dot{P}_0\left(1-\nu^2\right)}{4\sqrt{R}E}\left[t_L - t_c e^{-\frac{t}{t_c}}\left(e^{\frac{t_L}{t_c}}-1\right)\right] & \left(t_L < t\right) \end{cases} \tag{3.8}$$

$$t_c = \frac{\eta}{G_2}$$

Based on the above derivations, the relationship between the loading time and the displacement at the end of the loading segment can be described as:

$$h\left(t_L\right)^{3/2} - \frac{3\dot{P}_0\left(1-\nu_1{}^2\right)t_L}{4\sqrt{R}E_1} = \frac{3\dot{P}_0\left(1-\nu_2^2\right)}{4\sqrt{R}E_2}\left[t_L - t_c\left(1-e^{-\frac{t_L}{t_c}}\right)\right] \tag{3.9a}$$

$$h\left(t_L\right)^{3/2} = \frac{3\dot{P}_0\left(1-\nu^2\right)}{4\sqrt{R}E}\left[t_L - t_c\left(1-e^{-\frac{t_L}{t_c}}\right)\right] \tag{3.9b}$$

where Eq. 3.9a is for the three-parameter solid model and Eq. 3.9b for the Kelvin model. Using the above equations, the viscoelastic properties of the $Zr_{55}Pd_{10}Cu_{20}Ni_5Al_{10}$ and $Mg_{58}Cu_{31}Nd_5Y_6$ metallic glass can be fitted out the same way as described in the main text, as shown in Fig. 3.7 and 3.8, respectively. Also shown in Table 3.2 and 3.3 are the fitted corresponding viscoelastic

properties of the above two MGs. Note that in fitted properties all came from the Kelvin model while the three-parameter model yields a G_1 approaching infinity.

Table 3.2 The viscoelastic properties of the $Zr_{64.13}Cu_{15.75}Ni_{10.12}Al_{10}$ MGs were extracted by fitting the experimental data at different peak load.

	$Zr_{64.13}Cu_{15.75}Ni_{10.12}Al_{10}$ MG ($\nu = 0.365$)		
Load (μN)	600 μN	800 μN	1000 μN
E (GPa)	70.0	67.9	68.5
t_c (ms)	2.1	2.4	1.7
η (MPa s)	51.6	53.3	49.4

Table 3.3 The viscoelastic properties of the $Mg_{58}Cu_{31}Nd_5Y_6$ MGs were extracted by fitting the experimental data at different peak loads

	$Mg_{58}Cu_{31}Nd_5Y_6$ MG ($\nu = 0.31$ (Shao-Gang Wang, Ling-Ling Shi et al. 2010))		
Load (μN)	200 μN	600 μN	800 μN
E (GPa)	47.7	38.4	44.5
t_c (ms)	2.6	2.7	1.8
η (MPa s)	34.0	30.4	31.2

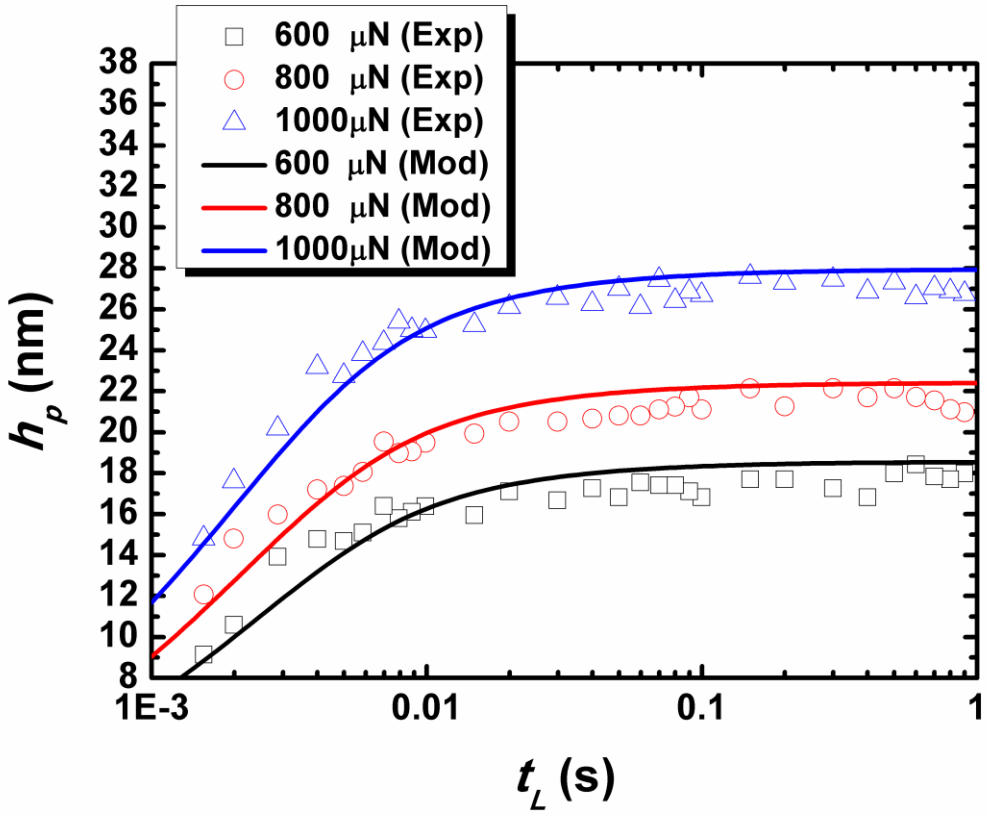

Figure 3.7 The variation of the indentation depth, h_p, with the loading time, t_L, at different indentation loads for $Zr_{64.13}Cu_{15.75}Ni_{10.12}Al_{10}$ MG.

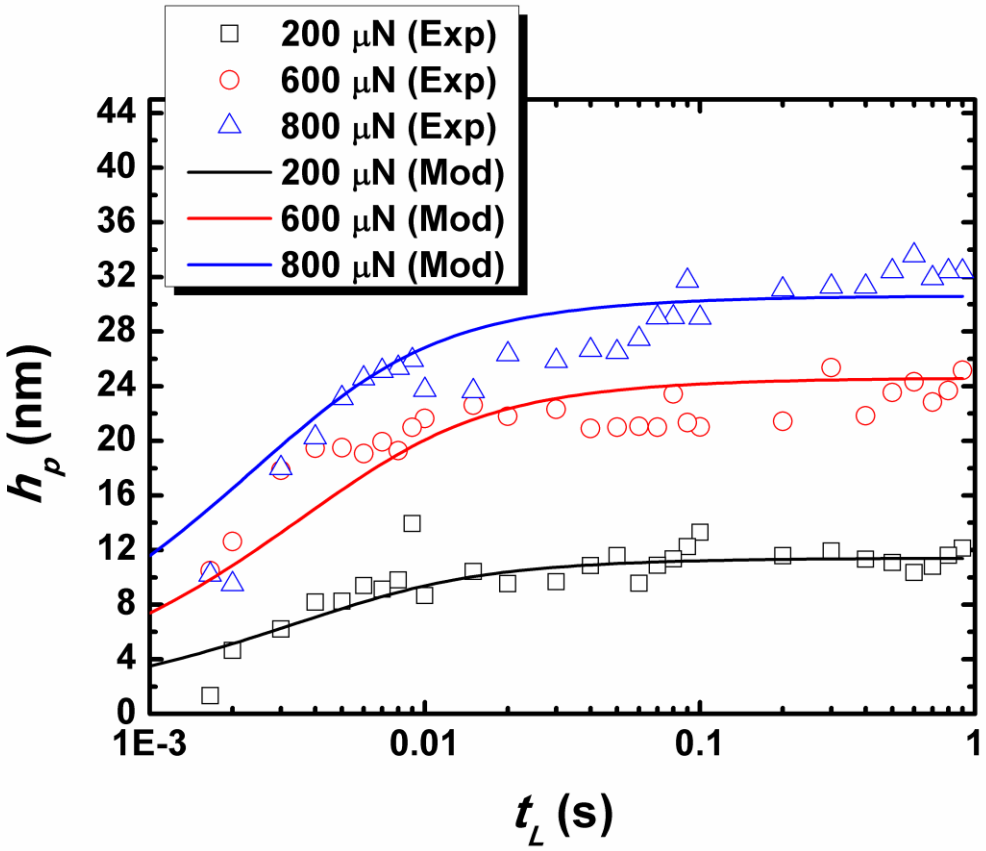

Figure 3.8 The variation of the indentation depth, h_p, with the loading time, t_L, at different indentation loads for $Mg_{58}Cu_{31}Nd_5Y_6$ MG

3.5 References

A. Dubach, F. H. Dalla Torre and J.F. Loffler, (2009). "Constitutive model for inhomogeneous flow in bulk metallic glasses." Acta Mater. **57**: 12.

A.S. Argon (1979). "Plastic deformation in metallic glasses." Acta Metall. **27**(1): 12.

C. Fan, P. K. Liaw and C. T. Liu, (2009). "Atomistic model of amorphous materials." Intermetallics **17**: 2.

C.E. Packard and C. A. Schuh (2007). "Initiation of shear bands near a stress concentration in metallic glass." Acta Mater. **55**: 11.

D. Ma, A. D. Stoica and X.-L. Wang, (2009). "Power-law scaling and fractal nature of medium-range order in metallic glasses." Nature Mater. **8**(1): 5.

D.B. Miracle, T. Egami, K.M. Flores and K. F. Kelton, (2007). "Structural aspects of metallic glasses." MRS Bulletin **32**: 6.

F. Spaepen (1977). "A microscopic mechanism for steady state inhomogeneous flow in metallic glasses." Acta Metall. **25**(4): 9.

H.B. Yu, W. H. Wang, H.Y. Bai, Y. Wu and M. W. Chen, (2010). "Relating activation of shear transformation zones to β relaxations in metallic glasses." Phys. Rev. B **81**(22): 4.

J. C. Ye, C. T. Liu, Q. Wang and Y. Yang (2010). "Atomistic Free-Volume Zones and Inelastic Deformation of Metallic Glasses." Nature Materials **9**(8): 5.

Klement W., Willens R. H. and Duwez POL, (1960). "Non-crystalline Structure in Solidified Gold-Silicon Alloys." Nature(187): 2.

L. Cheng, X. Xia, L.E. Scriven and W.W. Gerberich, (2005). "Spherical-tip indentation of viscoelastic material." Mech. Mater. **37**: 14.

Lokenath Debnath and Dambaru Bhatta (2007). Integral Transforms and Their Applications.

M.D. Demetriou, W. L. Johnson and K. Samwer, (2009). "Coarse-grained description of localized inelastic deformation in amorphous metals." Appl. Phys. Lett. **94**: 3.

M.Q. Jiang, L. H. L. (2009). "On the origin of shear banding instability in metallic glasses " J. Mech. Phys. Solids **57**: 26.

R.M. Christensen (1982). Theory of Viscoelasticity, Dover Publications.

Shao-Gang Wang, Ling-Ling Shi and Jian Xu, (2010). "Mg-based bulk metallic glasses: Elastic properties and their correlations with toughness and glass transition temperature " Journal of Materials Research **26**(7): 11.

W.L. Johnson and K. Samwer (2005). "A universal criterion for plastic yielding of metallic glasses with a $(T/Tg)^{2/3}$ temperature dependence." Phys. Rev. Lett. **95**: 4.

Y. Yang, J. C. Ye, J. Lu, Q. Wang and P.K. Liaw, (2010). "Revelation of the effect of structural heterogeneity on microplasticity in bulk metallic-glasses." J. Mater. Res. **25**(3): 13.

Y.F. Gao, B. Yang and T.G. Nieh, (2007). "Thermomechanical instability analysis of inhomogeneous deformation in amorphous alloys." Acta Mater. **55**: 9.

Y.Q. Cheng, A. J. Cao and E. Ma, (2009). "Correlation between the elastic modulus and the intrinsic plastic behavior of metallic glasses: The roles of atomic configuration and alloy composition." Acta Mater. **57**: 15.

4. The Structural versus Mechanical Origin of Strain Softening in Bulk Metallic-Glass

Numerous prior studies have shown that bulk metallic-glasses (BMGs) could be severely 'softened' by profuse shear-banding. While it is popular to attribute this softening behavior to a mechanism of 'defect' accumulation in the BMG literature, such as the creation of additional 'free-volume' around shear bands, however, through a series of carefully designed macro- and micro-mechanical experiments, we here show that, for our severely bent Zr-based BMGs, the witnessed mechanical softening is directly related to the presence of residual stress rather than to any genuine materials softening. Our finding implies that, other than defect accumulation, other possible structural mechanisms may prevail in stable shear-banding events which can lead to the apparent strain softening in BMGs.

4.1 Introduction

Since their advent in the 1960s, metallic glasses (MGs), and later their bulk forms [the so-called 'bulk metallic glasses' (BMGs)] (A. Inoue, H. Yamaguchi et al. 1990) that was successfully obtained only in the 1990s, have received extensive attentions for their superb strength and hardness, excellent corrosion (Y. Waseda and K. T. Aust 1981; T.C. Chieh, J. Chu et al. 2003)and wear resistance (Nozomu Togashi, Mamoru Ishida et al. 2008). Because of their unique mechanical properties, BMGs are often being deemed as a promising engineering material for structural applications. However, their poor ductility (Johnson W. L. 2002; C. A.

Schuh, T. C. Hufnagel et al. 2007) at room temperature, especially under a tension stress, constitutes the major hindrance to their structural use.

Unlike crystalline metals, in which extensive plasticity comes along with strain hardening (A.A. Salem, S.R. Kalidindi et al. 2005; Abhijit P. Brahme, Kaan Inal et al. 2011), BMGs usually exhibit a strain-softening behavior when shear banding occurs (Mingwei Chen, Akihisa Inoue et al. 2006; Mingwei Chen 2008; Byung-Gil Yoo, Kyoung-Won Park et al. 2009). Consequently, the shear-softened BMGs tend to fracture in a catastrophic manner, thereby leading to limited ductility under uniaxial loadings or even under bending for some cases. Over the past years, there is a continuing research effort to understand the physical origin that causes the phenomenon of the 'shear-induced softening' in BMGs (Alain Reza Yavari, Alain Le Moulec et al. 2005; Yunfeng Shi and Michael L. Falk 2005; H. Bei, S. Xie et al. 2006; M.Q. Jiang and L.H. Dai 2009; D. Pan, H. W. Liu et al. 2010).

Numerous previous studies (H. Bei, S. Xie et al. 2006; J. Pan, Q. Chen et al. 2011) related this 'shear-induced softening' to the creation and nucleation of free volume. According to this theory, the content of free volume increases with plastic strain, causing softening in BMGs. Kanungo et al. (Biraja P. Kanungo, Stephen C. Glade et al. 2004) examined the changes in free volume associated with shear band formation in Cu- and Zr-based BMGs using positron annihilation spectroscopy (PAS) and differential scanning calorimetry (DSC) . Their results indicated that the concentration of the free volume increased following plastic deformation. Through microstructural analyses, Steif (P.S. Steif, F. Spaepen et al. 1982), Li (Jing Li, F. Spaepen et al. 2002), and Yavari (Alain Reza Yavari, Alain Le Moulec et al. 2005) also proposed

that there was an increase in free volume in the deformed BMGs relative to those undeformed. Along a same line, H. Bei et al. (H. Bei, S. Xie et al. 2006) also suggested the observed softening under profuse shear banding was due to the additional free volume in the sheared region.

In order to quantify this shear-induced softening behavior, many researchers also relied on the measured mechanical properties of BMGs. For example, Bei et al. (H. Bei, S. Xie et al. 2006) found that the measured hardness of plastically deformed MGs was decreased with the increase of plastic strain and argued that this is due to an increasing shear-band thickness and free-volume concentration. Following the same line of reasoning, Song et al. (M. Song, Y. Y. Sun et al. 2012) also argued that, after altering the glassy structure of a BMG through either shear-banding or heat treatment, the hardness and elastic modulus of the BMG could be altered by changing the free volume concentration. In such a case, higher hardness and elastic modulus could be obtained with a less concentration of free volume in BMGs. Interestingly, contradictory results were also reported. For instance, Yu et al. (P. Yu, K.C. Chan et al. 2011) observed an increase in hardness after plastic compression and attributed this apparent hardening to plasticity-induced structural densification; however, the results of Yu et al. are contradictory to those reported from many other groups (Wei Hua Wang, Hai Yang Bai et al. 2000; H. Bei, S. Xie et al. 2006; Kou Hongchao, Wang Jun et al. 2011).

Other than the free-volume theory (M. H. Cohen and Turnbull 1959), an alternative mechanism related to residual stress was also proposed to explain the strain-induced softening in BMGs. For example, Wang et al. (L. Wang, H. B. et al. 2011) deliberately introduced tensile and compressive residual stress into a BMG bend bar after plastic bending, and found that the

hardness of the BMG decreased greatly with a tensile residual stress but increased only slightly with a compressive residual stress even at the presence of shear banding . Likewise, Chen et al. (L.Y. Chen, Q. Ge et al. 2008) also considered that a compressive residual stress is responsible for the increase in the hardness of deformed BMGs. Since plasticity in solids usually comes along with residual stress, these results suggest that there could be two possible mechanisms responsible for strain softening in BMGs, i.e. structural alteration, such as free-volume creation, versus residual stress. However, at the present time, it is still not clear which one plays the dominate role when strain softening occurs.

In this study, we intend to address the above issue through a series of macro- and micro-mechanical tests. To this end, we designed a plastic bending test which enables us to easily apply a severe plastic deformation in BMGs. After the plastic bending, we measured the local elastic modulus and hardness across the thickness of the BMG bend bars using the Joslin-Oliver-based nanoindentation (J.E. Jakes, C.R. Frihart et al. 2009) and the microcompression method, which allow us to characterize the micromechanical properties with and without the presence of residual stress and also in the regions of geometrical discontinuities. No matter which mechanism is operative, a comparative study will be finally performed to provide the critical evidence for an experimental verification.

4.2 Material

For the synthesis of the bulk-metallic glass, high-purity metals including Zr (99.9 at.%), Cu (99.99 at.%) and Al (99.99 at.%) were used. The master alloy with a nominal atomic percentage composition of $Zr_{47}Cu_{46}Al_7$ was fabricated by arc melting under a Ti-gettered high-purified

argon atmosphere on a water-cooled copper hearth. During the fabrication, the ingot was re-melted at least five times to ensure the homogeneous distribution of their chemical composition. The structure of the BMG samples was examined by X-ray diffractometry (XRD, Co radiation) before and after the plastic bending. As shown in Fig 4.1, these XRD patterns only display a broad diffraction maximum without any detectable sharp Bragg peaks, indicative of an overall amorphous structure even after the plastic deformation.

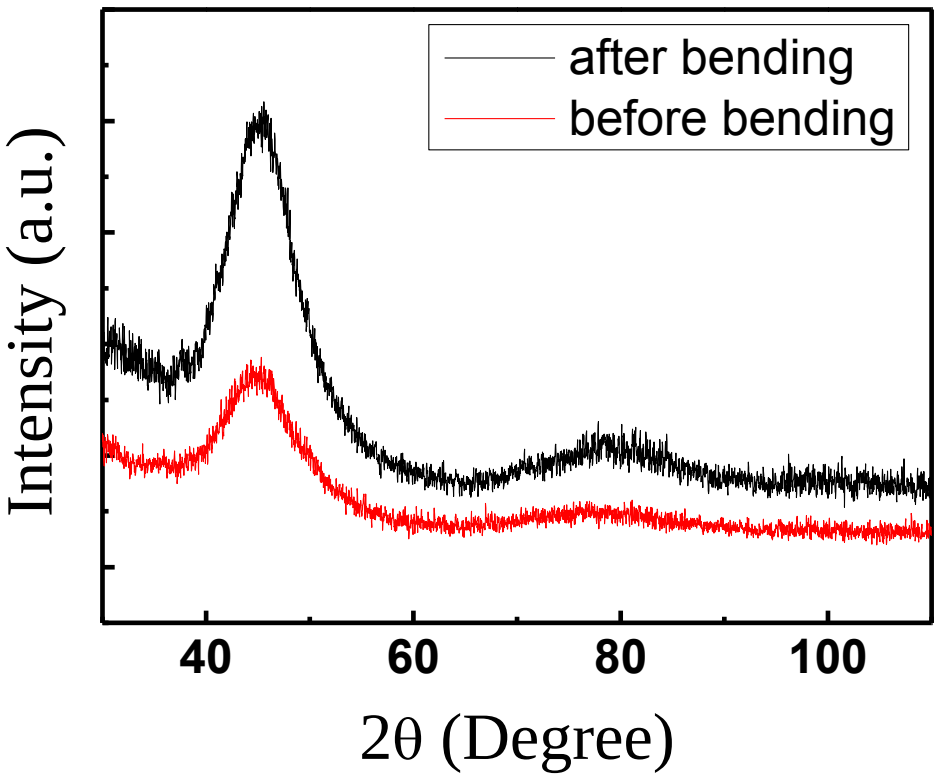

Figure 4.1 The XRD patterns of $Zr_{47}Cu_{46}Al_7$ metallic glass before and after bending.

4.3 Experiment

For the bending experiments, three bending samples (or slices) with the dimension of 10mm×3mm×0.42mm were prepared through the sectioning from a same BMG plate. Before bending, the lateral (10mm×0.42mm) and top surfaces (10mm×3mm) of the slices were mechanically polished to a mirror finish to facilitate the examination of shear-banding morphologies. With one end fixed, the slices were subsequently pushed at the free end against the mandrels with different diameters, as shown in Fig 4.2(a). Unlike the regular 3- or 4-point bending experiments (R. Busch, W. Liu et al. 1998; G.Y.Wang, P.K. Liaw et al. 2008; G.Y. Wang, P.K. Liaw et al. 2012; Jinn P. Chu, J.E. Greene et al. 2012), this experimental set-up can readily lead to a severe plastic deformation of the slices. After bending, shear bands exposed on the lateral surfaces of the slices were imaged by scanning electron microscopy (SEM) (JEOL Model JSM-6490, Japan).

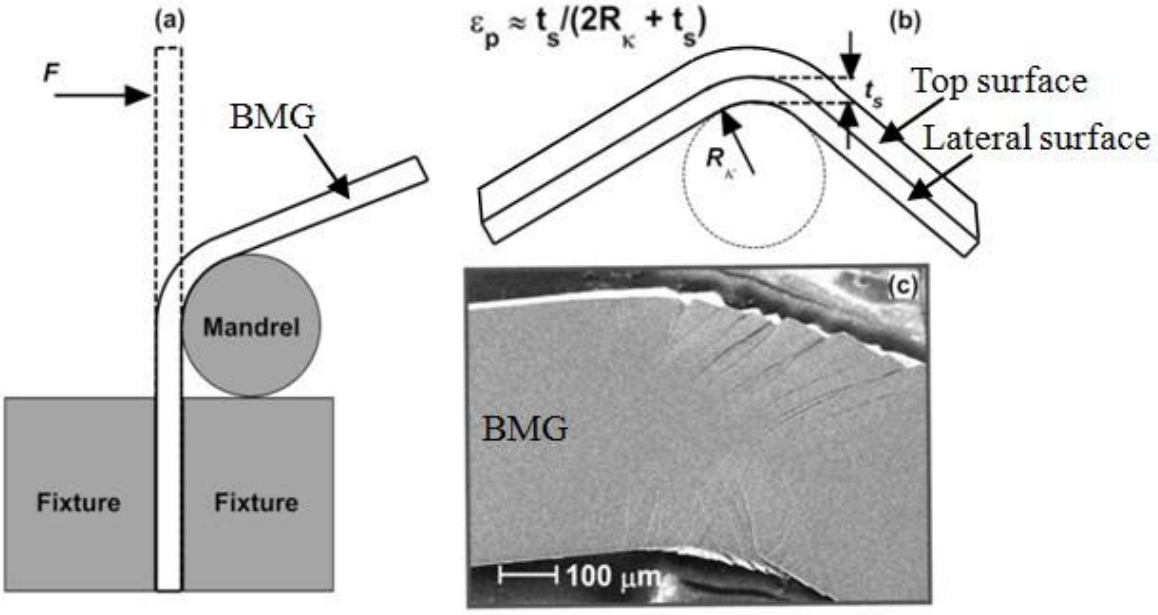

Figure 4.2 The sketches of (a) the experimental setup, (b) the bent configuration of one BMG sample and (c) a SEM image showing the shear band distribution in the severely plastically deformed region of the BMG sample.

Subsequently, the local elastic modulus and hardness (or yield strength) were measured by nanoindentation and microcompression. To that end, the plastically deformed BMG slices were cold-mounted into epoxy resin blocks for fixation. As conforming to the basic requirements for nanoindentation, the lateral surfaces of the BMG slices were again mechanically polished to remove surface irregularities resulting from the previous plastic deformation. Here, it needs to be emphasized that, due to an indentation 'edge effect' (N. Schwarzer, I. Hermann et al. 2001; J.E. Jakes, C.R. Frihart et al. 2008; J.E. Jakes, C.R. Frihart et al. 2009; S.Q. Shu, Y. Yang et al. 2009; Y. Zhao and T. C. Ovaert 2010), the original Oliver-Pharr method (Oliver W.C. and Pharr G.M. 1992) cannot be directly applied here to measure the local mechanical properties of the BMG slices, particularly in the areas close to their edges. To resolve this issue, the Joslin-Oliver

method (J.E. Jakes, C.R. Frihart et al. 2009) was employed, the details of which were described in the following text and therefore omitted here for brevity. To rule out the possible residual stress effect (Min Ha Lee, Joong Hwan Jun et al. 2010; L. Wang, H. B. et al. 2011), microcompression was subsequently conducted for local mechanical characterization. Using the ion-beam milling method (Y. Yang, J.C. Ye et al. 2009; Ye JC, Lu J et al. 2010), micropillars with the same dimension, ~5μm in height and ~2μm in diameter, were milled out in three representative regions, i.e. the compressive edge, the middle section and the tensile edge. Subsequently, the micropillars were compressed at the nominal strain rate of 5×10^{-3} s^{-1} on the Hysitron™ TrioIndenter (TI900) system (Hysitron Inc, Minneapolis, MN) by using a 10-μm flat-ended diamond tip.

4.4 Results and Discussion

To systematically investigate the mechanism of strain softening, the three BMG slices were plastically bent to different curvatures without fracture. Afterwards, the geometries of the bent slices were examined by SEM. Under the SEM, it can be clearly seen that profuse shear banding occurs across the thickness of the bent slice, as shown in Fig 4.2(c). The local mechanical properties were first measured on the Hysitron™ NanoIndenter system (Hysitron Inc, Minneapolis, MN) with a Berkvoich diamond tip. After indentation at the maximum force of 500 mN, the observed indentation mark is around 10 μm in size [inset of Fig 4.3(a)]. To ensure data reproducibility, adjacent indentation marks were set 30μm apart. For the sake of comparison, the indentation force-displacement curves from three typical regions are shown in Fig 4.3(a). Since the standard Oliver-Pharr method is no longer applicable for the indentations made in the regions

close to both edges (Oliver W.C. and Pharr G.M. 1992), the Joslin-Oliver method (J.E. Jakes, C.R. Frihart et al. 2009) was employed here for data analyses.

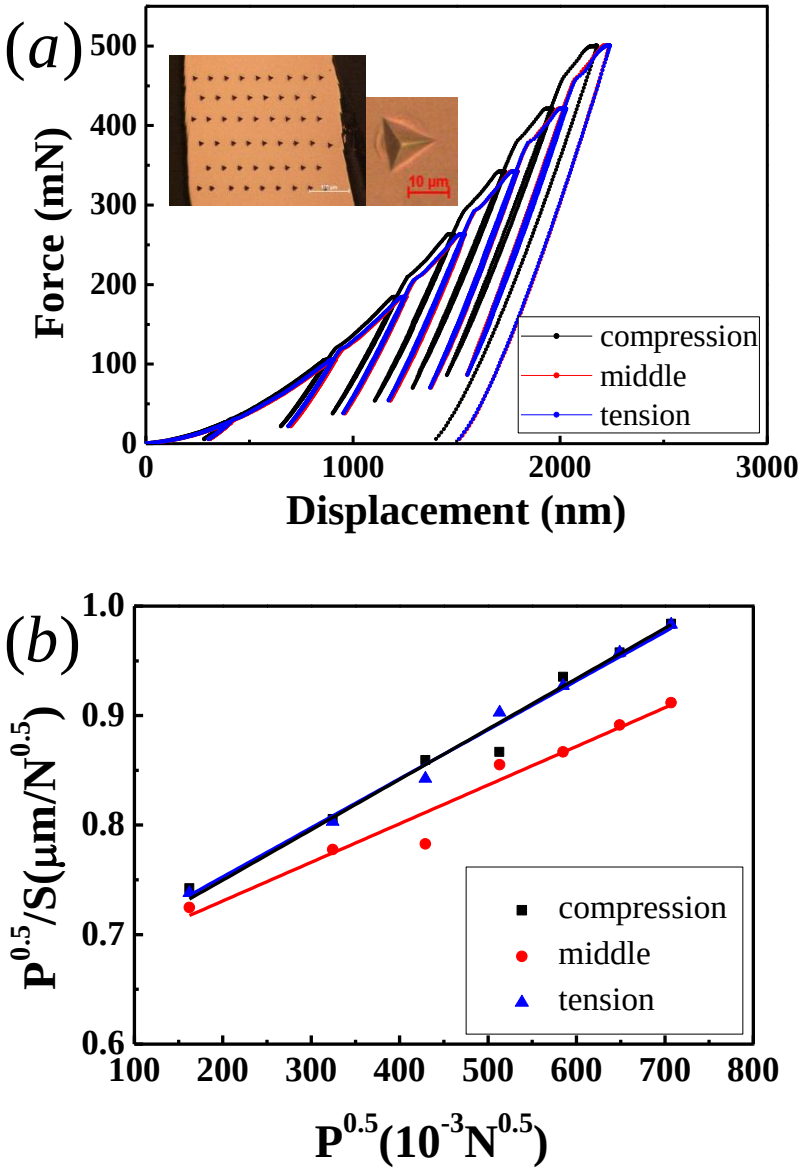

Figure 4.3 (a) The force-displacement curves of the nanoindentation performed in the three typical regions of the BMG bent slice [insets: the optical images of (left) the indentation mark arrays across the thickness of the bent slice and (right) the typical indentation mark with pile-up] and (b) the SYS correlations for multiload indents on compression side, tension side and middle of the bending slice.

Unlike the method of Oliver-Pharr (Oliver W.C. and Pharr G.M. 1992), the most widely used analysis for calculating hardness and modulus of Berkovich nanoindentation, which is based on three implicit assumptions: the sample has rigid support, it fills a half-space and it is homogeneous, the Joslin-Oliver method can remove the artifacts induced by edge effect. Considering the elastic discontinuity, J. E. Jakes et al. (J.E. Jakes, C.R. Frihart et al. 2008; J.E. Jakes, C.R. Frihart et al. 2009) summarized the different types of compliances in a nanoindentation experiment, which are listed in Table 4.1.

Table 4.1 Summary of compliances present in a nanoindentation experiment (J.E. Jakes, C.R. Frihart et al. 2009).

Compliance type	Notation	Descriptions
Total	C_t	Measured unloading compliance, obtained from an experimental load–depth trace
Machine	C_m	Compliance attributable to displacements of nanoindenter load frame Machine-dependent
Structural	C_s	Compliance attributable to edge effects or long range elastic displacements within the specimen, as opposed to the displacements caused by a Sneddon-type stress field Dependent on specimen shape, size, support, and homogeneity
Contact	C_P	Indenter-specimen compliance in the absence of structural compliance; its value can be obtained from Sneddon-type elasticity solution for indentation by a cone or pyramid indenter against a rigid half-space

Note: $C_P = (C_t - C_m - C_s)$

Accounting for the above compliances, the SYS correlation is

$$C_t P_0^{1/2} = (C_m + C_s) P_0^{1/2} + J_0^{1/2} \qquad (4.1)$$

Here, $J_0 = \frac{H}{E_{eff}^2}$ is the Joslin-Oliver parameter (D.L. Joslin and W.C. Oliver 1990) and indicates resistance to plastic penetration. In this case, E_{eff} is an 'effective' modulus for contact and determined by a mathematical formula: $\frac{1}{E_{eff}} = \frac{1}{\beta}\left(\frac{1-\nu_s^2}{E_s} + \frac{1-\nu_d^2}{E_d}\right)$ (note: the subscripts d and s are short for diamond tip and sample, β =1.23 in this chapter), the J_0 and $C_m + C_s$ are independent of load. So, $C_t P_0^{1/2}$ forms a straight line of slop $C_m + C_s$, if it is plotted as a function of $P_0^{1/2}$. Its intercept, $J_0^{1/2}$, is an area-independent material parameter and represents the ratio of square root of hardness and effective modulus. In our experiment, the total compliance, C_t, is calculated by the reciprocal of stiffness, which is the slop of unloading data at maximum load to the displacement axis. As shown in Fig. 4.3(a), a multiload function is defined and its key parameters are listed in Table 4.2.

Table 4.2 The major parameters of multiload function used in our nanoindentation experiment.

Number of cycles	Peak load mN	Displacement exponent	Unloading fraction	Loading time s	Hold time s	Unloading time s
7	500	1	0.8	2	2	2

As shown in Fig. 4.3b, we computed the intercept of the Stone-Yoder-Sproul (SYS) plot, which is the square root of Joslin-Oliver parameter, by fitting SYS plots. Meanwhile, the hardness is calculated based on its definition: the load is divided by its projected area, measured by optical microscopy. After that, the Young's modulus is extracted from Joslin-Oliver parameter getting rid of the artifact caused by this edge effect.

Based on the Joslin-Oliver method (J.E. Jakes, C.R. Frihart et al. 2009) the local hardness and Young's Modulus (the Poisson ratio used for calculating the Young's modulus is 0.365 in this chapter.) of the three BMG bent slices were measured by nanoindentation. As shown by the contour plots in Figs 4.4(a)-(c), the local hardness remains more or less at a constant of ~ 6 GPa for sample 1 and 2 while reduces significantly at the compression side for sample 3. In contrast, there is no significant change in the measured local Young's Moduli. Regardless of the surface plastic strain, their values fluctuate around the average of 110 GPa.

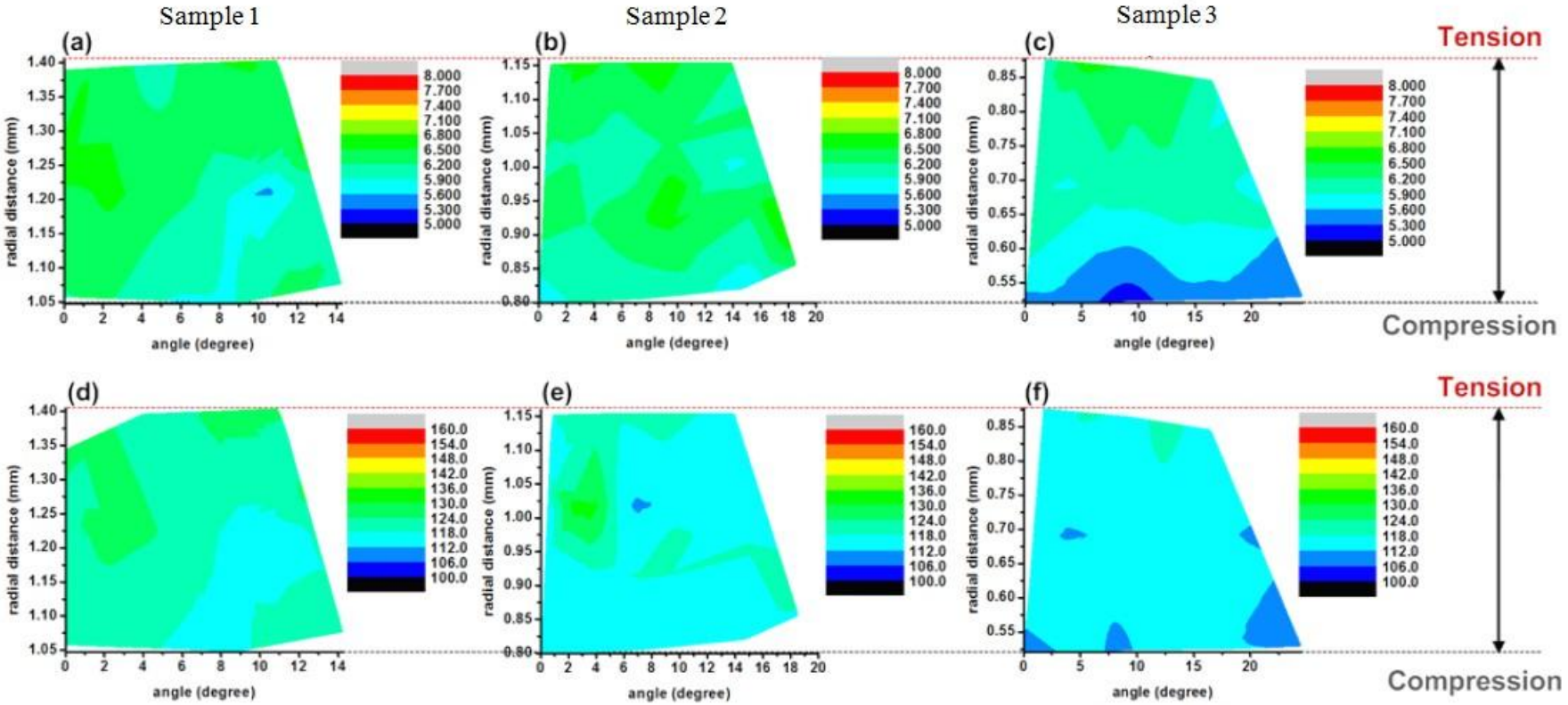

Figure 4.4 The contour plots for (a)-(c) the measured local hardness and (d)-(f) Young's Moduli as a function of the maximum surface plastic strain in a polar coordinate system.

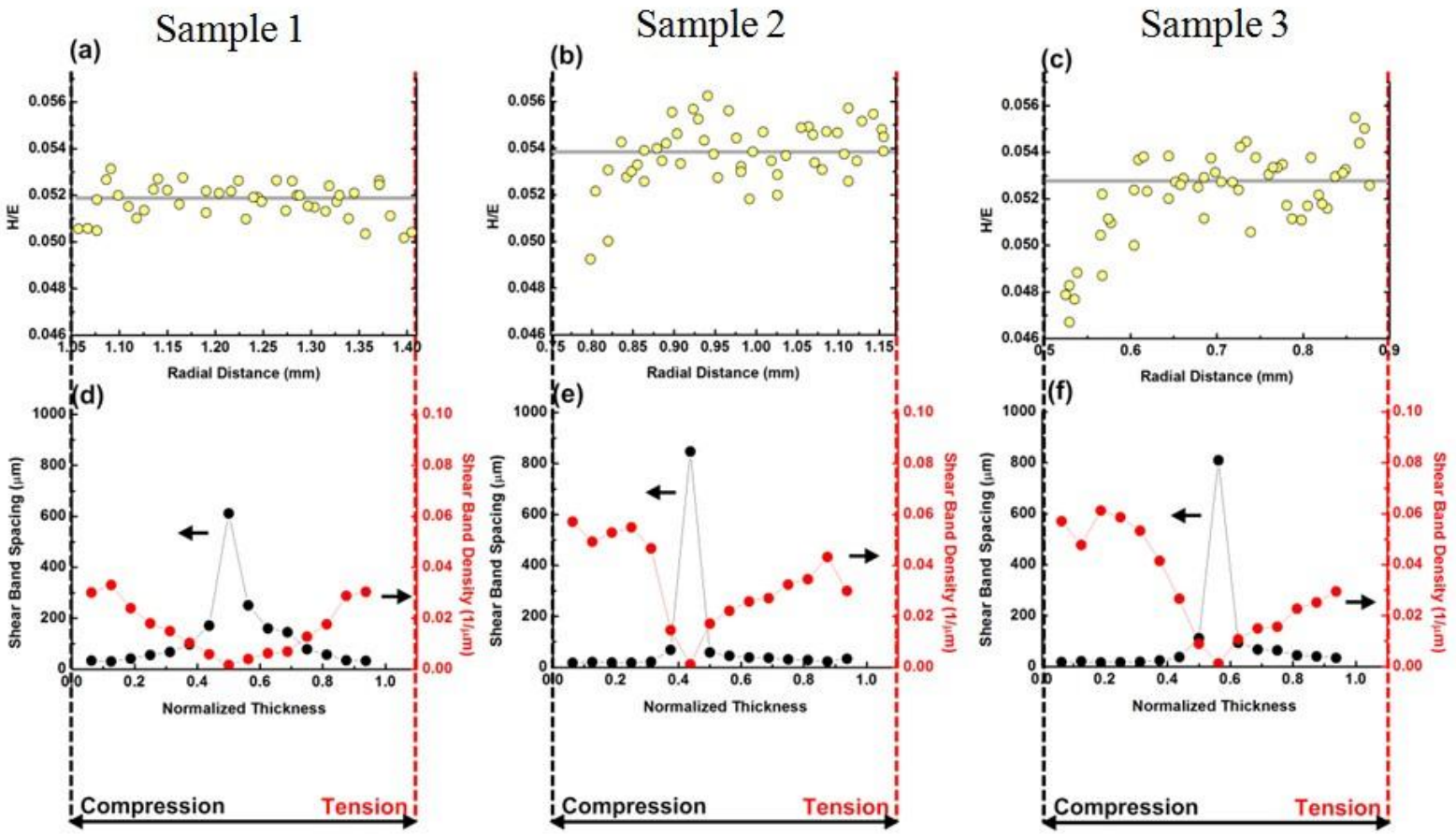

Figure 4.5The variations of (a)-(c) the measured hardness-to-modulus, H/E, ratio and (d)-(f) the shear-band density and spacing in the radial direction corresponding to the different surface plastic strains.

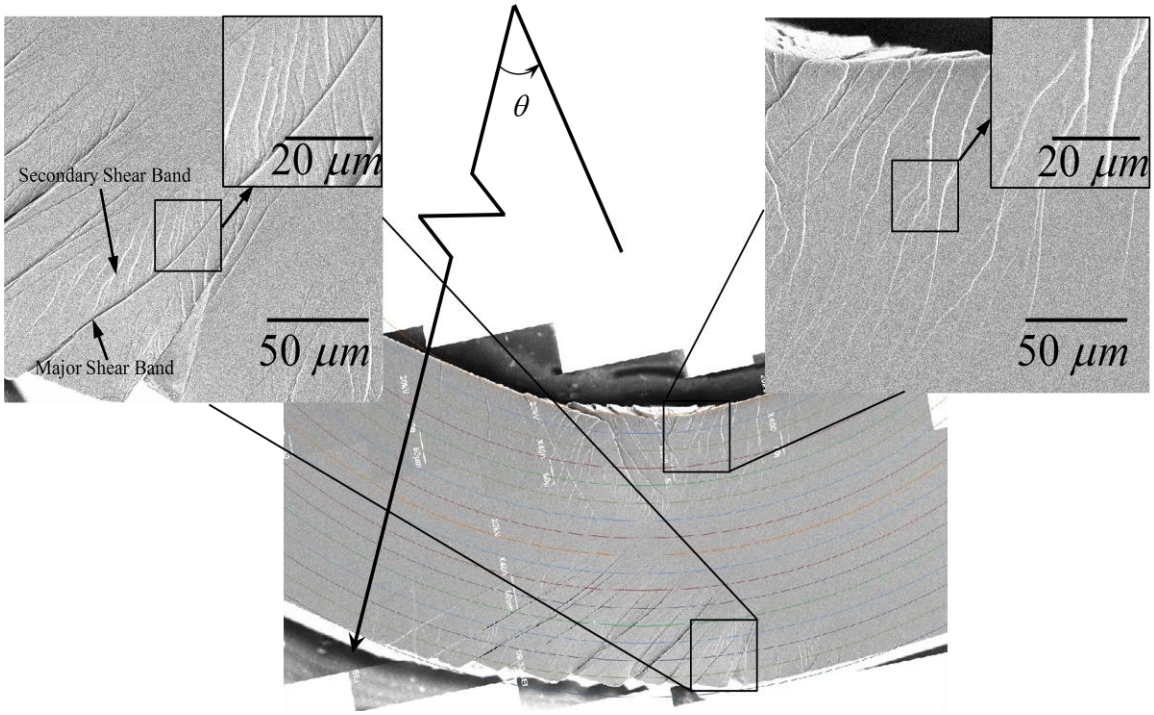

Figure 4.6 The montaged SEM image showing the shear-band morphologies on the BMG bent slice (note that a schematic of the polar coordinate used for locating the indentation marks is superimposed on the SEM image).

To quantificationally justify the factors which cause this change effectively, the shear-band density and spacing were plotted in Fig 4.5 and compared with the ratio of hardness and Young's Modulus across the thickness of the sample. The number of shear bands was carefully counted from the SEM images. The thickness of bent slices is normalized to 1 and the shear bands at fifteen regularly spaced distincts are manually counted, as shown in Fig.4.6. Then, the shear band spacing is calculated by $d_{SB} = \frac{R\theta}{N_{SB}}$, where, R is the radius for the counted shear bands, θ is the polar angle, N_{SB} is the number of shear bands at the corresponding radius. So the shear band density is the reciprocal of the shear band spacing.

Based on the above calculation, the variation of shear bands are shown in Fig 4.5 (d)-(f). On the compression side of bent slices, shear bands density increased from ~0.03 to ~0.06 for the sample 1 to sample 2 and then kept about ~0.06 for the sample 3. But the ratio of hardness and Young's modulus reduced with the increasing of plastic strain. In other words, Fig 4.5 suggests that the shear band density (or spacing) is not the determining factor for the decrease of hardness on the compression side.

Apart from the shear band density (or spacing), we also measured the shear offsets of each shear band on both tension and compression side (shown as Fig. 4.7), and defined the maximum plastic strain with the following equation.

$$\varepsilon = \frac{\sum_{i=1}^{N_{SO}} \triangle s_i \cos\theta}{S} \tag{4.2}$$

Where, $\triangle s_i$ is the length of *i*-th shear offset, N_{SO} is the number of shear offset, θ is tilt angle of shear offset, S is the arc length of neutral axis. If we use the average length of shear offset, the Eq.4.2 can be further simplified. Because N_{SO}/S is equal to the shear offset density (ρ), the simplified plastic strain is $\varepsilon = \overline{\triangle s}\rho\cos\theta$ and $\overline{\triangle s}$ is the average length of shear offset. Based on the above definition, we calculated both the maximum tension and compression plastic strain of three different samples. Then, according to Ye et al.(J. C. Ye, J. P. Chu et al. 2012) , the residual stresses on the compression sides were extracted, and all of them are listed in Table. 4.3.

Table 4.3 The maximum plastic strain on both tension and compression side of the three samples, and residual stress on compression side of all three samples.

	ε_T	ε_C	$\sigma_y\ (Gpa)$	$\sigma_0\ (Gpa)$	$\sigma_r\ (Gpa)$	
					DP model	MC model
Sample 1	0.02	0.02	2.0	2.0	---	---
Sample 2	0.05	0.03	2.1	1.9	0.174	0.156
Sample 3	0.08	0.04	2.2	1.73	0.431	0.385

Note: the subscripts T and C of plastic strain donate tension and compression.

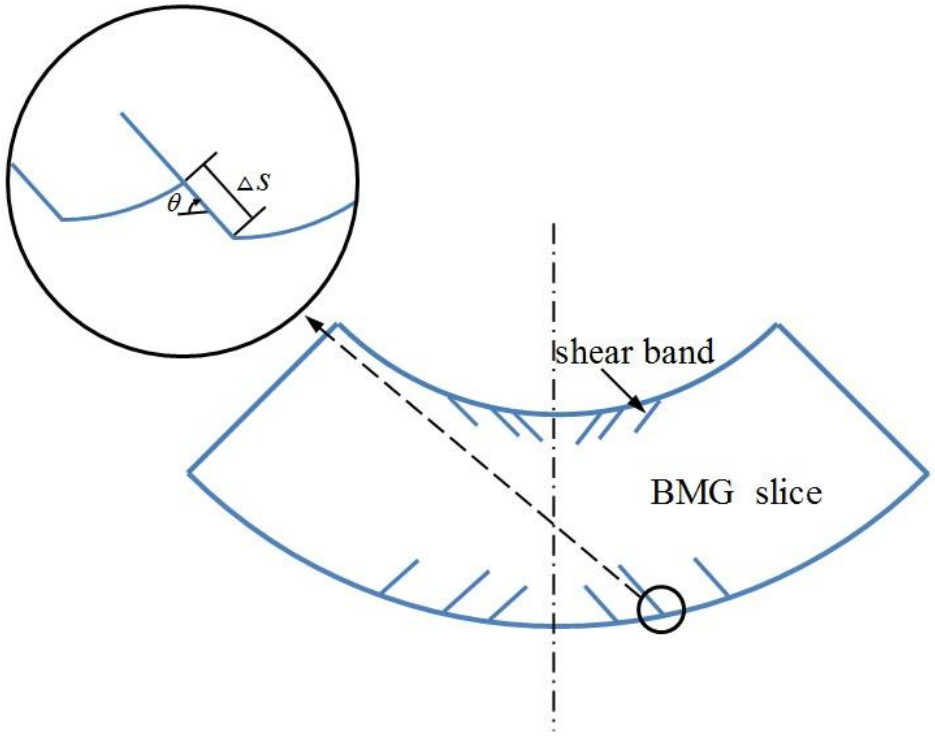

Figure 4. 7 The Schematically drawing for the definition of maximum plastic strain on both tension and compression sides.

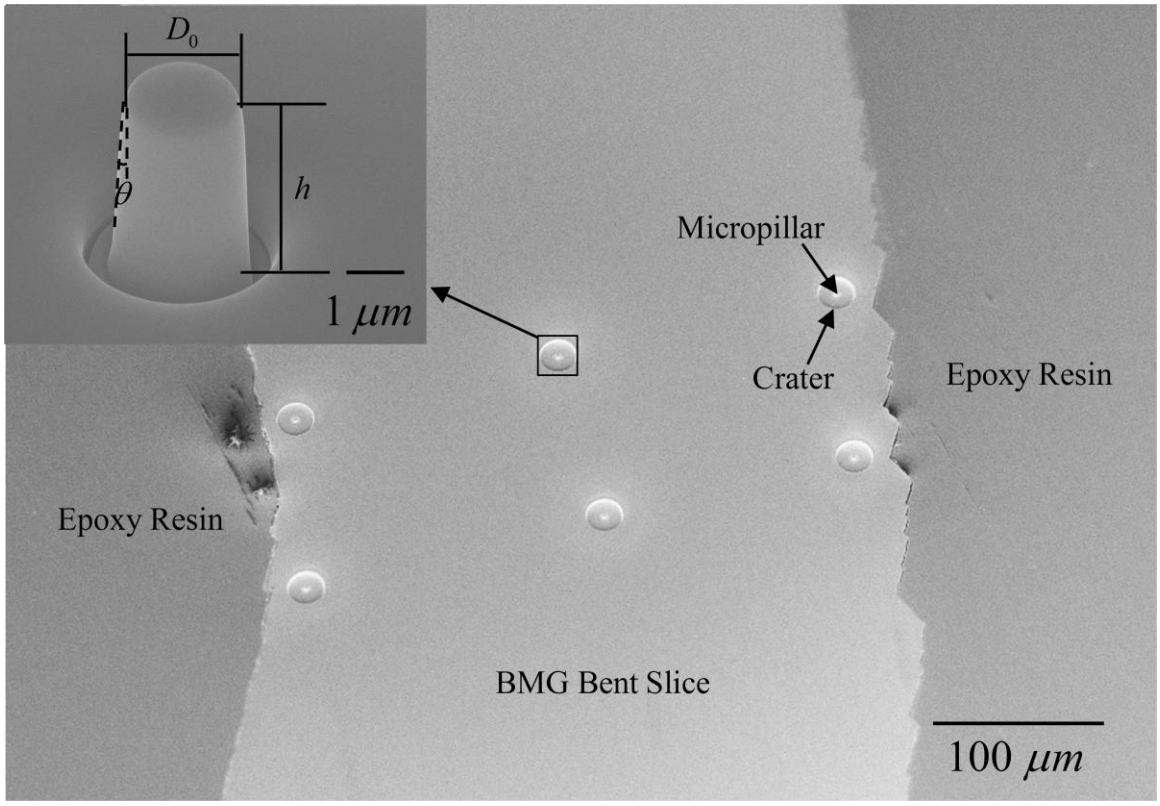

Figure 4.8 The SEM image showing the micropillars fabricated in the thickness direction of the deformed BMG slice (inset: the angle view of a FIB-milled micropillar).

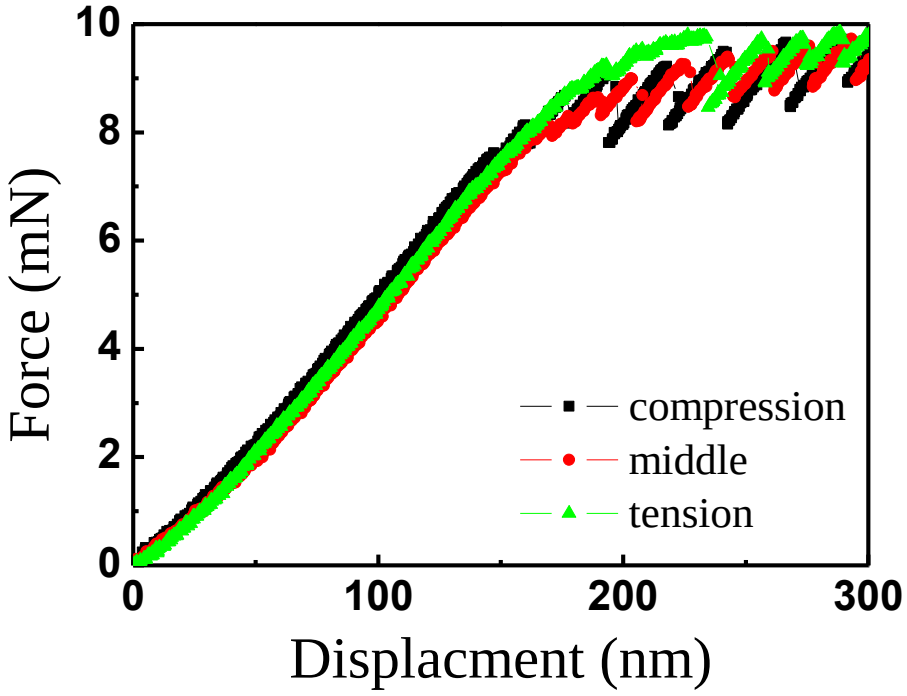

Figure 4.9 The typical serrated load-displacement curves obtained from the microcompression tests conducted at the compression side, the tension side and the middle section.

However, the stress state effect had not been considered in the above analysis. The micro-pillars (shown in Fig. 4.8) were fabricated to measure the yield stress and Young's Modulus under no residual stress state. Three typical force-displacement curves are shown in Fig. 4.9. According to Yang et al. (Y. Yang, J.C. Ye et al. 2009), the Young's modulus can be measured based on the slop at the straight portion of the load-displacement curve and the geometry of the micrpillar. After the correction of their imperfection, they showed that there was no significant change for the hardness and Young's Modulus as shown in Fig. 4.10, which were different from the above nanoindentation results. The comparison between the nanoindentation and micro-pillars compression shown that the residual stress was the main factor causing the decrease of

hardness on the compression region: the hardness and Young's modulus is reduced by the tensile residual stress, but not obviously changed by the compression residual stress.

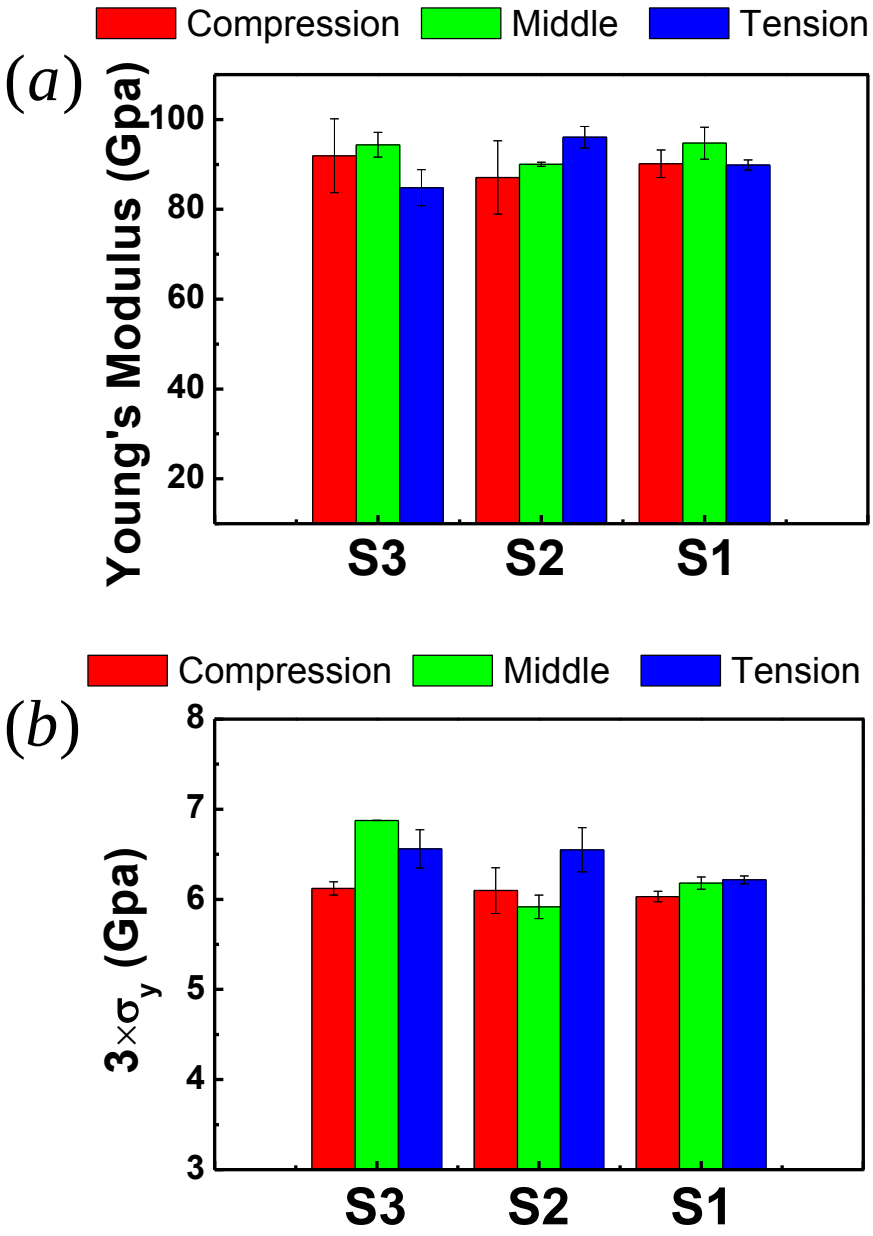

Figure 4.10 Comparison of (a) the measured Young's moduli and (b) three times the yield strengths of the micropillars localized in the tension side, the compression side and middle section at different maximum surface plastic strains.

Distinct from the above conclusions, J. Pan et al. (J. Pan, Q. Chen et al. 2011) probed shear-induced softening and dilatation directly on the shear band itself and found that there were nearly 40% softening measured by nanoindentation on the individual shear band (up to ~160 μm in width). They proved that the increase of free volume was the the mechanism of softening. But the shear band width is ~10nm induced by plastic bending in our experiment which is much smaller than the dimension of indents (~10 μm in length), so the softening induced by shear bands cannot be measured in our experiment. Meanwhile, accompanied by the dilatation and free volume increase, the structure in MG is rejuvenated (or the free volume is annihilated) by structural relaxation. In other word, the balance between the generation and annihilation of free volume determines that no strain-induced softening was captured in our experiment.

At last, nanocrystalline is also a possible cause of softening after plastic deformation. To make sure that if there is nanocrystalline nucleated during the bending, the most severely bent sample was selected to confirm its glass nature. Two TEM samples were fabricated by a dual beam scanning electron microscopy (SEM)/FIB system (Quanta 200 3D, FEI) on both compression and tensile side, from the most severely bent slice. Their TEM and HRTEM results were shown in Fig 4.11 and no nanocrystalline was found.

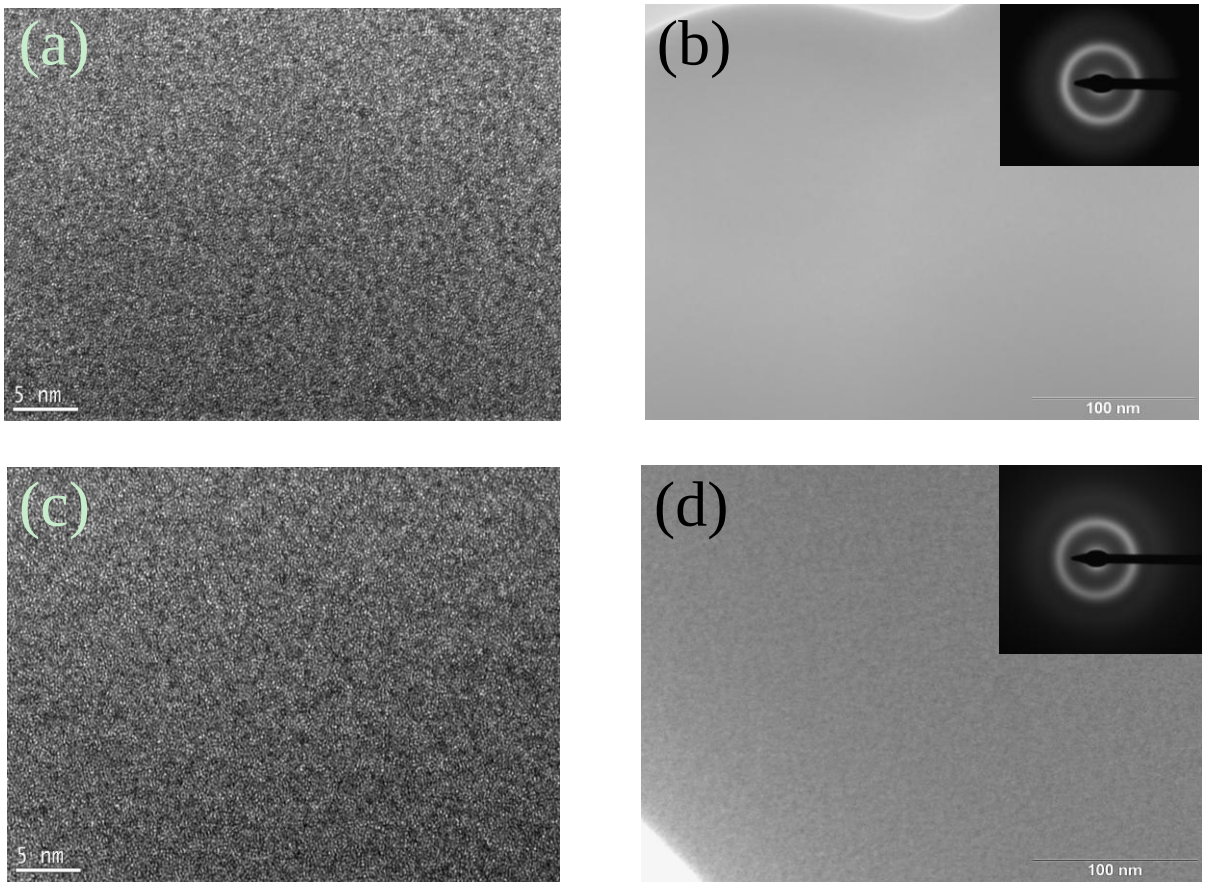

Figure 4.11 The high- and low-resolution TEM images of the severely bent MG slice taken at (a)-(b) the compression side and (c)-(d) the tension side. [insets in (b) and (d): the selective area diffraction patterns (SADPs)].

4.5 Conclusion

In summary, the nanoindentation and micro-pillar compression experiments suggest that the structure may change accompanied by the advancing of shear bands, but without nano-crystalline phase formed. Through the nanoindentation study of the mechanical properties from the compressive to tensile shear-banding zone, it can be shown that the material's elastic modulus keeps at a constant while its hardness drops more significantly in the compression region than that in the tension region. Meanwhile, the shear-band density should not be one important

influence factor, comparing the mechanical properties among different samples. Apart from that, the micro-pillar tests suggest that the residual stresses play a vital role on this asymmetric effect and the TEM images reveal that there is no nanocrystalline phase found in both of tension and compression regions.

In this chapter, the possible factors of strain induced softening in the bent slices are analyzed with respect to the confounding influence of shear-band densities, residual stresses and possible structural variation arising from the change in the stress state. Under tensile state, the shear bands are the connection of free-volume or voids and the atomic clusters are not damaged. But for the compression state, some atomic clusters must be broken and the material is softening. In a word, all these structural changes are still in the micro scale and cannot change the micromechanical material properties numerically.

4.6 References

A. Inoue, H. Yamaguchi, Y. Zhang and T. Masumoto, (1990). "Al-La-Cu Amorphous-alloys with A Wide Supercooled Liquid Region." Materials Transactions JIM **31**(2): 6.

A.A. Salem, S. R. Kalidindi and S.L. Semiatin, (2005). "Strain hardening due to deformation twinning in α-titanium: Constitutive relations and crystal-plasticity modeling." acta Materialia **53**(12): 8.

Abhijit P. Brahme, Kaan Inal., Raja K. Mishra and Shigeo Saimoto, (2011). "A new strain hardening model for rate-dependent crystal plasticity." Computational Materials Science **50**(10): 11.

Alain Reza Yavari, Alain Le Moulec, Akihisa Inoue, Nobuyuki Nishiyama, Nicoleta Lupu, Eiichiro Matsubara, Walter José Botta, Gavin Vaughan, Marco Di Michiel and Åke Kvick, (2005). "Excess free volume in metallic glasses measured by X-ray diffraction." Acta Mater. **53**(6): 9.

Biraja P. Kanungo, Stephen C. Glade, Palakkal Asoka-Kumar and Katharine M. Flores, (2004). "Characterization of free volume changes associated with shear band formation in Zr- and Cu-based bulk metallic glasses." Intermetallics **12**(10-11): 8.

Byung-Gil Yoo, Kyoung-Won Park, Jae-Chul Lee, U. Ramamurty and Jae-il Jang, (2009). "Role of free volume in strain softening of as-cast and annealed bulk metallic glass." J. Mater. Res. **24**(4): 12.

C. A. Schuh, T. C. Hufnagel and U. Ramamurty (2007). "Mechanical Behavior of Amorphous Alloys." Acta Mater. **55**: 43.

D. Pan, H. W. Liu, T. Fujita, A. Hirata, A. Inoue, T. Sakurai and M. W. Chen, (2010). "Deformation-induced change in the structure of metallic glasses during multistep indentation." Phys. Rev. B **81**(13): 4.

D.L. Joslin and W. C. Oliver (1990). "New method for analyzing data from continuous depth-sensing microindentation tests " Journal of Materials Research **5**(01): 4.

G.Y. Wang, P. K. Liaw, Y. Yokoyama and A. Inoue, (2012). "Evolution of shear bands and fatigue striations in a bulk metallic glass during fatigue." Intermetallics **23**: 5.

G.Y.Wang, P. K. Liaw, Y. Yokoyama, A. Inoue and C.T. Liu, (2008). "Fatigue behavior of Zr-based bulk-metallic glasses." Materials Science and Engineering A **494**: 10.

H. Bei, S. Xie and E. P. George, (2006). "Softening Caused by Profuse Shear Banding in a Bulk Metallic Glass." Phys. Rev. Lett. **96**: 4.

J. C. Ye, J. P. Chu, Y. C. Chen, Q. Wang and Y. Yang (2012). "Hardness, yield strength, and plastic flow in thin film metallic-glass." Journal of Applied Physics **112**: 9.

J. Pan, Q. Chen, L. Liu and Y. Li, (2011). "Softening and dilation in a single shear band." Acta Materialia **59**(13): 13.

J.E. Jakes, C. R. Frihart, J.F. Beecher, R.J. Moon and D.S. Stone, (2008). "Experimental method to account for structural compliance in nanoindentation measurements." Journal of Materials Research **23**(04): 15.

J.E. Jakes, C. R. Frihart, J.F. Beecher, R.J. Moon, P.J. Resto, Z.H. Melgarejo, O.M. Sua ŕez, H. Baumgart, A.A. Elmustafa and D.S. Stone (2009). "Nanoindentation near the edge." J. Mater. Res. **24**(3): 16.

Jing Li, F. Spaepen and T. C. Hufnagel, (2002). "Nanometer-scale defects in shear bands in a metallic glass." Philosophical Magazine A **82**(13): 8.

Jinn P. Chu, J. E. Greene, Jason S.C. Jang, J.C. Huang, Yu-Lin Shen, Peter K. Liaw, Yoshihiko Yokoyama, Akihisa Inoue and T.G. Nieh, (2012). "Bendable bulk metallic glass: Effects of a thin, adhesive, strong, and ductile coating." Acta Materialia **60**: 13.

Johnson W. L. (2002). "Bulk Amorphous Metal - An Emerging Engineering Material." JOM **54**(3): 4.

Kou Hongchao, Wang Jun, Ma Weifeng, Chang Hui, Li Jinshan and Zhou Lian, (2011). "Correlations between Shear Bands and Plasticity in Ti-Based Bulk Metallic Glass." Rare Metal Materials and Engineering **40**(3): 4.

L. Wang, H. B., Y.F. Gao, Z.P. Lu and T.G. Nieh (2011). "Effect of residual stresses on the hardness of bulk metallic glasses." Acta Materialia **59**: 7.

L.Y. Chen, Q. Ge, S. Qu and J.Z. Jiang, (2008). "Stress induced softening and hardening in a bulk metallic glass." Scripta Materialia **59**(11): 4.

M. H. Cohen and D. Turnbull (1959). "Molecular transport in liquids and glasses." J. Chem. Phys. **31**: 6.

M. Song, Y. Y. Sun, Y. H. He and S. F. Guo (2012). "Structure related hardness and elastic modulus of bulk metallic glass." JOURNAL OF APPLIED PHYSICS **111**: 5.

M.Q. Jiang and L. H. Dai (2009). "On the origin of shear banding instability in metallic glasses." Journal of the Mechanics and Physics of Solids **57**(8): 26.

Min Ha Lee, J. H. J., Jürgen Eckert, (2010). "Effect of Residual Stress on Mechanical Property of Monolithic Bulk Metallic Glass." Materials Science Forum **654 - 656**: 4.

Mingwei Chen (2008). "Mechanical Behavior of Metallic Glasses: Microscopic Understanding of Strength and Ductility." Annual Review of Materials Research **38**: 25.

Mingwei Chen, Akihisa Inoue, Wei Zhang and Toshio Sakurai, (2006). "Extraordinary Plasticity of Ductile Bulk Metallic Glasses." Phys. Rev. Lett. **96**(24): 4.

N. Schwarzer, I. Hermann, T. Chudoba and F. Richter, (2001). "Contact modelling in the vicinity of an edge." Surface and Coatings Technology **146-147**: 7.

Nozomu Togashi, Mamoru Ishida, Nobuyuki Nishiyama and Akihisa Inoue, (2008). "Wear Resistance of Metallic Glass Bearings." Rev. Adv. Mater. Sci. **18**: 5.

Oliver W.C. and Pharr G. M. (1992). "An improved technique for determining hardness and elastic modulus using load and sensing indentation experiments." Journal of Materials Research **7**(6): 19.

P. Yu, K. C. Chan, W. Chen and L. Xia, (2011). "Elastic moduli and mechanical properties of bulk metallic glasses after quasi-static compression." Journal of Alloys and Compounds **509**: 4.

P.S. Steif, F. Spaepen and J.W. Hutchinson, (1982). "Strain localization in amorphous metals." Acta Metallurgica **30**(2): 9.

R. Busch, W. Liu and W. L. Johnson, (1998). "Thermodynamics and kinetics of the Mg65Cu25Y10 bulk metallic glass forming liquid." Journal of Applied Physics **83**(8): 8.

S.Q. Shu, Y. Yang, T. Fu, C.S. Wen and J. Lu, (2009). "Can Young's modulus and hardness of wire structural materials be measured using nanoindentation." J. Mater. Res. **24**(3): 5.

T.C. Chieh, J. Chu, C.T. Liu and J.K. Wu, (2003). "Corrosion of $Zr_{52.5}Cu_{17.9}Ni_{14.6}Al_{10}Ti_5$ bulk metallic glasses in aqueous solutions." Materials Letters **57**: 4.

Wei Hua Wang, Hai Yang Bai, J. L. Luo, Ru Ju Wang and D. Jin, (2000). "Supersoftening of transverse phonons in $Zr_{41}Ti_{14}Cu_{12.5}Ni_{10}Be_{22.5}$ bulk metallic glass." Physical Review B **62**(1): 4.

Y. Waseda and K. T. Aust (1981). "Corrosion behaviour of metallic glasses " Journal of Materials Science **16**(9): 23.

Y. Yang, J. C. Ye, J. Lua, F.X. Liu and P.K. Liaw, (2009). "Effects of specimen geometry and base material on the mechanical behavior of focused-ion-beam-fabricated metallic-glass micropillars." Acta Materialia **57**: 11.

Y. Zhao and T. C. Ovaert (2010). "Error Estimation of Nanoindentation Mechanical Properties Near a Dissimilar Interface via Finite Element Analysis and Analytical Solution Methods." J Mater. Res. **25**(12): 9.

Ye JC, Lu J, Yang Y and Liaw PK (2010). "Extraction of bulk metallic-glass yield strengths using tapered micropillars in micro-compression experiments " Intermetallics **18**(3): 9.

Yunfeng Shi and Michael L. Falk (2005). "Structural transformation and localization during simulated nanoindentation of a noncrystalline metal film." Appl. Phys. Lett. **86**: 4.

5. Fractal Growth of the Dense-Packing Phase in Annealed Metallic Glass imaged by High-Resolution Atomic Force Microscopy

Unlike crystalline metals, which have a well-understood periodically structure, the amorphous structure of metallic glasses (MGs) is still poorly understood, particularly when such a structure rearranges itself at the nanoscale under external agitations. In this chapter, we provide compelling evidence obtained from a recently developed high-resolution atomic force microscopy (HRAFM) technique that reveals the nanoscale structural heterogeneity after thermal annealing in a Zr-Ni metallic glass. Through the HRAFM technique, we are able to uncover the annealing-induced fractal growth of the dense-packing phases in the binary MG thin film, which exhibits a fractal dimension of ~1.7, in line with a two-dimensional diffusion limited aggregation process. The current findings not only reveal the evolution process of atomic packing in the annealed MG thin film, but also shed light on the possible cooling rate effect on the atomic structure of MGs.

5.1 Introduction

One of the biggest challenges facing us in the field of metallic glasses (MGs) is to discover how their atomic structure is constructed and how such a construction can be built into the structure-property relation – a problem that has long been pursued in this kind of material. Unlike crystalline metals, whose periodically ordered structure is energetically stable and can be imaged well using state-of- art electron microscopy, MGs possess an apparently disordered structure that

is metastable in nature and usually shows only a maze-like pattern under an electron microscope, thus frustrating any meaningful tracking of its underlying structural features. In the past, tremendous research efforts have been devoted to revealing the short- and medium-range order in MGs(D.B. Miracle 2004; Cang Fan, P. K. Liaw et al. 2006; H. W. Sheng, W. K. L UO et al. 2006; D. Ma, A.D. Stoica et al. 2009; Akihiko Hirata, Pengfei Guan et al. 2010), which originate from the clustering of dense-packing atoms and can be revealed by static means, such as x-ray or neutron diffraction (Cang Fan, P. K. Liaw et al. 2006; D. Ma, A.D. Stoica et al. 2009; W. Dmowski, T. Iwashita et al. 2010) and high-resolution transmission electron microscopy (TEM) (Akihiko Hirata, Pengfei Guan et al. 2010). Despite the great success achieved so far in understanding these local ordered structures, questions still remain as how the mechanical/physical properties of MGs are derived from the overall structural amorphousness, since these properties in principle rely on not only the local "ordered" structures, but also "disordered" and "semi-ordered" ones (Y.Q. Cheng and E. Ma 2011). Unfortunately, these non-ordered structures possess no unique structural features and become indistinguishable when only examined statically. In addition, what keeps the problem complicated is that the whole amorphous structure of an MG alloy can rearrange itself when perturbed externally, leading to either structural relaxation or rejuvenation. These features of the amorphous structure are tied to many important dynamic processes, such as aging, plasticity and glass transition, and yet to be understood for MGs.

In principle, the whole atomic structure of an MG may be envisaged as an atomic-scale composite, consisting of solid-like regions as a "matrix" containing liquid-like regions as "inclusions" (Cang Fan, P. K. Liaw et al. 2006; J. C. Ye, C. T. Liu et al. 2010; Y. Yang, J. F.

Zeng et al. 2010; Y.H. Liu, D. Wang et al. 2011; Y.Q. Cheng and E. Ma 2011; Yang Y and Liu C.T. 2012). Albeit simple, this kind of physical picture agrees qualitatively with the results obtained from recent atomic force microscopy (AFM) experiments (Y.H. Liu, D. Wang et al. 2011). Inspired by this, one may wonder if the evolution process of the amorphous structure in MGs can be also revealed. If so, we could take a big stride in the pursuit of understanding the structure-property relation in MGs. With this in mind, we set the primary goal for the current study to be tracking the evolution process of the atomic structure in an MG annealed to various degrees. The major reason for selecting thermal annealing as the way of perturbation is that, through this process, we can readily obtain numerous glassy structures that have the same chemical composition but different energetic states. In so doing, we may be able to discover those structural features that are common to the same metallic glass under a variety of cooling rates.

5.2 Material and Experiment

To achieve our goal, an MG thin film is used as the model material, which has the simple binary composition of $Zr_{70}Ni_{30}$ (in atomic percentage) and a thickness of ~300 nm. The thin film was deposited from a Zr-Ni target by means of reactive DC magnetron sputtering using an Alliance Concept AC450 device. The substrate was silicon (100), positioned at a distance of 70 mm from the target. The vacuum limit was 5×10^{-7} mbar and the argon working pressure was 3×10^{-3} mbar. The delivery power for deposition was 300 W. The atomic structure of the thin film was characterized by X-ray diffraction and TEM. As shown in Fig.5.1, both experiments confirm the structural amorphousness of the thin film. Next, we performed AFM scanning of the thin film on a Vecco™ multimode AFM platform in an ambient environment. To achieve ultrahigh spatial

resolution, a special AFM tip was used in the study, which possesses a spring constant k of ~40 N m^{-1} and a damping factor Q of ~ 700, and has its tip coated with a diamond-like carbon (DLC) nanotube with a radius of ~1 nm. During the AFM scanning, the amplitude-modulation (AM) mode was employed under a proportional-integral feedback control, and the AFM tip making intermittent contacts with the film surface at a pre-defined set-point amplitude A_{sp} and a frequency f. The basic mechanics of using AM-AFM for structural characterization has been detailed elsewhere (J. P. Cleveland, B. Anczykowski et al. 1998; P. J. James, M. Antognozzi et al. 2001; Garcia R and Perez R. 2002) and is briefly described below for MGs. At the set-point amplitude A_{sp}, the mechanical energy is transported from the AFM tip and dissipated away on the surface of an MG. Based on prior findings (J. C. Ye, C. T. Liu et al. 2010; Y.H. Liu, D. Wang et al. 2011), it is known that the dense-packing (solid-like) phases in an MG tend to dissipate less energy than the loose-packing (liquid-like) ones. Consequently, by measuring the energy dissipation point by point on the film surface, a structural contrast, including both ordered (dense-packing) and non-ordered (loose-packing) structural features, can form on a two-dimensional (2-D) plane (Y.H. Liu, D. Wang et al. 2011).

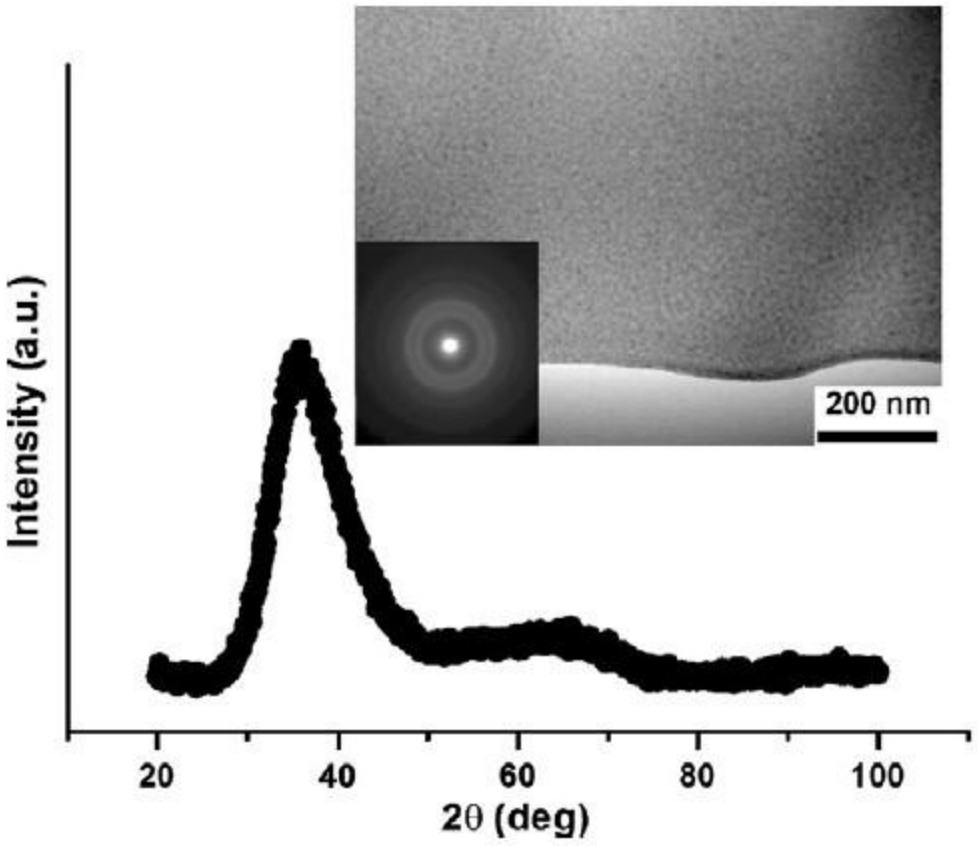

Figure 5.1 The X-ray diffraction pattern of the thin film with a broad peak at $2\theta \sim 40^\circ$ indicative of an overall amorphous structure (the inset: the TEM plan-view of the freestanding film obtained by etching away the silicon substrate and subsequent ionic polishing at 3 kV with liquid nitrogen cooling).

In practice, however, it is not straightforward to achieve a nano-scale resolution with the AM-AFM method. Great care must be taken in preparing a film surface with a sub-nanometer-scale roughness, and in removing artifacts due to surface adhesion and topography from the derived structural image (J. P. Cleveland, B. Anczykowski et al. 1998; P. J. James, M. Antognozzi et al. 2001; Garcia R and Perez R. 2002). For brevity, the details of obtaining a high-resolution AFM structural image is omitted here; instead, they are presented in **Appendix A**. In our AM-AFM experiments, the two direct measurements are the surface topography and phase

images. In Figs.5.2 (a)-(f), one can see a series of surface topography images (left column) and the corresponding phase images (right column), which were obtained from a same area on the film but apparently change their 'morphology' systematically with the A_{sp}/A_0 ratio, where A_0 is the vibration amplitude of the tip before it 'taps' the film surface. As shown in Figs.5.2 (a)-(c), the measured surface roughness decreases from ~0.8 nm at $A_{sp}/A_0 = 0.92$ to ~0.7 nm at $A_{sp}/A_0 = 0.15$; in contrast, the measured phase shifts increase with the decreasing A_{sp}/A_0 ratio. According to the work of Garcia R. and Perez R. (Garcia R and Perez R. 2002), the A_{sp}/A_0 ratio correlates positively with the tip-surface distance, and the sign of the measured phase shift indicates the nature of the tip-surface interaction, i.e., a positive phase shift corresponds to repulsion and a negative phase shift to attraction. To check if the same sign convention is followed by our system, we measured the phase shift, $\Delta\varphi$, as a function of the A_{sp}/A_0 ratio by probing the individual spots on the film. As shown in Fig.5.3, negative phase shifts are obtained at a relative high A_{sp}/A_0 ratio ($0.7 < A_{sp}/A_0 < 1.0$) as opposed to positive phase shifts at a relatively low A_{sp}/A_0 ratio ($A_{sp}/A_0 < 0.7$), indicating that the same sign convention as used by Garcia R. and Perez R.(Garcia R and Perez R. 2002) was adopted by our AFM system. Since the formation of the structural contrast is due to a repulsive tip-surface interaction, a relatively low A_{sp}/A_0 ratio was utilized in our AFM experiments.

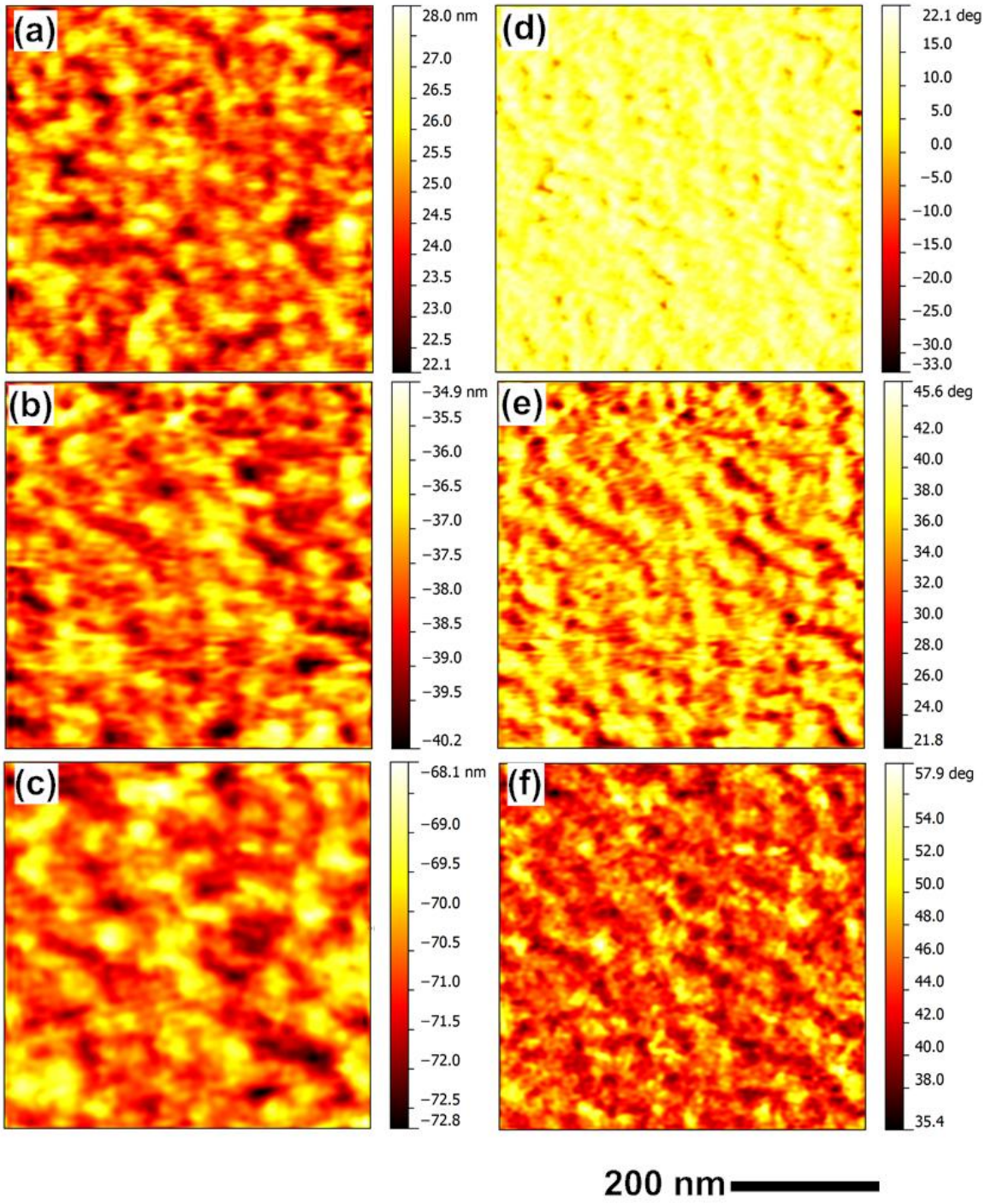

Figure 5.2 The effect of the A_{sp} / A_0 ratio, as correlated with the mean distance between the vibrating AFM tip and film surface, is on the obtained AFM images. (a) to (c) the topography and (d) to (f) corresponding phase images obtained respectively at $A_{sp} / A_0 = 0.92$ [(a) and (d)], 0.62 [(b) and (e)], and 0.15 [(c) and (f)]. The scale bar for all images is 200 nm. The effect of surface roughness has been corrected from the phase images.

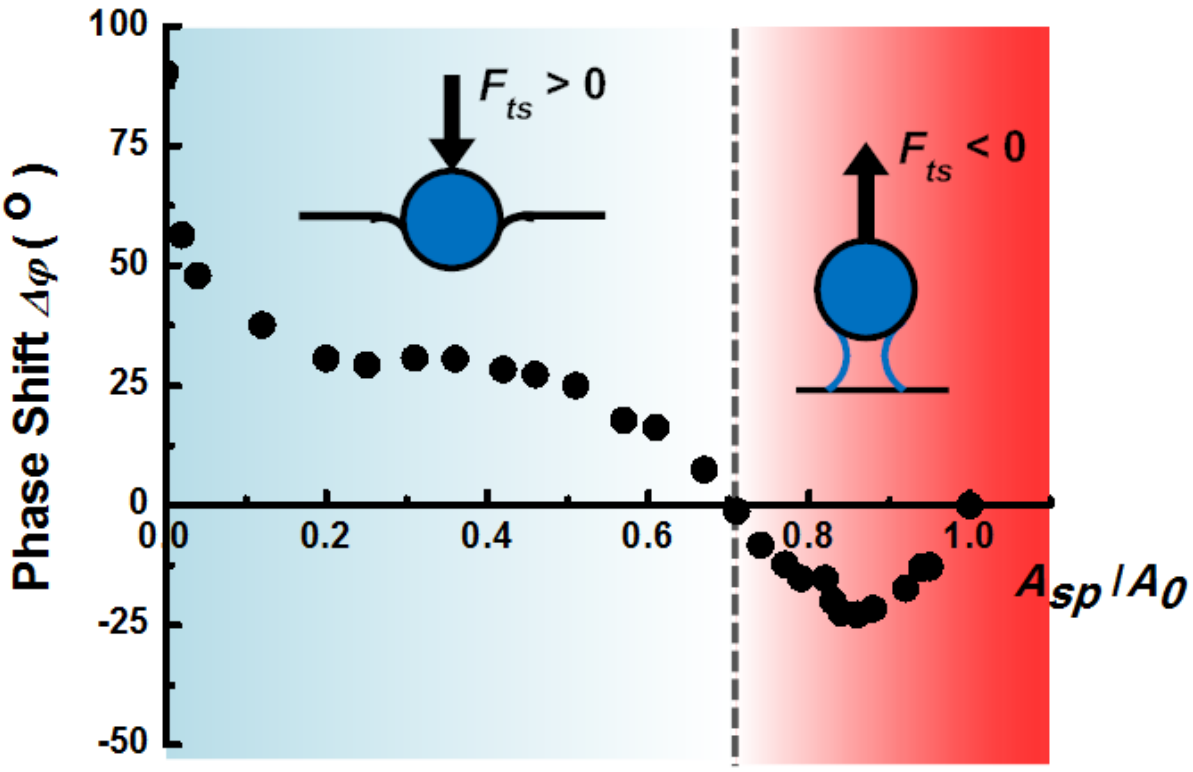

Figure 5.3 The variation of phase shift $\Delta\varphi$ with A_{sp}/A_0 measured at a spot of the film. Insets: Sketches of the negative (pulling) and positive (pushing) tip-surface forces.

5.3 Results and Discussion

We focus here only on the AFM images obtained at $A_{sp}/A_0 = 0.15$, although those obtained at others ratios may be similar. Note that, in our AFM experiments, the driving frequency *f* of the tip is fixed at its resonance frequency; therefore, the measured phase shift, $\Delta\varphi$, can be related to the local energy dissipation, E_{dis}, via the simple relation, $E_{dis}/\left(\pi k A_{sp} A_0 / Q\right) = sin\left(\pi/2 - \Delta\varphi\right) - A_{sp}/A_0$ (J. P. Cleveland, B. Anczykowski et al. 1998; P. J.

James, M. Antognozzi et al. 2001; Garcia R and Perez R. 2002) and the time-averaged tip-surface force, F_{ts} , which is exerted by the AFM tip under the AM mode, can be written as $F_{ts} = F_0 \cos\left(\pi/2 - \Delta\varphi\right)/2$, where $F_0 = kA_0/Q$ (Nicol´as F Mart´ınez and Ricardo Garc´ıa 2006). In that regard, we can measure not only the energy dissipation but also the average tip-surface force through the AFM phase imaging. For our AFM experiments, the estimated repulsive force, F_{ts} , falls in the range between ~0.1 and ~0.2 nN, with $A_0 \sim 10$ nm and $20° < \Delta\varphi < 60°$, which also corresponds to an dissipated energy varying between ~6 and ~13 eV over the tip-surface contact area [Figs.5.2 (d)-(f)]. Assuming a contact radius of ~ 1 nm, which equals the lateral size of the coated DLC nanotube, we can obtain an average contact pressure of ~31 to ~77 MPa being exerted by the tip, which is far below the average hardness of ~ 3 GPa for Zr-based metallic glasses. Thus, it is important to note that the surface material was deformed only in an elastic fashion.

Without affecting the image contrast, the normalized energy dissipation, $E_{dis}/\left(\pi k A_{sp} A_0/Q\right)$, is used to construct the structural image. As shown in Fig.5.4 (a), a blue-red color palette is used for image rendering to further enhance the visual contrast. The loose-packing phases are those associated with high energy dissipation, and colored in red; the dense-packing phases are those associated with low energy dissipation, and are colored in blue. Interestingly, both the loose- and dense-packing phases appear as isolated “islands” [Fig.5.4 (a)], and the majority of the scanning area appears to be colored green, which corresponds to “semi-ordered” structures with intermediate atomic-packing. Note that the color scale is set somewhat arbitrarily, and the image contrast derived thereof yields only qualitative information on the general structure of the thin film.

As the elastic coupling among different phases obscures clear-cut inter-phase boundaries, we need to set a boundary-defining criterion to perform a quantitative analysis. Note that a similar situation is encountered in the development of the atomic stress theory for MGs (T. Egami 2011), in which the so-called "free volume" and "anti-free-volume" are defined based on a particular atomic-level volume strain that can be related to the topological instability of atomic clusters. Following a similar logic, here we define the loose-packing phases as the region taking the top P_c percents of the total energy dissipation. Here, P_c refers to the area under the curve of the energy dissipation distribution, as shown in Fig.5.4 (b). Conceptually, this is equivalent to selecting a cut-off energy that is dissipated at the boundary of a loose-packing phase.

Before the annealing experiment, we were interested in seeing how the loose-packing phases so defined are compared with the shear transformation zones (STZs) (A.S. Argon 1979). In Argon's seminal work (A.S. Argon 1979), STZs were speculated to be loosely packed regions prone to irreversible shear deformation upon yielding. This speculation has two important implications. First, the STZs are areas of a transient effect that may be understood as a "dynamic defect"; and second, the STZs may have s static structural feature closely related to the regions of low packing density. In other words, the loose-packing regions would be the preferential STZ sites according to the original STZ theory. In the MG literature, confirming whether such a correlation exists between the dynamic STZ effect and the corresponding static structural feature has been the subject of several studies (D. Pan, A. Inoue et al. 2008; Y.H. Liu, D. Wang et al. 2011; Y.Q. Cheng and E. Ma 2011).Through atomistic simulations (Y.Q. Cheng and E. Ma 2011), however, it has been found that, on a statistical basis, STZ sites may be correlated with

loose-packing phases, which corroborates the notion of Argon to a certain degree. In view of this, the comparison of our experimental results with the known features of STZs is meaningful.

Figures 5.4 (c)-(g) displays the results obtained at P_c = 5%. First of all, the loose-packing phases are isolated from each other, as shown by the inset (right) of Fig.5.4 (b). Second, their inclination angle$\emptyset$, as defined by the inset (left) of Fig.5.4 (b), has a uniform distribution in [-180 °, 180 °], indicative of the random orientation of the loose-packing phases [Fig. 5.4 (c)]. Third, by comparing the maximum (D_{max}) and minimum (D_{min}) bounding lengths of the loose-packing phases [Fig. 5.4 (d) and (e)], we find that their shape is close to an ellipse, showing an aspect ratio close to 2. This ratio agrees very well with what was observed from the atomistic simulations (Qi-Kai Li and Mo Li 2007), in which similar shape anisotropy, with an aspect ratio of 1.5-2.0, was found for shear-intensified regions in the MG. Note that similar shape anisotropy has also been observed in AFM images obtained at other A_{sp}/A_0 ratios [Fig. 5.4 (f)].

We can estimate the average size of these loose-packing phases by assuming that they take on a circular shape. In doing so, we obtain an average radius of ~2 nm [Fig. 5.4 (g)], which, in order of magnitude, is also consistent with both the theoretical estimation (William L. Johnson, Marios D. Demetriou et al. 2007) and experimental measurement (D. Pan, A. Inoue et al. 2008) of the average size for STZs (~2 nm). Note that similar findings could be obtained if P_c was varied between ~2% and ~15%. Within this range, the loose-packing phases exhibit an average size varying between ~1 nm and ~4 nm, but still retain their shape anisotropy and random orientation. With a P_c below ~2%, however, we could not obtain sufficient data for analyses,

while above ~15% the loose-packing phases start to merge into the background of the structural image and, therefore, lose their physical meaning. Based on these findings, it can be generally seen that the loose-packing phases revealed by our AFM experiments possess similar geometric features to those already known for STZ sites, which is consistent with previous findings obtained from the atomistic simulations (Qi-Kai Li and Mo Li 2007; Y.Q. Cheng and E. Ma 2011). Subsequently, it was our task to explore the evolution of atomic packing in an annealed MG thin film.

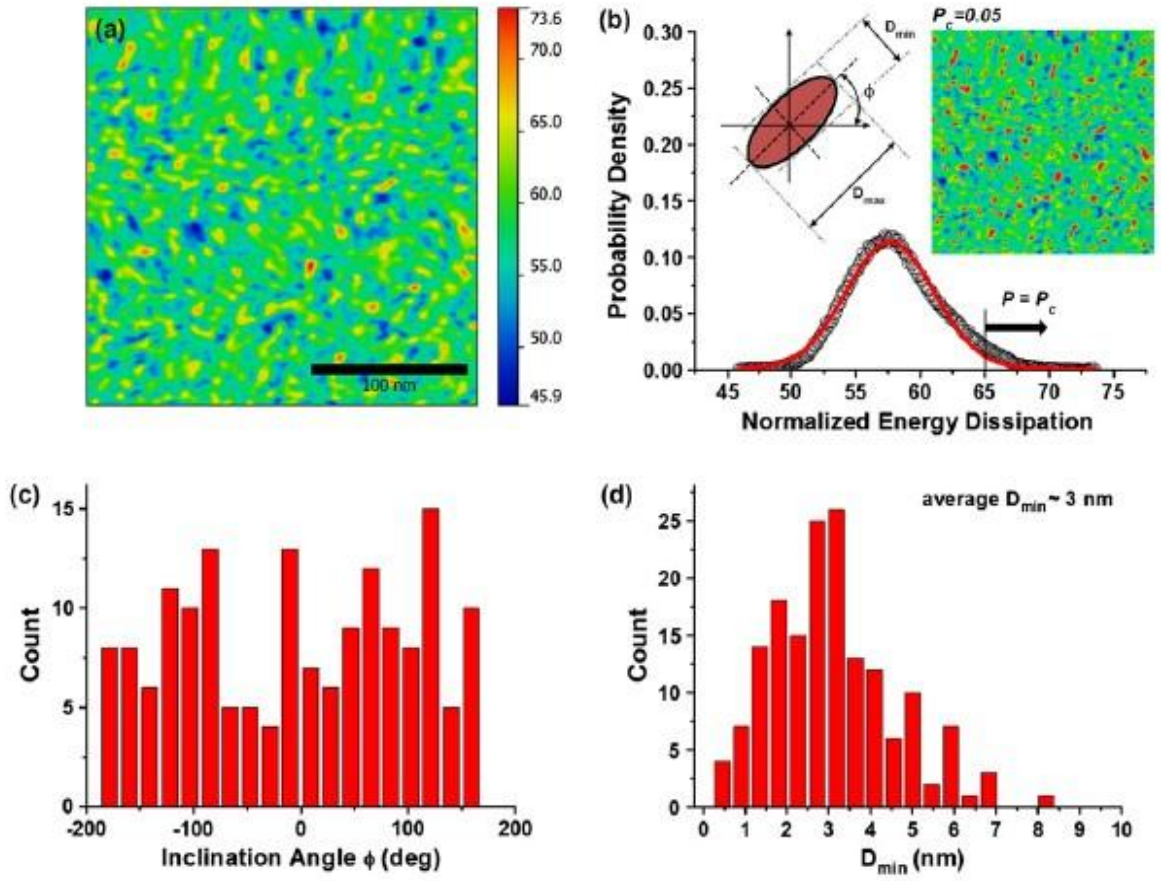

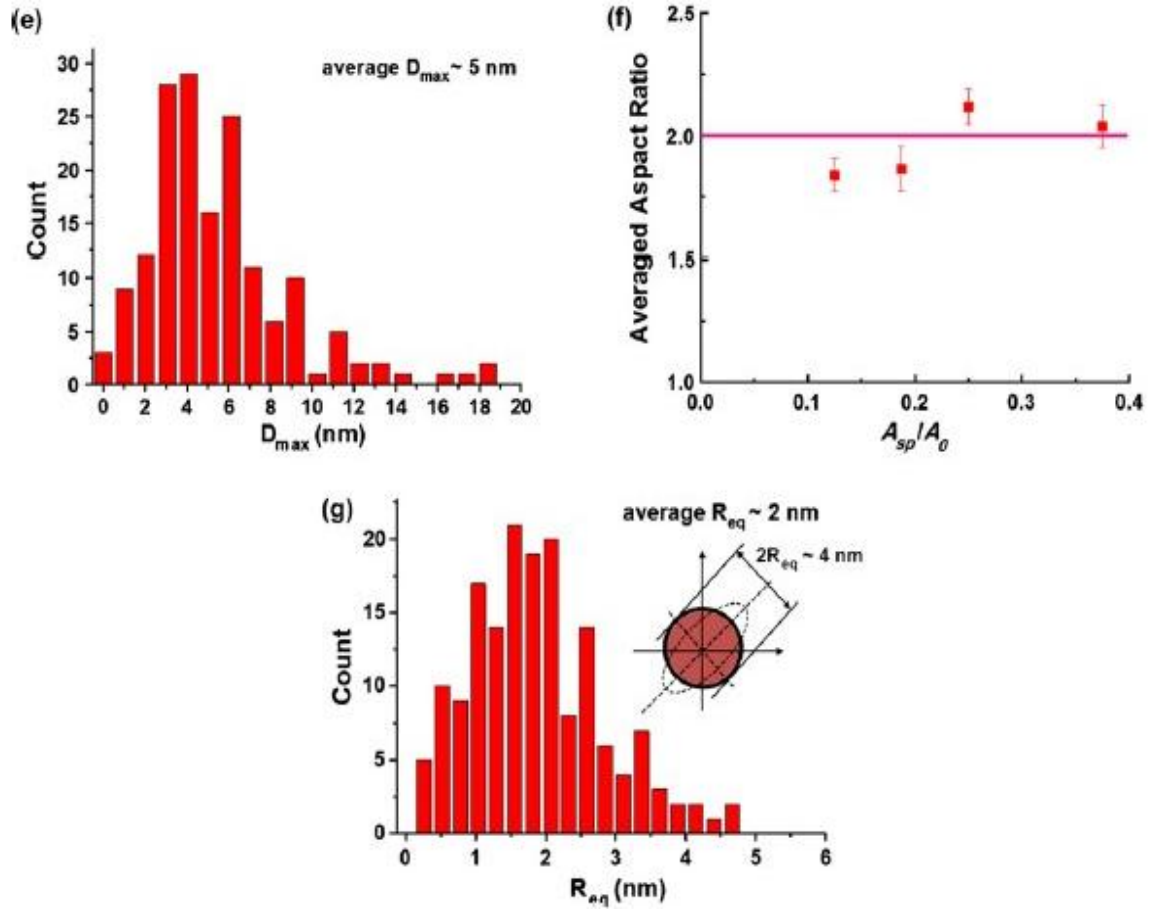

Figure 5.4 (a) The structural contrast formed through the normalized energy dissipation at $A_{sp} / A_0 = 0.15$, (b) the Gaussian-type probability density distribution of the normalized energy dissipation [the insets: (left) the sketch illustrating different geometric parameters defined for an elliptical loose-packing region and (right) the highlight of the loose-packing phases in (a) by shading them uniformly in red.], and the histograms of (c) the inclination angle ϕ of the loose-packing phases, the lengths of (d) short axis, D_{min}, and (e) long axis, D_{max}, and (f) the equivalent disk radius, R_{eq}, of the loose-packing phases [the sketch in the inset of (e) demonstrates the definition of R_{eq}].

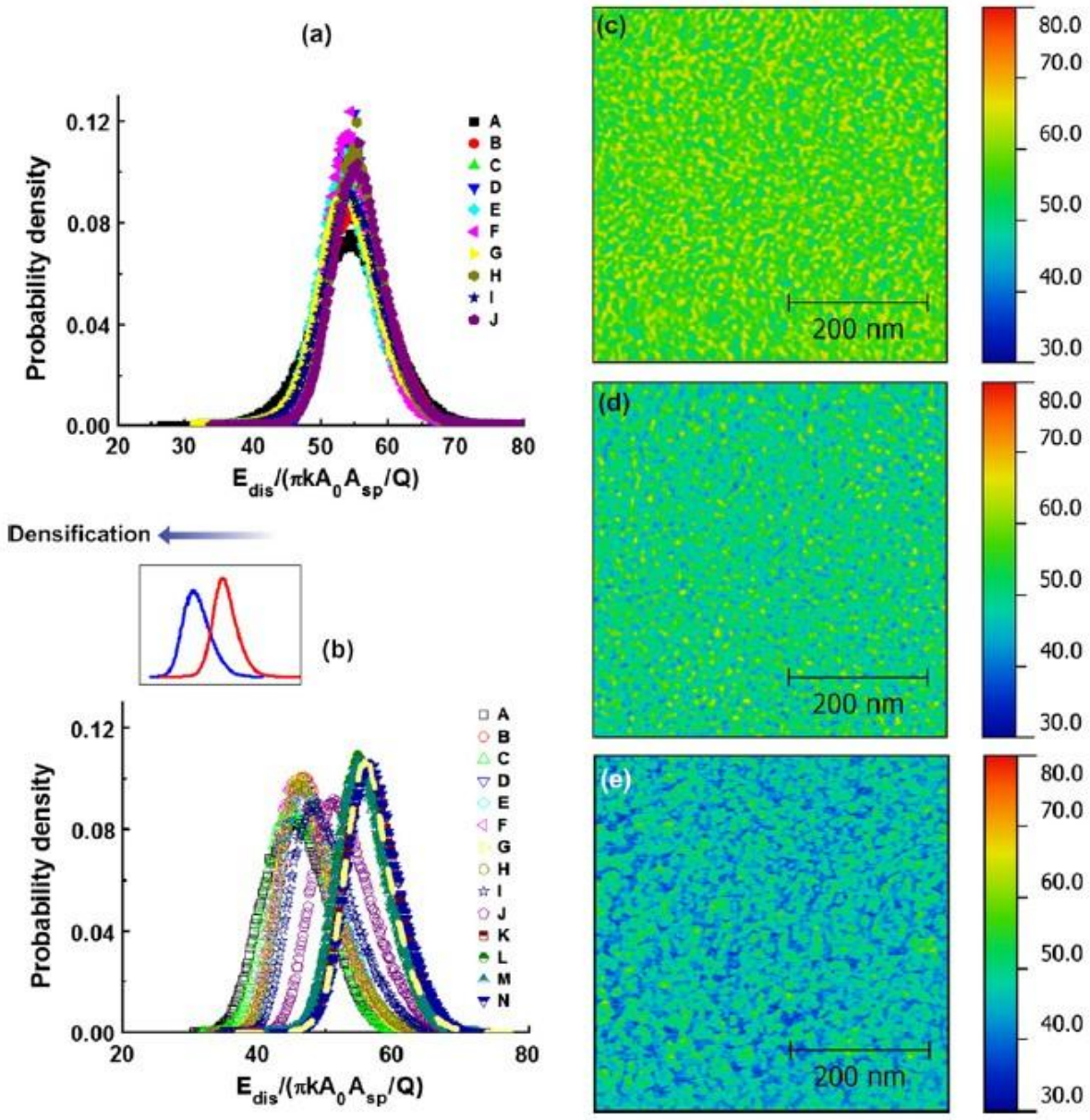

Figure 5.5 Structural characterization of the $Zr_{70}Ni_{30}$ thin film before and after isothermal annealing. (a) the energy spectra obtained by scanning 10 random sites of a 500 nm x 500 nm size before annealing; (b) the energy spectra obtained by scanning 14 random sites of the same size after annealing [Note that the dotted yellow line indicates the average position of the energy spectrum before annealing and the inset highlights the difference in the energy spectrum obtained before (red curve) and after (blue curve) annealing]; and the structural contrast formed (c) before annealing, (d) after mild annealing, and (e) after deep annealing. [Note that the localization of the scanning place is designated by the letter in (a) and (b)].

To avoid surface oxidation, a thin film wrapped in a Ti thin foil was heat treated in a high vacuum (10^{-5}torr). This was done by first increasing the temperature at rate of 20 K min^{-1} to a peak value of ~650 K, then immediately cooling it down to the room temperature. According to the research of X. J. Liu et al. and K. Georgarakis (X.J. Liu, X.D. Hui et al. 2009; K. Georgarakis, A. R. Yavari et al. 2010), this temperature is close to the glass transition temperature (~647K) obtained by heating a Zr-Ni MG with a similar chemical composition at a rate of ~1 K s^{-1}. In theory, this kind of heat treatment allows the Zr-Ni thin film to enter the supercooled liquid region momentarily but is insufficient to cause overall structural crystallization, as confirmed by our subsequent X-ray analysis (data not shown here). Note that, unlike in normal isothermal annealing, our heat treatment was not carried out by holding the peak temperature for a certain time and the heat conduction was unlikely to be constant. As a consequence, the film surface may not reach a thermal equilibrium during the experiment. This did, however, provide us with an opportunity to image the film surface as it was annealed to different degrees.

To track the annealing-induced structural evolution, we first checked whether the AFM images obtained by scanning the local areas could represent the structure of the whole film prior to annealing. To this end, we scanned at least 10 random sites of the same size (500 nm × 500 nm) before the thermal annealing. As shown in Fig.5.5 (a), the obtained energy spectra are very similar, implying that the thin film statistically possesses the same structure across the different scanning areas. In comparison, the energy spectra obtained the same way after the thermal annealing are more “scattered”, as seen in Fig.5.5 (b), suggesting that the annealing process did not occur uniformly over the whole film. In some places, the obtained energy spectra remain

almost identical to those in Fig.5.5 (a); while in others the obtained energy spectra are shifted as a whole towards the low energy side, indicating the densification of the overall atomic packing.

By further comparing the shapes of the energy spectra [see the inset of Fig.5.5 (b)], one can also see that the energy spectrum becomes broadened and skewed to its low energy side after the annealing. This shape change implies that the structural densification tends to develop in the relatively dense-packing phases, causing the unified movement of the left branch of the energy spectrum; nevertheless, there may be a large energy barrier within some loose-packing phases against such structural densification, which causes the energy spectrum to become skewed to the low energy side after the annealing. As transforming a loose-packing phase to a dense-packing one entails structural contraction, our current results suggest that, in some loose-packing regions, the elastic strain energy caused by local structural contraction may outweigh the energy reduction due to local structural relaxation, which therefore sets a higher barrier energy for these loose-packing phases than for the dense-packing ones, even though, kinetically, there is more room for atoms to rearrange themselves inside the loose-packing regions. As the width of the energy spectrum is a manifestation of the local structural heterogeneity, i.e. a narrow spectrum width corresponds to a more uniform structure and vice versa, the broadening and skewing of the energy spectrum indicates an increasing degree of local structural heterogeneity.

Note that similar conclusions may be drawn from the results obtained from the thermal annealing experiments carried out on bulk samples, in which the change in the atomic structure was inferred from 1-D volume-averaging data, such as X-ray and neutron diffraction spectra (U. Köster, J. Meinhardt et al. 1997; L. Yang, J. Z. Jiang et al. 2005). However, in contrast to those

conventional techniques, our current nanoscale approach provides direct evidence that reveals the evolution of loose- and dense-packing phases simultaneously on a 2-D plane.

As mentioned above, our current approach is unique in that it enables to directly see how a large structure evolves in the metallic glass through the contrast formed by the local energy dissipation. By making use of the spatial non-uniformity of the thermal annealing, we can track the evolution of atomic packing by studying the structural images taken from the local areas annealed to various degrees. Figures 5.5 (c)-(e) display three such AFM images which represent the three distinct annealing status of the film, i.e. before annealing, after mild annealing and after deep annealing, respectively. As seen from these images, the atomic structures so selected clearly show the general trend of atomic-packing densification through a reduction in energy-dissipation. Furthermore, by using the aforementioned boundary-defining criterion, we can also study how the loose- and dense-packing phases evolve in the annealing process. To single out the loose-packing phases, we fix the corresponding cut-off energy at ~68%, which corresponds to P_c = 0.05 before the annealing. As seen in Figs.5.6 (a)-(d), the loose-packing phases are randomly dispersed in the thin film with a size distribution between ~1 and ~5 nm before the annealing [Fig.5.6 (a)]; whereas after the annealing their number and size diminish rapidly as a result of the densification in those places where the loose-packing phases reside [Figs.5.6 (b)-(d)]. By comparing Figs.5.6 (a) with (d), one can clearly see that the overall darkening of the image contrasts, which indicates that, with further annealing, the densification of the relatively dense-packing phases becomes more dominant than the transformation of the loose- to dense-packing phases.

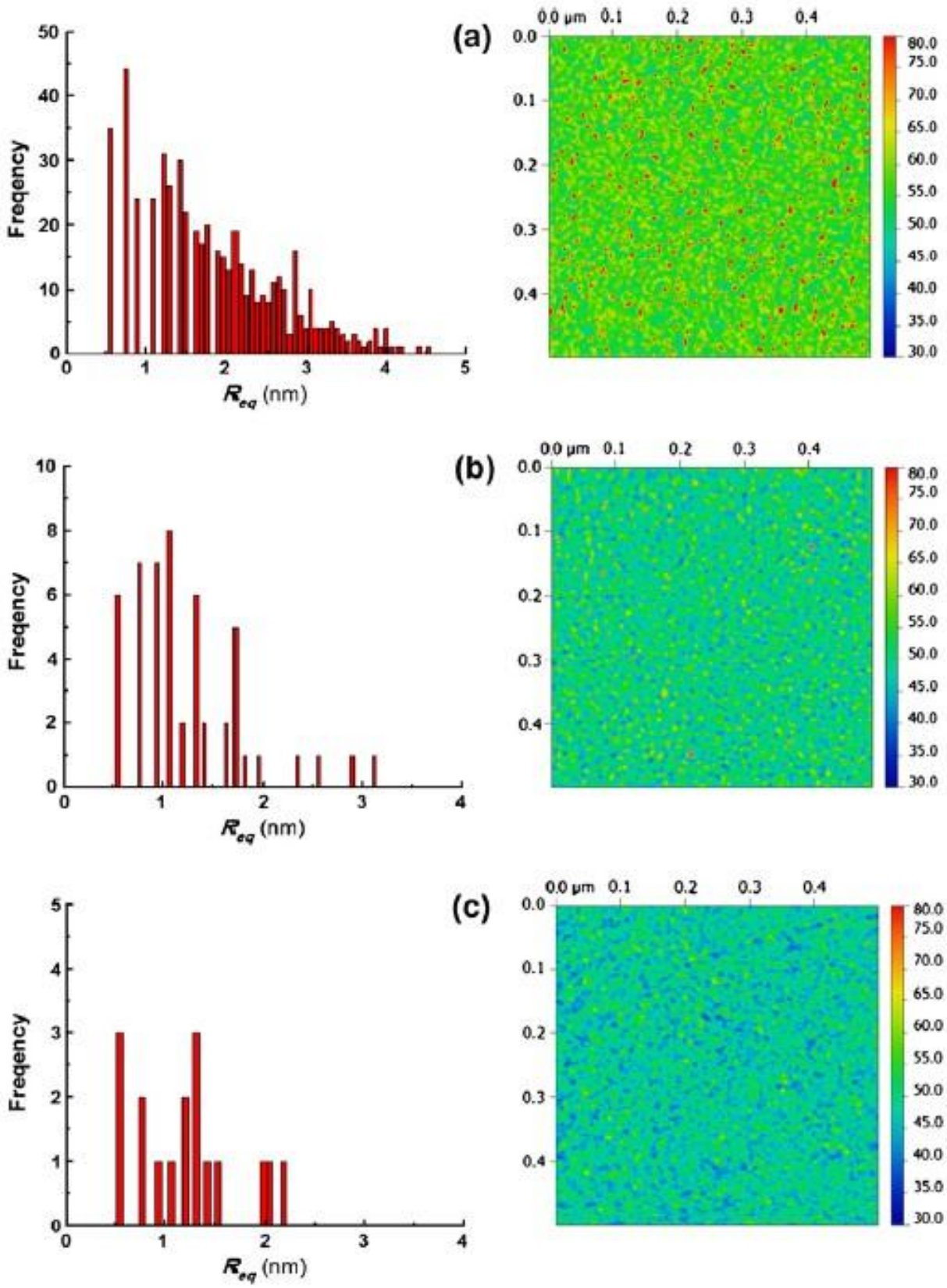
(a)
Freqency
R_{eq} (nm)
0.0 μm
(b)
Freqency
R_{eq} (nm)
(c)
Freqency
R_{eq} (nm)

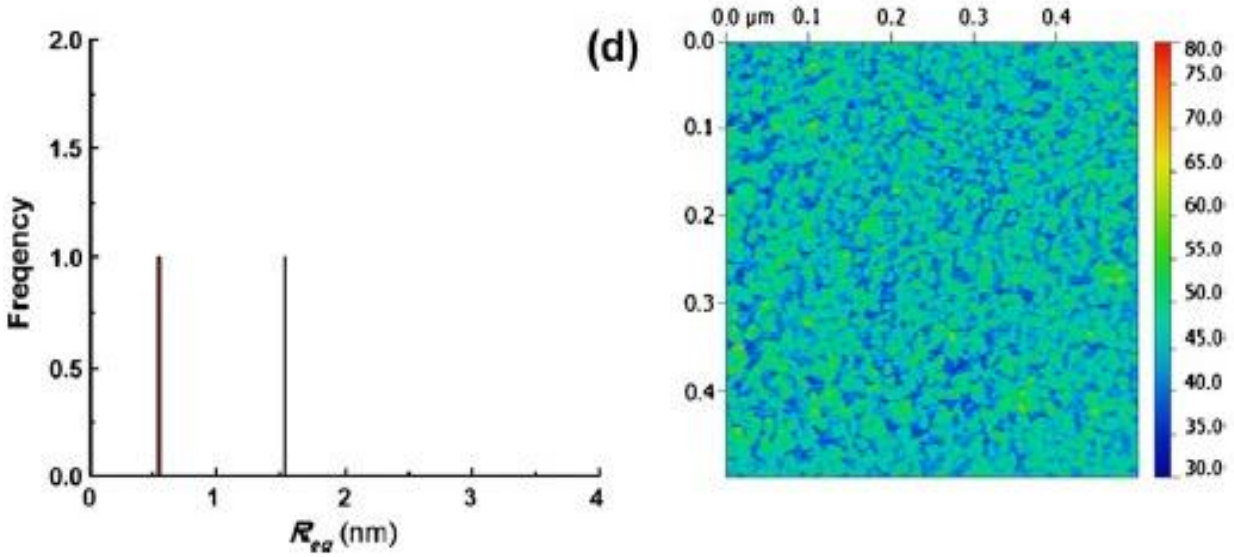

Figure 5.6 The annealing-induced annihilation of the loose-packing phases characterized by $E_{dis}Q/\pi kA_{sp}A_0 \geq 68\%$. (a) the structural contrast of the film before annealing; (b)-(d) the structural contrast of the film subject to an increasing extent of annealing. (Note that the images shown to the left are the histograms for the average size of the loose-packing phases while to the right are the corresponding AFM images with the loose-packing phases being highlighted in red).

As the opposite of the loose-packing phases, the dense-packing phases are defined herein as those consuming the bottom P_c = 5% of the total energy being dissipated before the annealing, which is equivalent to fixing the normalized cut-off energy at ~ 45% for them. Instead of tracking the growth of the individual dense-packing phases, which is not feasible for this study because the scanned images were taken from different areas, we employ a statistical approach here to study the accumulated size distribution of the dense-packing phases. For this purpose, we compute the accumulated counts,

$$N\left(\overline{R}\right) = \sum_{R_{eq} \geq R} n\left(R_{eq}\right) \tag{5.1}$$

which sum over all dense-packing phases with a size greater than a pre-defined cut-off value $\overline{R}$. It should be emphasized here that R_{eq} refers to the radius of a circle that has the same area as the interconnected dense-packing phases rather than the physical size of the individual dense-packing phases, and *n* is the number of the cluster of the dense-packing phases with the size of R_{eq}. In practice, one can make a double-logarithmic plot of *N* vs. $\overline{R}$ and examines its trend line to gain insights into the growth behavior of the clusters.

According to M. E. J. Newman's findings (M. E. J. Newman 2005), the shape of the accumulated size distribution is an indication of how the densification takes place via the growth or clustering of the dense-packing phases. When the thin film is slightly annealed, their accumulated size distribution is of a Gaussian type (Curve 'A1'), implying that the dense-packing phase clusters are all bounded in size [Fig. 5.7 (a)]. With further annealing, the Gaussian-type size distributions become "stretched", which yields a larger mean and standard deviation, as shown by the Curves A2 - A7. This behavior implies that the already formed cluster of dense-packing phases continues to grow, while newly formed dense-packing phases of a smaller size emerge. Interestingly, their accumulated size distribution ultimately transforms to a power-law scaling (the Curves A8 and A9). According to the results of M. E. J. Newman and Feder J. (Feder J. 1988; M. E. J. Newman 2005), the power-law scaling signals the formation of a fractal-dimensioned supercluster, which can have a divergent and sample-spanning size. Note that the fractal growth of the dense-packing phases can be also revealed visually by our AFM images. As shown in Fig.5.7 (b), one can vividly see the sequence of how the dense-packing phases and their clusters emerge, grow and finally link up to produce a ramified network structure, which is reminiscent of a statistical fractal object (Feder J. 1988).

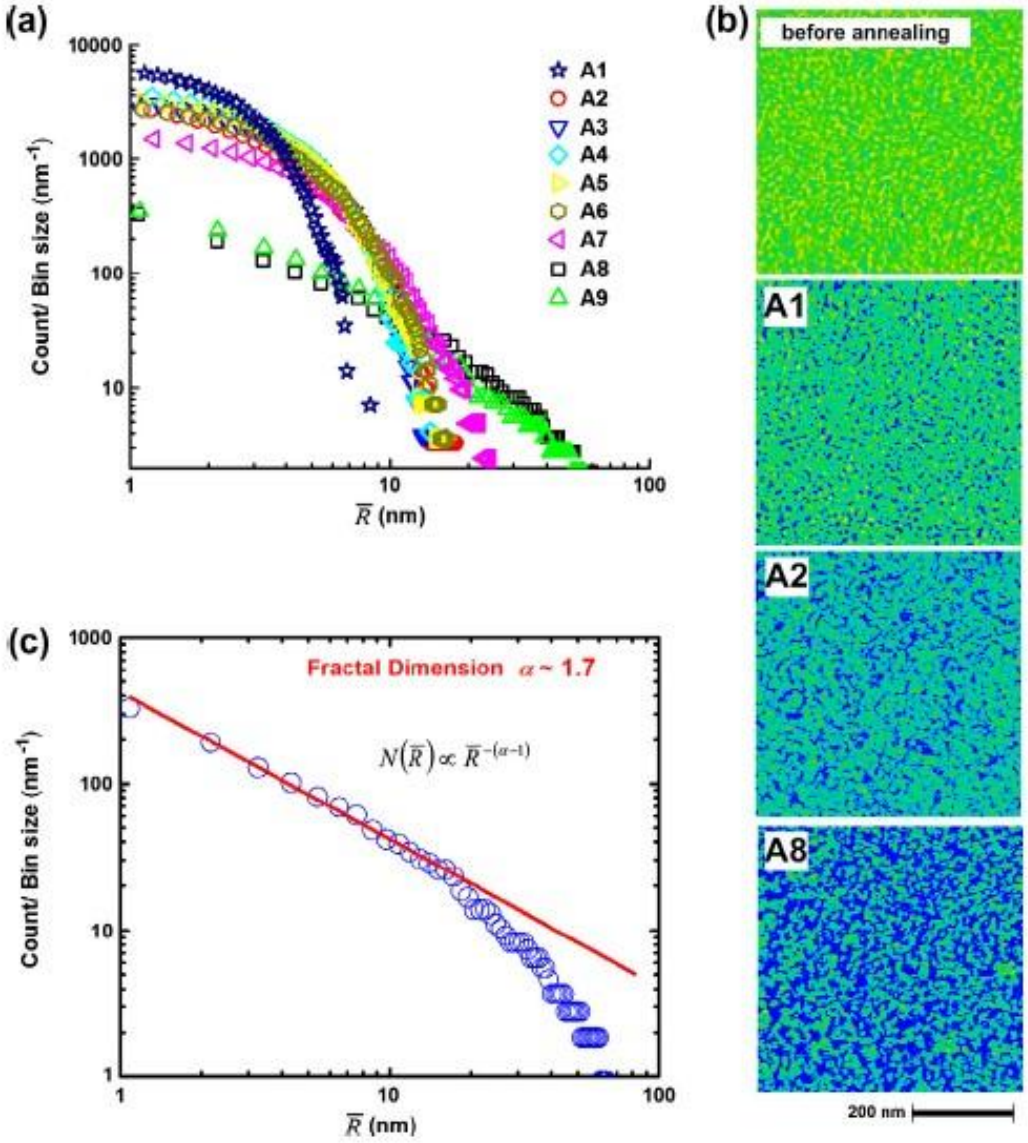

Figure 5.7 The annealing-induced formation of a fractal-like network of the dense-packing phases characterized by $E_{dis}Q/\pi kA_{sp}A_0 \leq 45\%$. (a) the accumulated size distributions of the dense-packing regions [note that the designation of the curves (A1-A9) are in an ascending order of annealing]; (b) the structural images rendered with the same color bar showing vividly the emergence of a fractal-like super-cluster (note that the dense-packing regions are highlighted in blue for clarity); and (c) the power-law size scaling for the accumulated size distribution of the dense-packing regions with an exponential cut-off. [Note that the count shown in (a) and (c) is normalized by the bin size to remove the statistic bias for data comparison].

Figure 5.7 (c) highlights the details of such a power-law scaling. Due to the finite size effect (Feder J. 1988), an exponential cut-off is also seen in Fig.5.7 (c). According to the research of Feder J. (Feder J. 1988), the power law scaling, $N\left(\overline{R}\right) \propto \overline{R}^{-(\alpha-1)}$, defines a "cluster fractal dimension", α. To estimate α, we follow a rigorous mathematic procedure as detailed in the publications of M. E. J. Newman and Dimiduk D. M. et al.(M. E. J. Newman 2005; Dennis M. Dimiduk, Chris Woodward et al. 2006) rather than directly fitting the power-law portion of the curve, which yields $\alpha = 1.7 \pm 0.2$ (see the **Appendix B** for details). Interestingly, a similar fractal dimension of 1.63 –1.7 was found in many other 2-D patterns generated in a variety of physical processes, such as dielectric break-down (L. Niemeyer, L. Pietronero et al. 1984) and metal leaf growth (Matsushita M., Hayakawa Y. et al. 1985). Despite being driven by different growth mechanisms, the formation of such fractal-dimensioned superclusters shares the common kinetic origin of diffusion limited aggregation (DLA) (Feder J. 1988). According to Refs (Ling Yang, Michael K Miller et al. 2009; Q. Wang, C. T. Liu et al. 2011), the development of local dense atomic packing in the Zr-based MGs entails both a local topological rearrangement and diffusion-assisted chemical redistribution. Since nucleation sites for dense-packing phases are limited and atom diffusion is hindered in MGs (A. Inoue 2000), the dense-packing phases cannot grow to a large size on their own and, therefore, it is feasible that the fractal growth of the dense-packing phases, as seen in the MG, is also governed by the DLA mechanism. Note that the above statistical analysis is based upon a particular cut-off energy (= 45%) for the dense-packing phases. In general, we can redo the whole analysis by selecting a different cut-off value. In this way, we can produce a general coordinate system, as shown in Fig.5.8, with the abscissa representing the annealing status of the MG thin film and the ordinate the selected cut-off energy.

For each row of the structural images shown along the abscissa, their overall atomic packing is increasingly densified from left to right. Interestingly, regardless of the selected cut-off energy, the same kind of fractal super-cluster is found with a fractal dimension of ~ 1.7, which indicates that our analysis is robust and that previous findings are indeed the outcome of the annealing process rather than an image artifact.

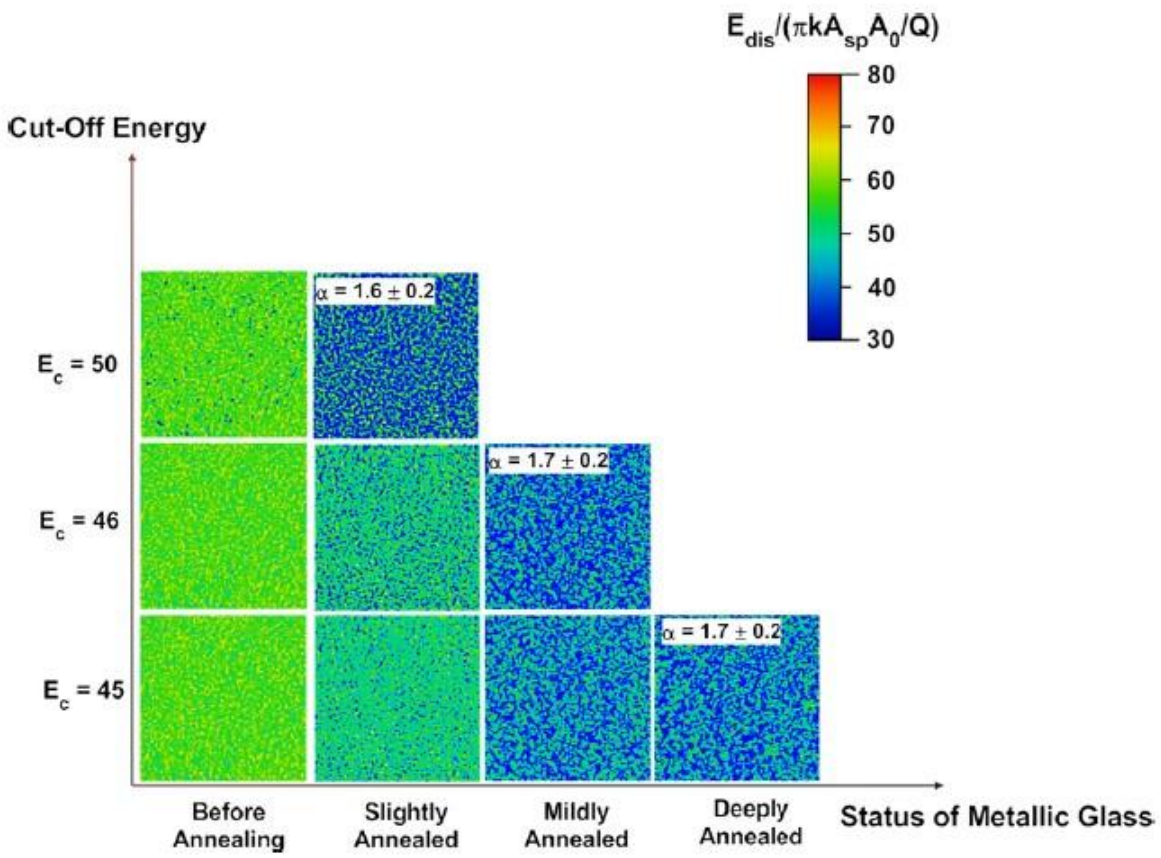

Figure 5.8 The sequence of structural evolution in the metallic-glass thin film displayed on the general coordinate system. Regardless of the selected cut-off energy, the same fractal dimension α of ~1.7 is obtained from the images in which the interconnected dense-packing regions exhibit a power-law scaling in their accumulated size distribution (note that all the AFM images are rendered using the same color scale as shown at the upper-right corner, and the dense-packing regions are highlighted in blue).

5.4 Implications

In the MG literature, one debatable issue is whether or not the atomic-packing in metallic glasses should be of a fractal dimension (Y.Q. Cheng and E. Ma 2011). According to Ma et al (D. Ma, A.D. Stoica et al. 2009), an apparently universal fractal dimension of ~ 2.3 was obtained for a variety of bulk metallic-glasses (BMGs) through the study of their X-ray and neutron diffraction peaks (D. Ma, A.D. Stoica et al. 2009); in sharp contrast, no fractal-dimension was detected the same way in the simulated MGs (Y.Q. Cheng and E. Ma 2011), which were obtained computationally from metallic melts via an extremely fast cooling rate. Given that a DLA pattern has a theoretical fractal dimension of ~ 1.7 in two dimensions and ~ 2.5 in three dimensions (Feder J. 1988), the fractal dimension of ~ 2.3 obtained from the BMGs (D. Ma, A.D. Stoica et al. 2009) is in line with the fractal dimension of ~1.7 obtained in this study. If the fractal dimension of ~2.3 was really "universal", as suggested by Ma et al. (D. Ma, A.D. Stoica et al. 2009), then how could one explain the findings that the simulated MGs exhibit a packing dimension close to ~ 3, as reported by Cheng and Ma (Y.Q. Cheng and E. Ma 2011). Here, we suggest an explanation to reconcile this seeming contradiction.

Based on our current AFM findings, we argue that the simulated small-sized MGs relative to the bulk counter-parts are analogous to our as-deposited MG thin film relative to the annealed ones. In that regard, the fractal growth of the dense-packing phases, which can contribute to incident X-ray (or neutron) beam-diffraction events, is most likely not yet completed in the simulated MGs. If this were the case, it would not be surprising for a non-fractal dimension or a fractal dimension other than ~2.3 to be obtained from the diffraction peaks;

by comparison, the fractal dimension of ~2.3 seen in many types of BMGs is a manifestation of the completes fractal growth of the dense-packing phases at a slow cooling rate.

Based on the above discussions, we may draw the conclusion that the cooling rate should play an important role in the fractal packing of atomic clusters in MGs – which was ignored in the previous studies (D. Ma, A.D. Stoica et al. 2009; Y.Q. Cheng and E. Ma 2011).

5.5 Conclusion

To conclude, the current article can be divided into two parts. In the first part, we discuss how one can obtain a high-resolution atomic force microscopy image of the nanoscale structure in an MG thin film through the correction of the surface adhesion and topography effects. In the second part, we provide in unprecedented detail experimental evidence of how atomic packing evolves in an annealed Zr-Ni MG thin film. Through the experimental results, we have shown the fractal growth of the dense-packing phases in the MG thin film. Considering the similarity between the thermal annealing of an MG and the vitrification of a glass-forming liquid at different cooling rates, an important insight can be gained into the cooling rate effect on the atomic structure of MGs, that is, as compared to a fast cooling rate, a slow cooling rate tends to promote the fractal growth of the dense-packing phases. As a result, MGs obtained by slow cooling become more densely packed, with a fractal packing dimension and enhanced local structural heterogeneities.

5.6 Appendix A

Deconvolution of Surface Topographic Information from Phase Imaging

According to Stark et al. (Martin Stark, Clemens Möller et al. 2001), the phase shift $\Delta\varphi$ measured in the AM-AFM is a convoluted result of local energy dissipation and surface topography. In theory, this measured phase shift can be formulated as $\Delta\varphi = \Delta\varphi_{dis} + \Delta\varphi_{surf}$, in which $\Delta\varphi_{dis}$ and $\Delta\varphi_{surf}$ denote the phase shift due to energy dissipation and surface topography, respectively. Under the integral-proportional feedback control, it can be shown that $\Delta\varphi_{surf} \propto \delta A_{sp}$, where δA_{sp} is the recorded amplitude error (Martin Stark, Clemens Möller et al. 2001). In such a case, the subtraction of $\Delta\varphi_{surf}$ from $\Delta\varphi$ can be achieved by finding a coefficient β such that the standard deviation of $\Delta\varphi - \beta\delta A_{sp}$ could be minimized (Martin Stark, Clemens Möller et al. 2001). Note that $\Delta\varphi = \Delta\varphi(x, y)$ and $\delta A_{sp} = \delta A_{sp}(x, y)$ are both functions of the 2D coordinates *x*, *y*, and the coefficient β can be derived as:

$$\beta = \frac{E\left(\Delta\varphi \bullet \delta A_{sp}\right) - E\left(\Delta\varphi\right) \bullet E\left(\delta A_{sp}\right)}{D\left(\delta A_{sp}\right)} \tag{A1}$$

Where $E(\bullet)$ and $D(\bullet)$ denote respectively the mean and standard deviation of a physical quantity.

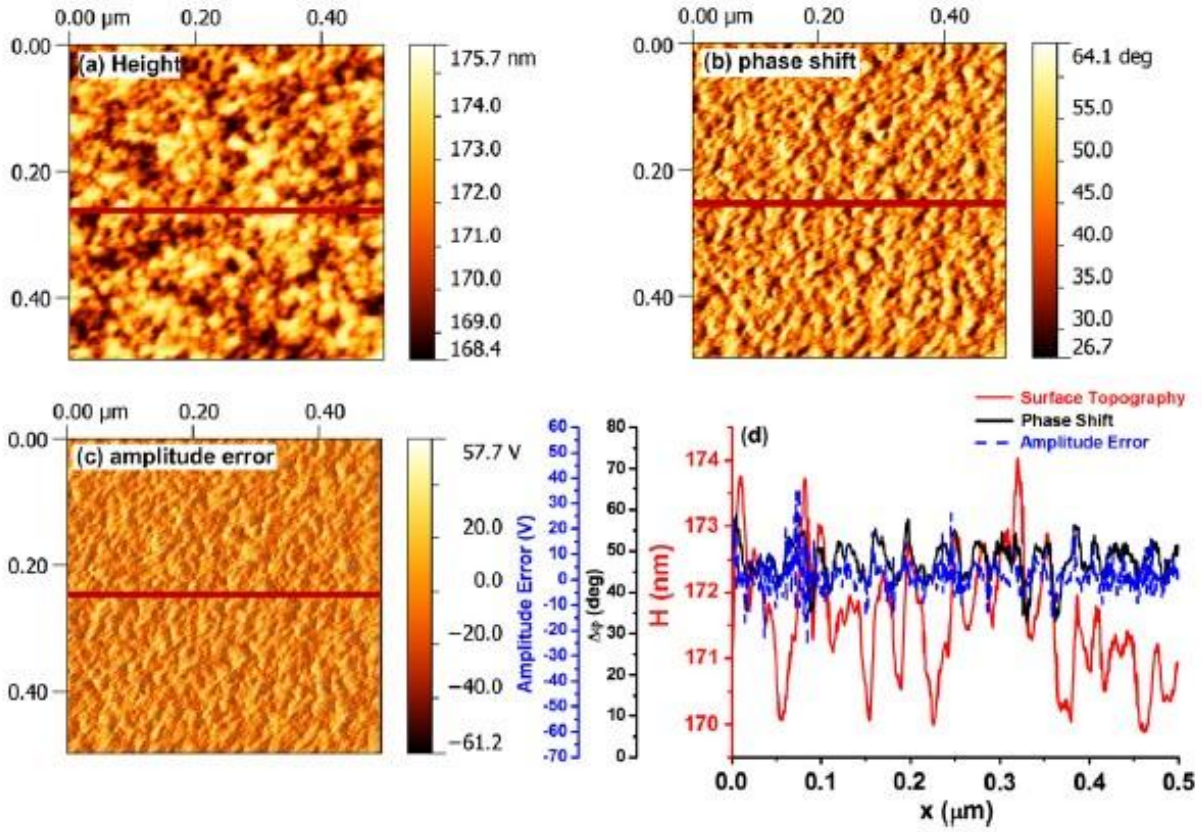

Figure A1 The AFM images obtained simultaneously from a same area of the film. (a) The height image, (b) the phase image, (c) the amplitude-error image, and (d) the comparison of the line-scan results obtained at the middle section (red line) of (a)-(c).

For the sake of illustration, Figures A1 (a)-(c) display the height, phase and amplitude error images obtained simultaneously by scanning a same area on the metallic-glass thin film, from which it can be easily perceived that, as opposed to the apparently dissimilar height and phase images, the spatial patterns shown on the phase and amplitude-error images look alike. This observation can be further justified through the comparison of the line-scan results across the mid-section of all three AFM images [Fig. A1 (d)]. From these observations, it can be

inferred that the measured phase shift contains information not only from local energy dissipation but also from surface topography. To remove such a surface topography effect, Eq. (A1) is utilized to compute the appropriate value of β and subsequently, a new phase image is generated by performing the operation of image subtraction $\Delta\varphi - \beta\,\delta A_{sp}$.

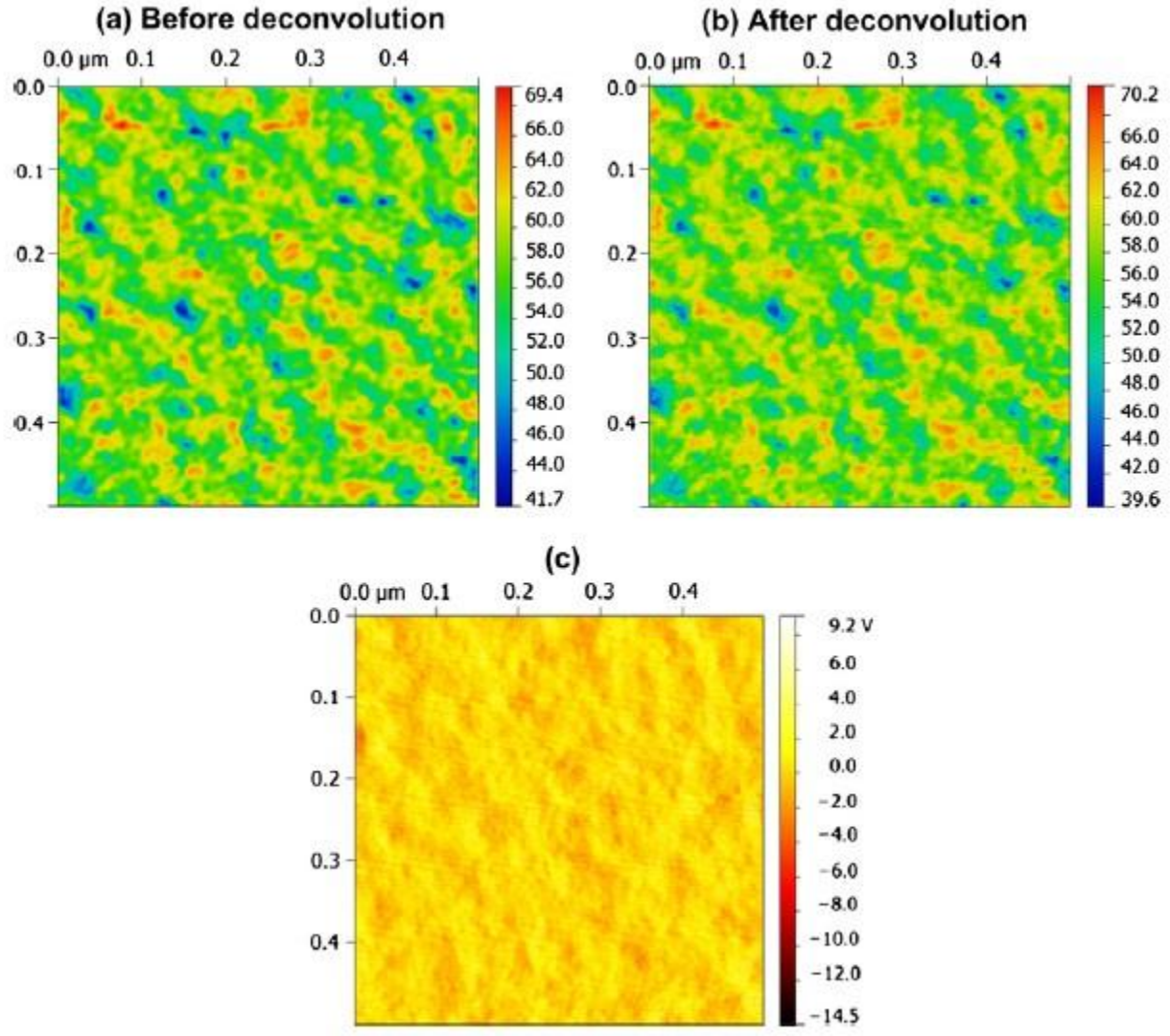

Figure A2 The AFM energy-dissipation images obtained (a) before and (b) after the deconvolution of the surface topography from the corresponding phase image; and (c) the amplitude-error image used for the deconvolution.

[Note that (b) is obtained at $A_{sp}/A_0 = 0.15$ and $\beta = 0.077$].

For comparison, Figures A2 (a)-(b) display one energy-dissipation image obtained at $A_{sp}/A_0 = 0.15$ before and after the deconvolution. Owing to the atomic-scale smoothness of the film surface, which exhibits the root-mean-square roughness of less than ~ 1 nm, we found that the β value deduced from the original phase [Fig. A2 (b)] and amplitude-error images [Fig. A2 (c)] was negligibly small and only about ~ 0.077. As a result, only a minor change occurred to the contrast of the deconvoluted energy-dissipation image, as shown in Fig. A2(b). Similar results were also obtained from other AFM images acquired at different A_{sp}/A_0 ratios. Despite that, the surface topography information has been decovoluted from the phase images subsequently being used for constructing the structural images.

5.7 Appendix B

Maximum Likelihood Estimate of Fractal Exponent

To estimate the fractal exponent α, the power-law distribution $p(x) = C\,x^{-\alpha}$, where C is a normalization factor such that $\int_{x_{\min}}^{\infty} p(x)\,dx = 1$ and x_{min} is the minimum of a set of n values x_i, can be cast into the following form:

$$p(x) = \frac{\alpha - 1}{x_{min}} \left(\frac{x}{x_{min}} \right)^{-\alpha} \qquad (B1)$$

Given $x_i \ (i = 1, 2, \cdots, n)$, the likelihood of the data sets can be expressed as $P(x \mid \alpha) = \prod_{i=1}^{n} p(x_i)$. According to the Bayes' law, this gives us the probability $P(\alpha \mid x)$ of a particular value of α, which is $P(\alpha \mid x) = P(x \mid \alpha) P(\alpha) / P(x)$. According to Newman (M. E. J. Newman 2005), the prior probability of the exponent α should be uniform, i.e. a constant independent of α. Thus, maximizing $P(\alpha \mid x)$ with respect to α gives:

$$\alpha = 1 + n \left[\sum_{i=1}^{n} ln \frac{x_i}{x_{min}} \right]^{-1} \qquad (B2)$$

Furthermore, from the width of the maximum of the likelihood as a function of α, the standard error σ of the estimated α can be derived as (M. E. J. Newman 2005):

$$\sigma = \sqrt{n} \left[\sum_{i=1}^{n} ln \frac{x_i}{x_{min}} \right]^{-1} = \frac{\alpha - 1}{\sqrt{n}} \qquad (B3)$$

By applying (B2) and (B3) to the measured data points within the power-law portion of the accumulated size distribution, we can thus estimate the fractal dimension for the growth of the dense-packing phases as $\alpha = 1.7 \pm 0.2$ in the metallic-glass thin film.

5.8 References

A. Inoue (2000). "A. Stabilization of metallic supercooled liquid and bulk amorphous alloys." Acta. Mater. **48**: 8.

A.S. Argon (1979). "Plastic deformation in metallic glasses." Acta Metall. **27**(1): 12.

Akihiko Hirata, Pengfei Guan, Takeshi Fujita, Yoshihiko Hirotsu, Akihisa Inoue, Alain Reza Yavari, Toshio Sakurai and Mingwei Chen (2010). "Direct observation of local atomic order in a metallic glass." Nature Materials Letters **10**: 6.

Cang Fan, P. K. Liaw, T. W. Wilson, W. Dmowski, Th. Proffen, H. Choo and C.T. Liu (2006). "Structural Model for Bulk Amorphous Alloys." Appl. Phys. Lett. **89**(11): 3.

D. Ma, A.D. Stoica and X.-L. Wang (2009). "Power-law scaling and fractal nature of medium-range order in metallic glasses." Nature Mater. **8**(1): 5.

D. Pan, A. Inoue, T. Sakurai and M. W. Chen (2008). "Experimental characterization of shear transformation zones for plastic flow of bulk metallic glasses." PNAS **105**(39): 4.

D.B. Miracle (2004). "A structural model for metallic glasses." Nature Materials **3**: 6.

Dennis M. Dimiduk, Chris Woodward, Richard LeSar and Michael D. Uchic (2006). "Scale-free intermittent flow in crystal plasticity." Science **312**: 3.

Feder J. (1988). Fractals, New York: Plenum Press.

Garcia R and Perez R. (2002). "Dynamic atomic force microscopy methods." Surface Science Reports **47**: 105.

H. W. Sheng, W. K. L UO, F. M. Alamgir, J. M. Bai and E. Ma (2006). "Atomic Packing and Short-to-medium Range Order in Metallic Glasses." Nature **439**: 7.

J. C. Ye, C. T. Liu, Q. Wang and Y. Yang (2010). "Atomistic Free-Volume Zones and Inelastic Deformation of Metallic Glasses." Nature Materials **9**(8): 5.

J. P. Cleveland, B. Anczykowski, A. E. Schmid and V. B. Elings (1998). "Energy dissipation in tapping-mode atomic force microscopy." Appl. Phys. Lett. **72**(20): 3.

K. Georgarakis, A. R. Yavari, M. Aljerf, D. V. Louzguine-Luzgin, M. Stoica, G. Vaughan and A. Inoue (2010). "On the atomic structure of Zr–Ni and Zr–Ni–Al metallic glasses." Journal of Applied Physics **108**: 7.

L. Niemeyer, L. Pietronero and H. J. Wiesmann (1984). "Fractal Dimension of Dielectric Breakdown." Physical Review Letters **52**(12): 5.

L. Yang, J. Z. Jiang, T. Liu, T. D. Hu and T. Uruga (2005). "Atomic structure in Zr70Cu29Pd1 metallic glass." Appl. Phys. Lett. **87**(6): 3.

Ling Yang, Michael K Miller, Xun-Li Wang, CT Liu, AD Stoica, Dong Ma, J Almer and D Shi (2009). "Nanoscale solute partitioning in bulk metallic glasses." Adv. Mater. **21**(3): 4.

M. E. J. Newman (2005). "Power laws, Pareto distributions and Zipf's law." Contemp Phys **46**: 28.

Martin Stark, Clemens Möller, Daniel J. Müller and Reinhard Guckenberger (2001). "From Images to Interactions: High-Resolution Phase Imaging in Tapping-Mode Atomic Force Microscopy." Biophysical Journal **80**: 10.

Matsushita M., Hayakawa Y. and Sawada Y. (1985). "Fractal structure and cluster statistics of zinc-metal trees de- posited on a line electrode." Physical Review A **32**(6): 3.

Nicol´as F Mart´ınez and Ricardo Garc´ıa (2006). "Measuring phase shifts and energy dissipation with amplitude modulation atomic force microscopy." Nanotechnology **17**: 6.

P. J. James, M. Antognozzi, T. J. M. J. Tamayo, J. M. Newton and M. J. Miles (2001). "Interpretation of Contrast in Tapping Mode AFM and Shear Force Microscopy. A Study of Nafion." Langmuir **17**: 12.

Q. Wang, C. T. Liu, Y. Yang, Y. D. Dong and J. Lu (2011). "Atomic-Scale Structural Evolution and Stability of Supercooled Liquid of a Zr-Based Bulk Metallic Glass." Phys. Rev. Lett. **106**(21): 4.

Qi-Kai Li and Mo Li (2007). "Assessing the critical sizes for shear band formation in metallic glasses from molecular dynamics simulation." Appl. Phys. Lett. **91**: 3.

T. Egami (2011). "Atomic level stresses." Progress in Materials Science **56**(6): 17.

U. Köster, J. Meinhardt, S. Roos and R. Busch (1997). "Formation of quasicrystals in bulk glass forming Zr-Cu-Ni-Al alloys." Materials Science and Engineering: A **226-228**: 4.

W. Dmowski, T. Iwashita, C.-P. Chuang, J. Almer and T. Egami (2010). "Elastic Heterogeneity in Metallic Glasses." Phys. Rev. Lett. **105**.

William L. Johnson, Marios D. Demetriou, John S. Harmon, Mary L. Lind and Konrad Samwer (2007). "Rheology and Ultrasonic Properties of Metallic Glass-Forming Liquids: A Potential Energy Landscape Perspective." MRS Bulletin **32**(08): 7.

X.J. Liu, X.D. Hui, G.L. Chen and T. Liu (2009). "Local atomic structures in Zr–Ni metallic glasses." Physics Letters A **373**(29): 6.

Y. Yang, J. F. Zeng, J. C. Ye and J. Lu (2010). "Structural inhomogeneity and anelastic deformation in metallic glasses revealed by spherical nanoindentation." Appl. Phys. Lett. **97**: 3.

Y.H. Liu, D. Wang, K. Nakajima, W. Zhang, A. Hirata, T. Nishi, A. Inoue and M.W. Chen (2011). "Experimental Characterization of Nanoscale Mechanical Heterogeneity in a Metallic Glass." Physical Review Letters **106**: 17.

Y.Q. Cheng and E. Ma (2011). "Atomic-level structure and structure–property relationship in metallic glasses." Progress in Materials Science **56**: 95.

Yang Y and Liu C.T. (2012). "Size effect on stability of shear-band propagation in bulk metallic glasses: an overview." Journal of Materials Science **47**(1): 13.

6. Nano-scale Structural Mapping of Thin Film Metallic Glass with Dynamic Atomic Force Microscopy

In this chapter, we summarize the recent use of the high-resolution dynamic atomic force microscopy (DAFM) in mapping the nano-scale dynamical structural heterogeneity in thin film metallic-glasses (TFMGs). Our focus is laid on the major factors which can influence the structural contrast in the DAFM images, such as tip radius, free-amplitude, set-point amplitude and surface roughness. Finally, through a comparative study of different TFMGs and single-crystal silicon, we demonstrate that the DAFM technique is an effective method to distinguish different amorphous structures through their nano-scale energy dissipation spectra. Other than that, our experimental results also show that, aside from their great potential for a wide range of engineering applications, TFMGs could also serve as a good model material for the fundamental research on the amorphous structure of metallic glasses (MGs).

6.1 Introduction

Unlike crystalline metals with a periodic atomic structure, metallic glasses (MGs) possess an amorphous structure lack of any long-range translational symmetry. Despite the amorphous 'maze' often shown on an electron microscopy image, local 'motifs' of atomic packing, such as the icosahedral and crystal-like packing (D.B. Miracle 2004; H. W. Sheng, W. K. L UO et al. 2006; C. Fan, P.K. Liaw et al. 2009; Q. Wang, C. T. Liu et al. 2011), can still be identified from atomistic simulations or electron microscopy. While these static structural features, often known as the short- or medium-range order (SRO or MRO), are commonly referred to as the structural building blocks of MGs in the literature (D.B. Miracle 2004; H. W. Sheng, W. K. L UO et al. 2006; C. Fan, P.K. Liaw et al. 2009; Q. Wang, C. T. Liu et al. 2011), however, amorphous structures are not meant to be 'static'. Under a thermal or mechanical loading, they can be

relaxed or rejuvenated, transitioning from one glassy configuration to another along the potential energy landscape (PEL) (J. C. Ye, C. T. Liu et al. 2010). According to the recent simulations (Dasgupta, Karmakar et al. 2012), at the onset of yielding, these events of structural rearrangements can span a spatial dimension of several orders of magnitude larger than the size limit (1-3 nm) of SRO or MRO (H. W. Sheng, W. K. L UO et al. 2006; Q. Wang, C. T. Liu et al. 2011). This behavior implies that, in order to gain a holistic structural understanding of MGs, one must turn to the dynamic aspect of amorphous structure. In principle, it is the amorphous structure **'in motion'** that gives rise to the different properties of MGs; therefore, it is worthwhile to characterize their dynamic structural heterogeneities in one way or another (J. C. Ye, C. T. Liu et al. 2010; W. Dmowski, T. Iwashita et al. 2010; Y. Yang, J.C. Ye et al. 2010; Y.H. Liu, D. Wang et al. 2011; Y. Yang, J.F. Zeng et al. 2012).

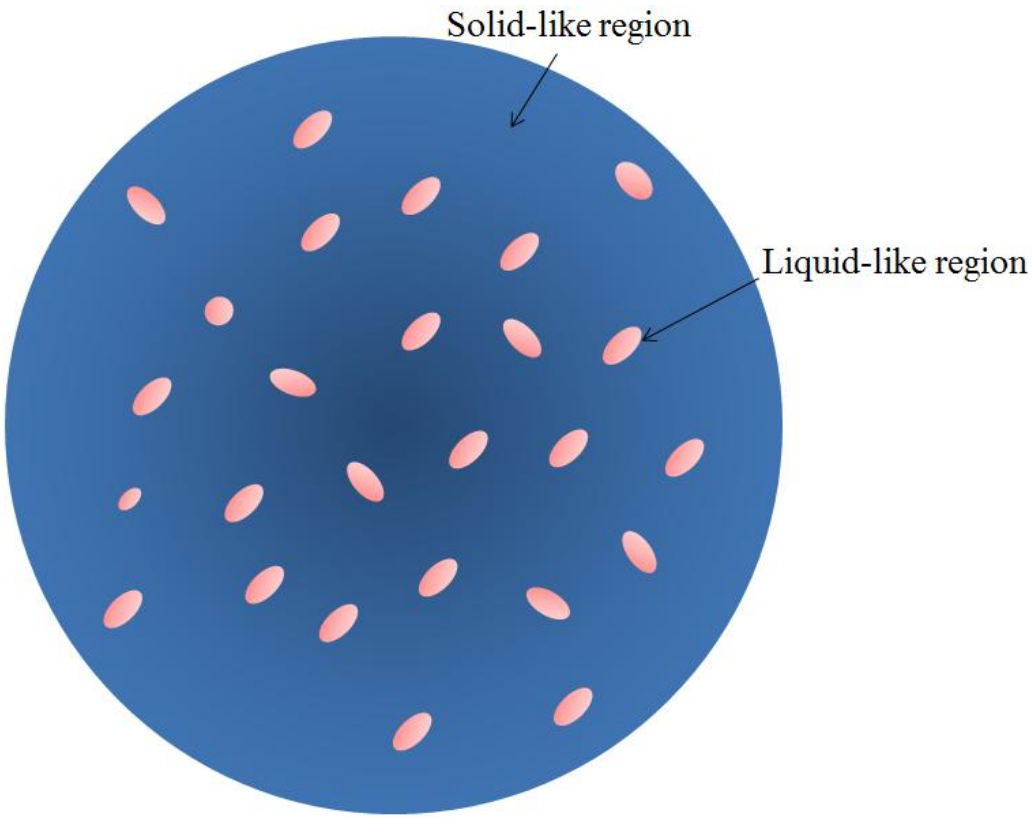

Figure 6.1 The schematics of the amorphous structure of MGs.

In principle, the amorphous structure of MGs can be depicted as a nano-scale composite, consisting of loose- and dense-packing atoms (Fig.6.1) (C. Fan, P.K. Liaw et al. 2009). When perturbed by an external agent, the dense-packing atoms respond elastically; whereas the loose-packing ones respond inelastically, of which the behavior resembles that of 'residual' supercooled liquids trapped within an elastic 'matrix' (J. C. Ye, C. T. Liu et al. 2010). Therefore, as a reflection of the underlying structural heterogeneity, the MGs as a whole deform in an anelastic fashion.

Recently, several experimental techniques have been devised or employed to reveal anelasticity in MGs, including the cyclic microcompression by Ye et al. (J. C. Ye, C. T. Liu et al.

2010), the X-ray diffraction from deformed samples by Dmowski et al. (W. Dmowski, T. Iwashita et al. 2010), the high-rate nanoindentation by Yang et al. (Y. Yang, J. F. Zeng et al. 2010), and the dynamic atomic force microscopy (DAFM) by Liu et al. (Y.H. Liu, D. Wang et al. 2011) and Yang et al. (Y. Yang, J.F. Zeng et al. 2012). In those experiments, the detected anelastic deformation spans a wide range of length scales (1 nm – 1 mm) (J. C. Ye, C. T. Liu et al. 2010; W. Dmowski, T. Iwashita et al. 2010; Y. Yang, J.C. Ye et al. 2010; Y.H. Liu, D. Wang et al. 2011; Y. Yang, J.F. Zeng et al. 2012), which suggests that, although anelasticity originates from the sites with a local structural heterogeneity, however, these sites are distributed 'homogenously' in the MG. Consequently, one can observe anelasticity at different length scales once these local sites become activated, as seen in the molecular dynamics (MD) simulations recently performed by Fujita et al (Fujita, Wang et al. 2012). Among the above experimental techniques, the DAFM method may be the most powerful one as its spatial resolving capability provides a feasible means to map out the whole amorphous structure on a 2-D plane (Y.H. Liu, D. Wang et al. 2011; Y. Yang, J.F. Zeng et al. 2012). Nevertheless, its use is limited only to thin film metallic-glasses (TFMGs) at this moment due to a stringent surface requirement, which will be discussed in the later text.

6.2 Theoretical Analysis and Experimental Set-Up

6.2.1 DAFM and Nano-Scale Energy Dissipation

Before the discussions of our experiments, we would like to have a brief overview of the DAFM method and the associated energy dissipation mechanisms at the nano-scale. In practice, there are a number of dynamic modes available for operating an AFM. However, our discussion is herein

limited to the amplitude-modulation (AM) AFM, also known as the tapping-mode AFM in the literature (Garcia 2010). Under this dynamic mode, a vibrating AFM tip is engaged with a sample surface at a pre-defined set-point amplitude and vibration frequency. Conceptually, this type of dynamic engagement is equivalent to 'feeding' the sample surface with the same amount of mechanical energies. However, the energy being actually dissipated varies with the site-specific material structure and some other factors, such as surface capillary forces and roughness (J. P. Cleveland, B. Anczykowski et al. 1998; Javier Tamayo and Ricardo Garc á 1998; Garcia R and Perez R. 2002; Garcia 2010; Y. Yang, J.F. Zeng et al. 2012).

Regardless of the nano-scale energy dissipation mechanisms, the energy dissipated per cycle, E_{dis}, can be expressed as (J. P. Cleveland, B. Anczykowski et al. 1998):

$$E_{dis} = \frac{\pi k A_{sp} A_0}{Q}\left[\sin\left(\frac{\pi}{2} - \Delta\varphi\right) - \frac{A_{sp}}{A_0}\frac{\omega}{\omega_0}\right] \tag{6.1}$$

where k is the spring constant of the AFM cantilever; A_{sp} and A_0 denote, respectively, the set-point and free amplitude; Q is the quality factor; $\Delta\varphi$ is the phase shift measured by the DAFM; and ω and ω_0 represent the respective driving and resonant frequency. Meanwhile, the time-average force (F_{ts}) exerted on the sample surface can be also derived, which is $F_{ts} = \frac{F_0}{2}\cos\left(\pi/2 - \Delta\varphi\right)$, where $F_0 = \frac{kA_0}{Q}$ (Garcia 2010). These equations constitute the basic nano-mechanics 'toolkit' for the structural characterization with DAFM.

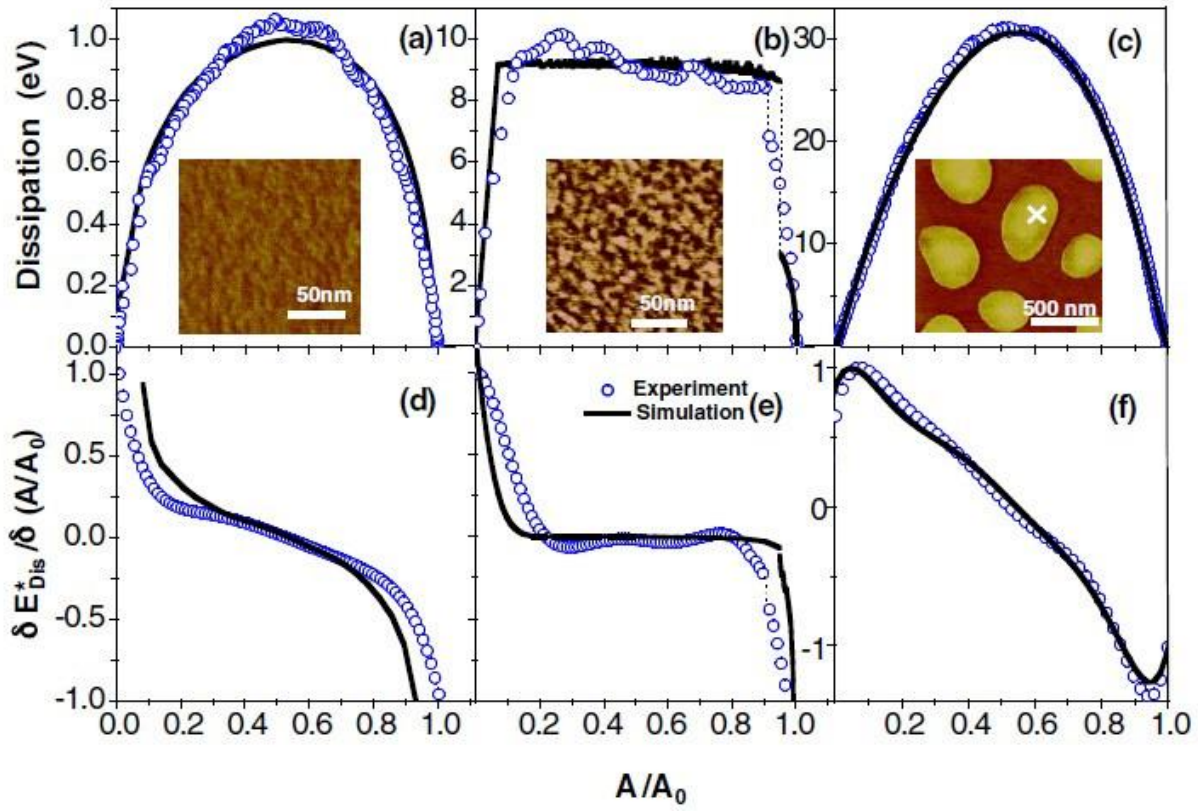

Figure 6.2 (a)-(c) The measured and simulated dynamic dissipation curves E_{dis} as a function of the amplitude ratio A/A_0 and (d)-(f) the corresponding derivatives. Note that (a) and (d) are obtained on a silicon surface with A_0=6.6nm and k=2N/m, (b) and (e) on a silicon with A_0=32.5nm and k=2N/m, and (c) and (f) on a PS region in the blend of a PS/PB polymer with A_0=15nm. Note that the images are taken from (R. Garcia, C. J. Go ́mez et al. 2006).

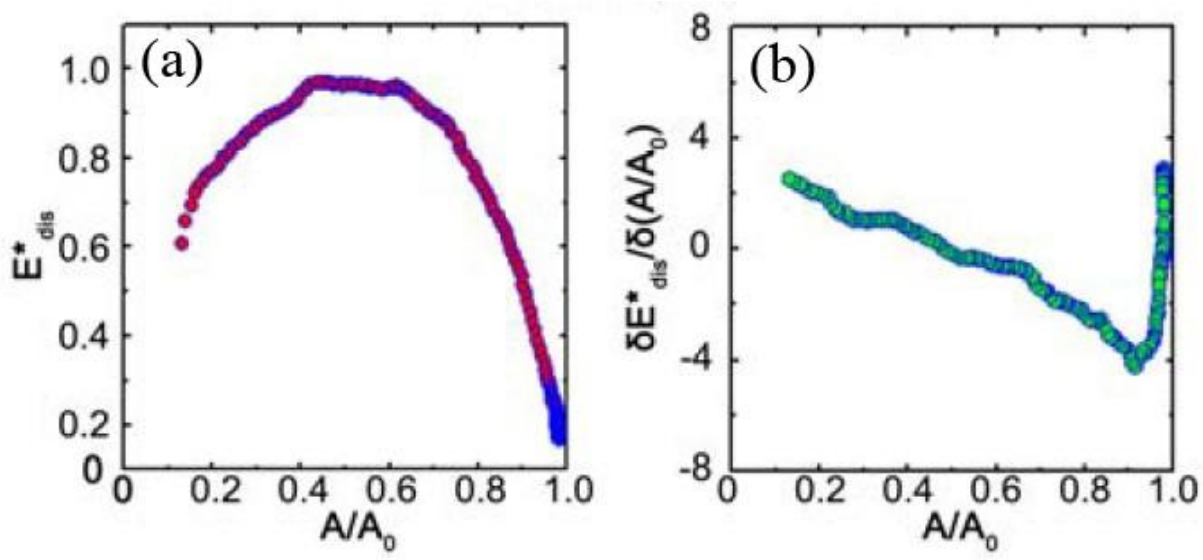

Figure 6.3 (a) The normalized energy dissipation (E^*_{dis}) spectrum and (b) its derivative as a function of the amplitude ratio A/A_0 for the $Zr_{55}Cu_{30}Ni_5Al_{10}$ TFMG (Y.H. Liu, D. Wang et al. 2011).

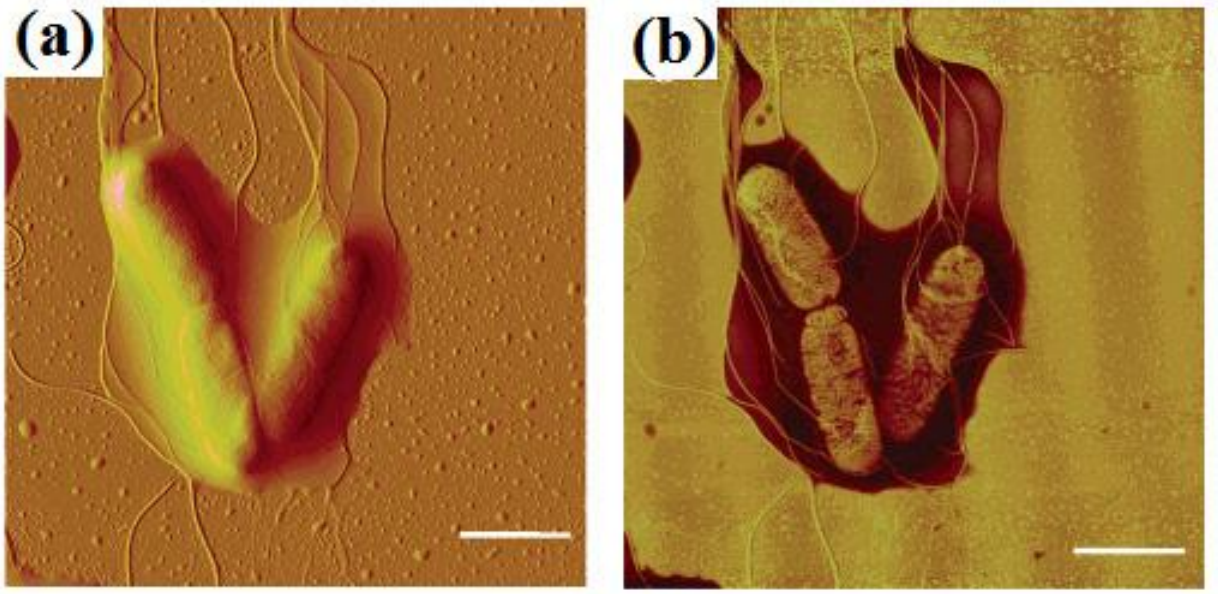

Figure 6.4 (a) The topography and (b) phase shift image of the three *S. typhimurium* cells covered by an EPS capsule (the scale bars = 2 μm). Note the DAFM images are taken from (Zhiyong Suo, Xinghong Yang et al. 2007).

In 2006, Garcia et al. (R. Garcia, C. J. Go ́mez et al. 2006) provides a convenient way to identify the mechanisms of nano-scale energy dissipation in the DAFM. In their work, three different dissipation mechanisms are studied, including the energy dissipation due to long-range surface attraction, surface hysteresis and sample viscoelasticity (or anelasticity for metals). In practice, the three mechanisms can be keyed to the three distinctive curves of $\delta E_{dis}/\delta\left(A_{sp}/A_0\right)$ versus A_{sp}/A_0, respectively, as shown in Figs. 6.2a-f. For the case of TFMGs, Liu et al. (Y.H. Liu, D. Wang et al. 2011) recently demonstrated that the nano-scale energy dissipation spectrum obtained from the Zr-based TFMG is consistent with that of anelasticity, as shown in Figs. 6.3a-b, which is consistent with the theory and modeling (C. Fan, P.K. Liaw et al. 2009; J. C. Ye, C. T. Liu et al. 2010; Fujita, Wang et al. 2012). Here, it is worth mentioning that, although the DAFM-based structural characterization has been used only recently for MGs, similar applications were existent for decades and are ubiquitous in other fields, such as polymeric and biological materials. For example, Figures 6.4a-b show a S. typhimurium cell imaged by the DAFM (Zhiyong Suo, Xinghong Yang et al. 2007). Although there are no visible structural features on the surface topography image (Fig. 6.4a), the presence of the three cells is evident on the corresponding phase image due to the viscoelasticity of the underlying biological materials (Fig. 6.4b).

6.2.2 Material and Experimental Set-Up

In our current work, three materials were selected for the structural imaging by DAFM, including the $Zr_{70}Ni_{30}$ TFMG, the $Zr_{53}Cu_{29}Al_{12}Ni_6$ TFMG and a bulk single-crystal silicon. The procedures for the film deposition and the characterization of their amorphous structures have been

described in our previous work (J. C. Ye, J. P. Chu et al. 2012; Y. Yang, J.F. Zeng et al. 2012), which are omitted here for brevity.

The DAFM experiments were subsequently conducted on the Bruker™ multimode AFM platform. For comparison, different AFM tips were used with a varying set-point A_{sp}, such as the regular tapping-mode silicon tip with a radius~10 nm and the specially designed sharp tip coated with a diamond-like carbon (DLC) nanotube with a tip radius ~1 nm. To simply the analysis, the driving frequency of the AFM tip was fixed at the resonant value.

6.3 Results and Discussions

6.3.1 Tip-Radius Effect

In the DAFM applications, one of the most commonly used tips is a silicon (Si) tip with a radius of ~10 nm. Given their wide availability, it is necessary to discuss the feasibility of using this kind of tips for the structural imaging of MGs. Since anelasticity can take place over a wide range of length scales, one should be able to detect the signals of anelasticity even with these common tips, provided that all other working parameters of the AFM system are tuned appropriately. Figures 6.5a-b show two energy dissipation maps obtained, respectively, from the $Zr_{70}Ni_{30}$ TFMG by using the regular Si-tip and the special DLC-tip. Note that the working parameters, such as A_0 and A_{sp}, are set equal for both cases but the stiffness k and damping factor Q of the AFM probes are slightly different. For the sake of comparison, the energy dissipation E_{dis}, shown on the color bar of Figs. 6.5a-b, is normalized by the maximum value. Evidently, in terms of structural contrast, the sharp tip gives a much better result than the blunt one. Using the

autocorrelation method, we obtained a correlation length of ~3 nm for Fig. 6.5a and ~7 nm for Fig. 6.5b. Considering that the typical size of SRO and MRO and that of a STZ event is around 1-3 nm (H. W. Sheng, W. K. L UO et al. 2006; Y.H. Liu, D. Wang et al. 2011), it is certain that the special DLC-tip is more suitable for the structural imaging of TFMGs. As such, all the DAFM images as presented hereafter in this chapter were obtained using the DLC-tips.

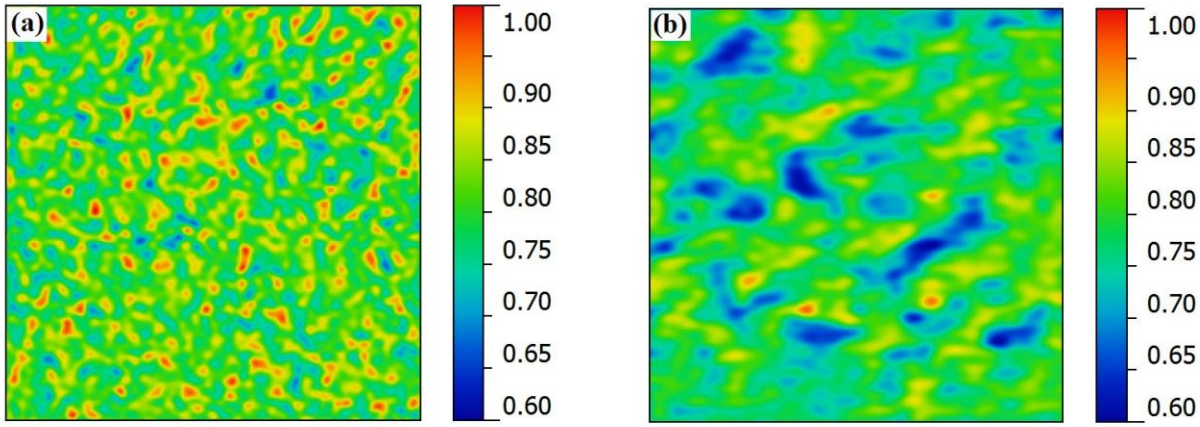

Figure 6.5 The normalized energy dissipation mapping obtained from the $Zr_{70}Ni_{30}$ TFMG by (a) a standard Si-Tip (radius~10nm) and (b) a DLC-Tip (radius~1nm). Note that the scan size for both DAFM images is 500 nm.

6.3.2 Free Amplitude (A_0) Effect

In principle, the same amount of mechanical energies can be dissipated via either surface attraction or repulsion(Garcia 2010). For our AFM system, an attractive tip-surface interaction corresponds to a negative phase shift while a repulsive interaction to a positive phase shift. Different from a repulsive tip-surface interaction, which is due to a real material response and produces the desired structural contrast, an attractive tip-surface interaction is usually caused by capillary forces. As such, the negative phase shifts measured from our AFM system were

regarded as artifacts and discarded from the subsequent image analyses (Y. Yang, J.F. Zeng et al. 2012). Therefore, in order to obtain the structural contrast, one has to adjust the few working parameters through fine tuning, such as the free amplitude A_0 and the set-point ratio (A_{sp}/A_0), so that positive phase shifts can be collected through the feed-back system of the AFM.

Conceptually, a repulsive force is favored at a short tip-surface distance. Under the AM mode, we can indirectly control the mean distance between the AFM tip and the sample surface by manipulating the set-point ratio A_{sp}/A_0. In theory, a high set-point ratio corresponds to a large tip-surface distance and vice versa (Garcia 2010). In such a case, it might appear straightforward to enforce a repulsive tip-surface interaction if one could just keep reducing the set-point ratio until a positive phase shift finally arise from the TFMG surface. Nevertheless, if the free amplitude A_0 is set low, it is possible that one can only acquire negative phase shifts over a wide range of set-point ratios. This is because, in the case of a wet surface, there could be a strong surface capillary force which can effectively drag down the vibration amplitude of the AFM tip. As a result, the action of the attractive force along is sufficient to meet the pre-fined set-point amplitude. This free amplitude effect was noticed a few years ago, and has been systematically studied by Garcia et al. (Garcia R and Perez R. 2002) and others (Nicol´as F Mart´ınez and Ricardo Garc´ıa 2006). Here, we observed the same effect by trying out different free amplitudes A_0 on the $Zr_{70}Ni_{30}$ TFMG.

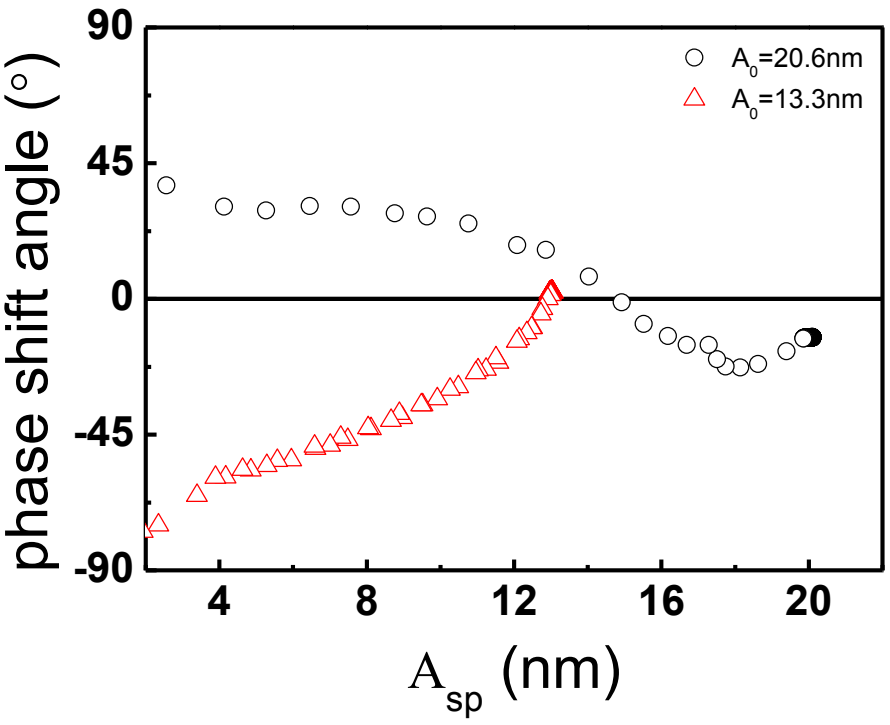

Figure 6.6 The phase shift as a function of the set-point amplitude A_{sp} obtained from the $Zr_{70}Ni_{30}$ TFMG at two different free amplitudes A_0.

Figure 6.6 shows two curves of phase shift versus set-point amplitude obtained from the $Zr_{70}Ni_{30}$ TFMG at two different free amplitudes. For A_0 ~21 nm, the measured phase shift appears negative when A_{sp} > ~15 nm due to the action of a surface attraction; with the reduction in A_{sp}, the sign of the phase shift is changed to positive, signaling the action of a surface repulsion when A_{sp} < ~15 nm. By comparison, for A_0 ~ 13 nm, only the negative phase shifts can be measured over a wide range of A_{sp} (2 nm < A_{sp} < 13 nm). This trend indicates that there might be a strong local capillary force at the moment of the AFM scanning; therefore, only the attractive tip-surface interaction can be sensed by the system. Note that the phase shift curves shown in Fig. 6.6 were obtained from a single contact point. To construct a DAFM image, the AFM tip typically needs to make intermittent contacts over an area consisting of 512×512 points.

Generally speaking, this corresponds to a huge amount (~ 2.5×10^5) of phase shift curves, which could vary from point to point even for a fixed free amplitude A_0.

6.3.3 Set-Point Ratio Effect

Based on the above discussions, it is clear that, once the free amplitude A_0 is fixed, we has to adjust the set-point ratio such that the tip-surface interactions over the whole scanning area can be tuned to repulsion. In other words, we have to ensure that the measured phase shift angles are all positive. Figures 6.7a-f show a series of height and phase images acquired by repeatedly scanning a same area on the surface of the $Zr_{70}Ni_{30}$ TFMG with DAFM. As seen in these figures, it is evident that the tip-surface interaction is attractive in some regions at a high set-point ratio (A_{sp}/A_0 ~ 0.75), which gives rise to the negative phase shifts seen in Fig. 6.7a. As expected, when the set-point ratio is set low (A_{sp}/A_0 < 0.75), we can now acquire positive phase shifts over the whole scanning area (Figs. 6.7b-f).

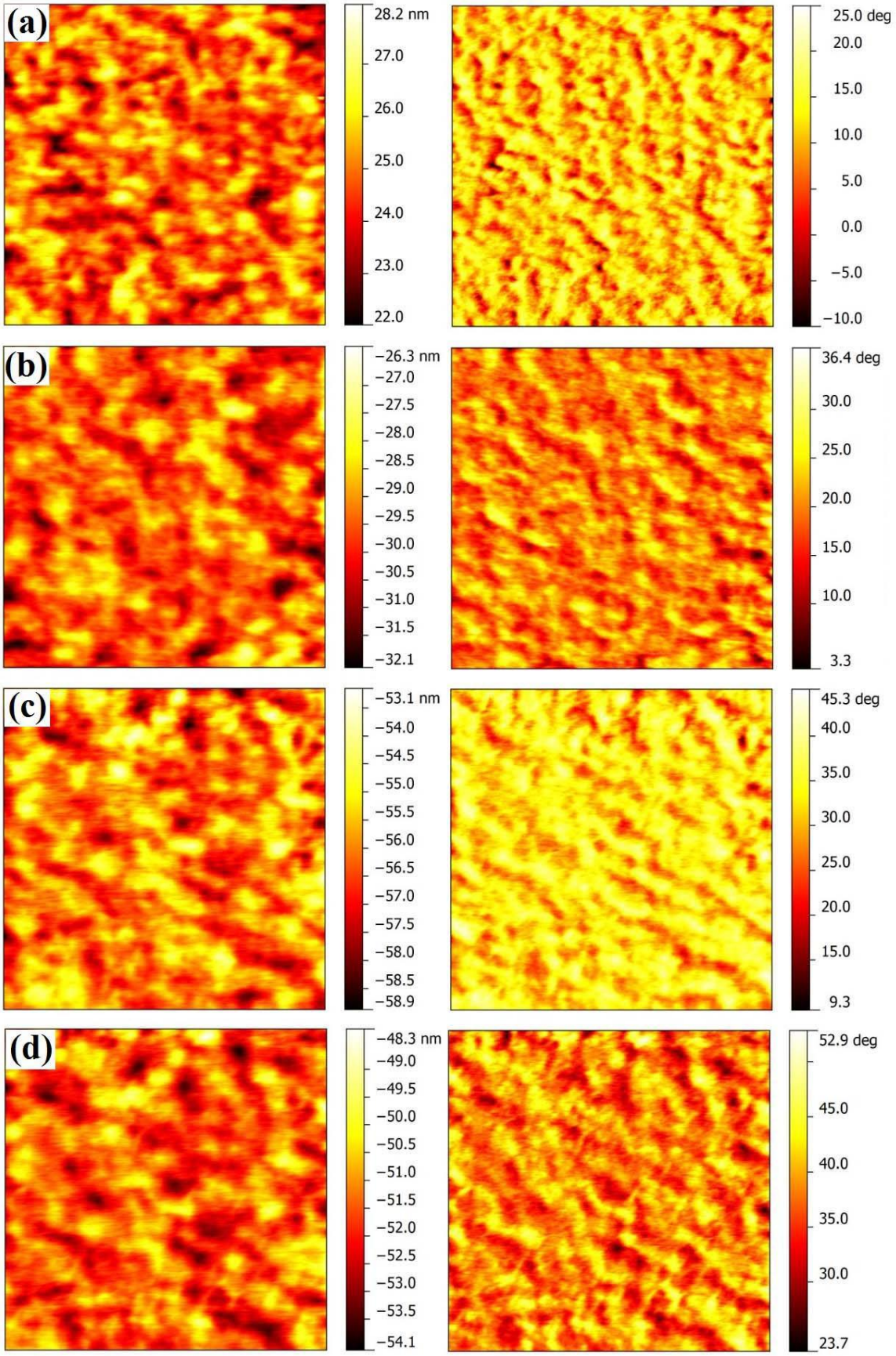
(a)
28.2 nm
27.0
26.0
25.0
24.0
23.0
22.0
25.0 deg
20.0
15.0
10.0
5.0
0.0
−5.0
−10.0
(b)
−26.3 nm
−27.0
−27.5
−28.0
−28.5
−29.0
−29.5
−30.0
−30.5
−31.0
−31.5
−32.1
36.4 deg
30.0
25.0
20.0
15.0
10.0
3.3
(c)
−53.1 nm
−54.0
−54.5
−55.0
−55.5
−56.0
−56.5
−57.0
−57.5
−58.0
−58.5
−58.9
45.3 deg
40.0
35.0
30.0
25.0
20.0
15.0
9.3
(d)
−48.3 nm
−49.0
−49.5
−50.0
−50.5
−51.0
−51.5
−52.0
−52.5
−53.0
−53.5
−54.1
52.9 deg
45.0
40.0
35.0
30.0
23.7

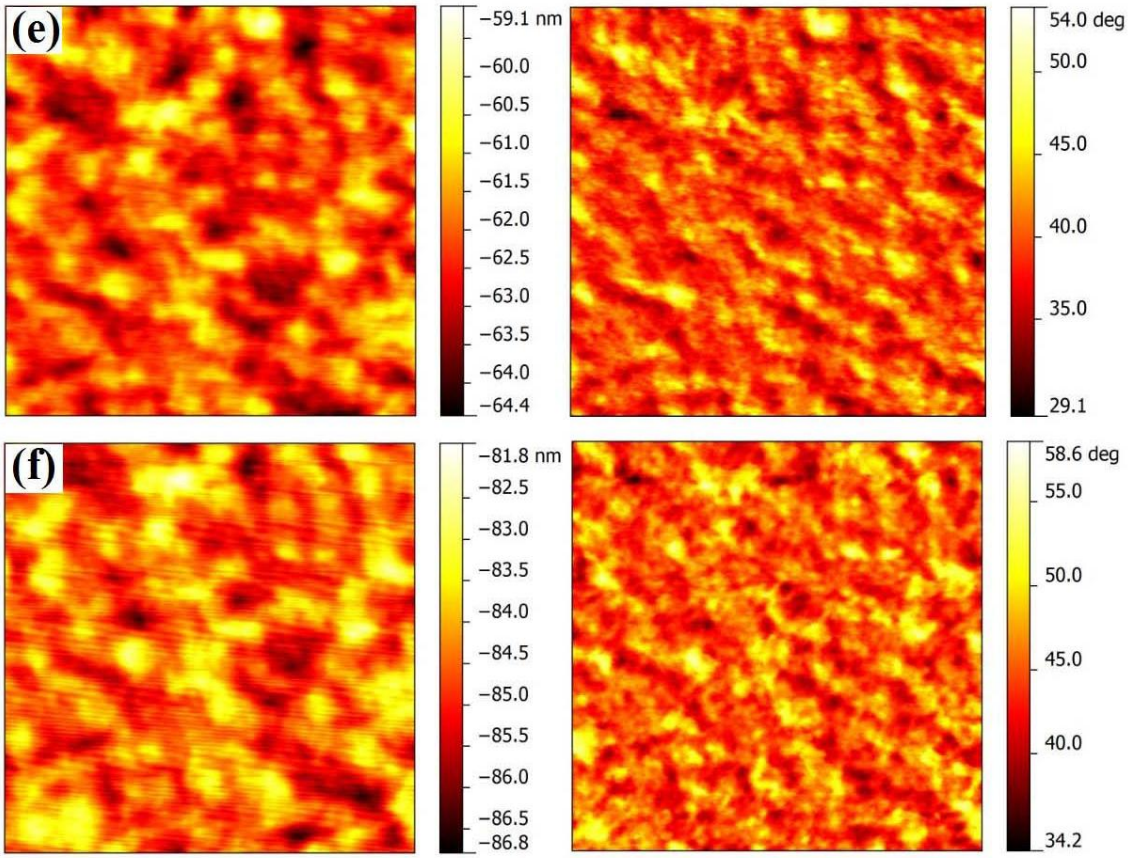

Figure 6.7 The height and phase DAFM images obtained from the $Zr_{70}Ni_{30}$ TFMG with the fixed A_0 (~21 nm) and the varying A_{sp}/A_0 ratios: (a) A_{sp}/A_0 =0.75, (b) A_{sp}/A_0 =0.63, (c) A_{sp}/A_0 =0.50, (d) A_{sp}/A_0 =0.38, (e) A_{sp}/A_0 =0.25, and (f) A_{sp}/A_0 =0.13. Note that each subfigure contains two images with the left to be the height and right to be the phase.

6.3.4 Surface Roughness Effect

Now let us discuss the surface roughness effect. Since no material surface can be 'perfectly' smooth, the total phase shift, $\Delta\phi$, measured from the AFM system is a convoluted result. In theory, we have $\Delta\phi = \Delta\phi_m + \Delta\phi_s$, where $\Delta\phi_m$ denotes the phase shift due to the material's response and $\Delta\phi_s$ due to surface roughness(P. J. James, M. Antognozzi et al. 2001). As already discussed in Refs. (P. J. James, M. Antognozzi et al. 2001; Y. Yang, J.F. Zeng et al. 2012), for a relatively

smooth surface which usually has a root-mean-square (RMS) roughness less than ~1nm, the surface roughness effect may be removed as long as we can still achieve a repulsive tip-surface interaction or obtain a positive $\Delta\phi$. However, if the material surface is too rough, it is also likely that the nature of the tip-surface interaction may be changed. If that occurs, it becomes extremely difficult to obtain a valid structural image of the TFMG. Figure 6.8a displays a height image of a 200-nm thick $Zr_{53}Cu_{29}Al_{12}Ni_6$ TFMG. It is evident that the film surface is very rough, consisting of grain-like patterns with sharp deep 'ditches'. Consequently, we obtain both positive and negative phase shifts even at a very low set-point ratio (~0.13) and high free amplitude (~21 nm), as seen in Fig. 6.8b. Noticing that these regions of negative phase shifts are spatially correlated very well with the 'ditches' (Figs. 6.8c-d), we may conclude that, when there is a sharp transition in the surface profile, for example, regions close to surface dust or scrapes, where the AFM tip cannot be allowed to make a physical contact with the surface, the position of the AFM tip will become unstable, jumping from the regime of a repulsive interaction to that of an attractive interaction. As a result, we can only acquire negative phase shifts therein and hence lose the structural contrast. This explains why TFMGs with an atomic-scale surface smoothness could serve as the good model material for the fundamental research on the structure of metallic-glasses (MGs) (Y.H. Liu, D. Wang et al. 2011; Y. Yang, J.F. Zeng et al. 2012).

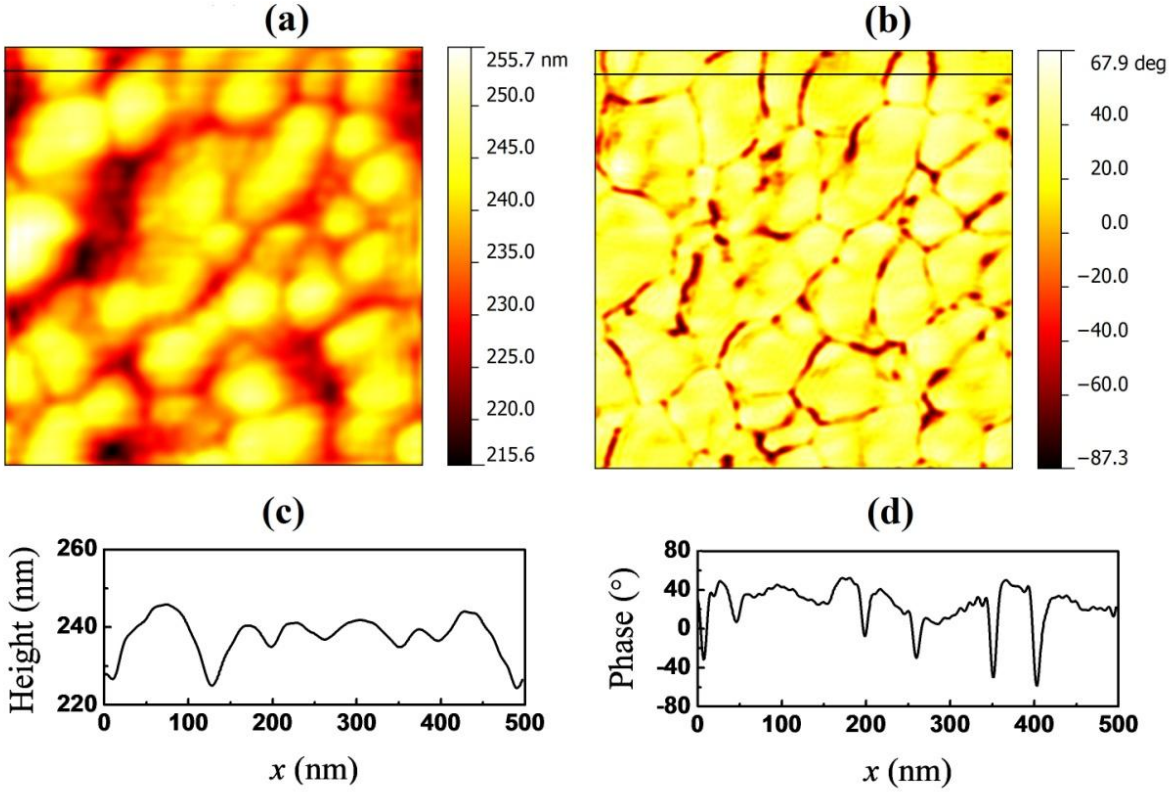

Figure 6.8 The (a) height and (b) phase images obtained from a 200-nm thick Zr-Cu-Al-Ni TFMG with a root-mean-square roughness of ~5nm at A_0 = 21 nm and A_{sp}/A_0=0.13 (the scan size = 500 nm). (c) and (d): the corresponding line-scan results obtained from the top section of (a) and (b) (black line).

6.3.5 Compositional Effect

Finally, it is important to show how the structural contrast, as derived from the nano-scale energy dissipation, could vary with the composition of the scanned surface. Figures 6.9a-c display the energy spectra obtained from the three samples using the same experimental set-up (A_0 = 21 nm, A_{sp}/A_0 = 0.13, k = 34.2 N/m, DLC-tip with a 1-nm radius). Note that all the selected scanning areas are very smooth and have a RMS roughness less than ~1nm. Evidently, under the same experimental condition, the $Zr_{70}Ni_{30}$ exhibits the largest peak broadening with an average energy

dissipation of ~15 eV/nm^2 (Fig. 6.9a). By comparison, the quaternary $Zr_{53}Cu_{29}Al_{12}Ni_6$ TFMG also causes an energy dissipation of ~15 eV/nm^2 on average; however, it exhibits a relatively sharper peak than the binary $Zr_{70}Ni_{30}$ TFMG, as shown in Fig. 6.9b. This implies that, after adding more elements into the alloy system, the atoms in the amorphous structure becomes well mixed and hence, the whole structure appears to be more homogeneous than before. In sharp contrast, the energy dissipation on the surface of the single-crystal Si is very low and extremely sharp (Fig. 6.9c). The average energy dissipation (~4 eV/nm^2) is only about 25% of that on the TFMG surfaces. Table 6.1 lists the key structural features that can extracted from the DAFM images (insets of Figs. 6.9a-c) for the three materials, from which it can be clearly seen that, in terms of energy absorption, the DAFM method enables the discrimination of the underlying structural heterogeneity in a quantitative manner.

Table 6.1 The RMS surface roughness, the average energy dissipation and the peak broadening quantified by the full width at half maximum, E_{FWHM}, of the energy spectra measured for the three samples.

Sample	$Zr_{70}Ni_{30}$ TFMG	$Zr_{53}Cu_{29}Al_{12}Ni_6$ TFMG	Single-crystal Si
RMS surface roughness (nm)	0.26	0.10	0.13
Average energy dissipation (eV/nm^2)	14.69	15.11	4.13
E_{FWHM} (eV/nm^2)	2.31	0.50	0.13

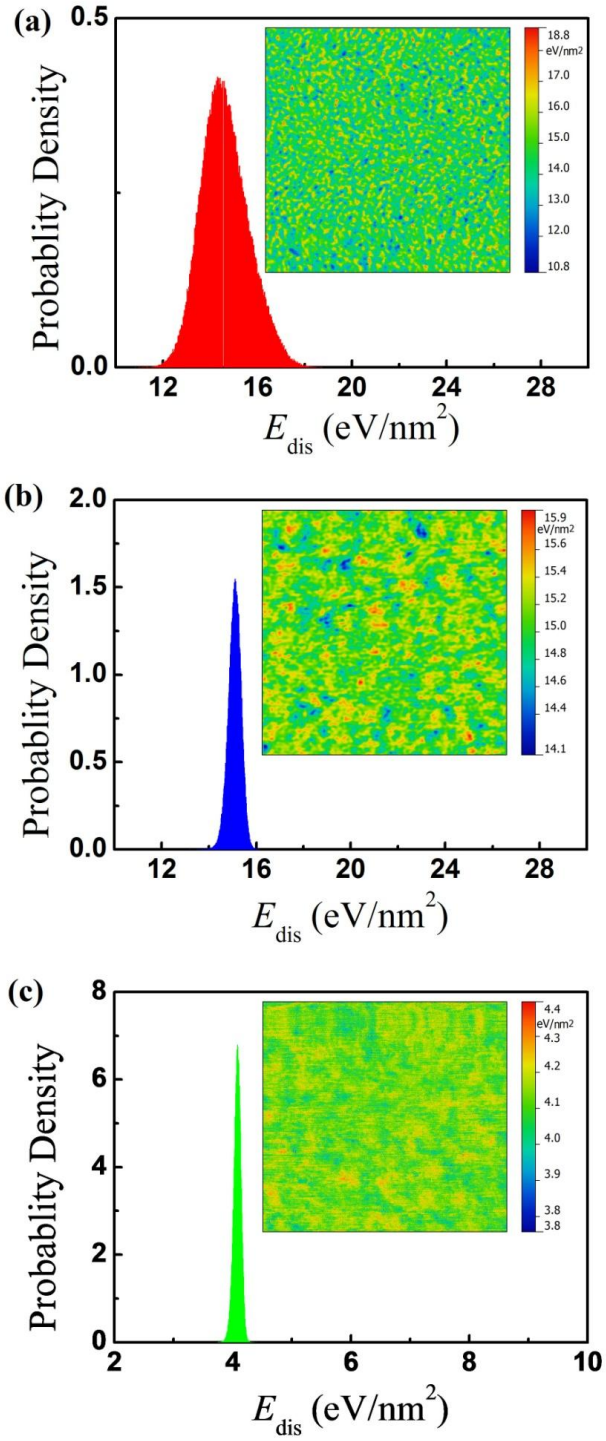

Figure 6.9 The energy dissipation spectra obtained for (a) the $Zr_{70}Ni_{30}$ TFMG, (b) the $Zr_{53}Cu_{29}Al_{12}Ni_6$ TFMG, and (c) the single-crystal Si at A_0 = 21 nm, A_{sp}/A_0=0.13 and k=34.2N/m. Note that the insets show the corresponding energy dissipation images with a scan size of 500 nm.

6.4 Concluding Remarks

To sum up, we performed a systematic study in this work on the use of the DAFM method for the structural imaging of the single-crystal Si, the $Zr_{70}Ni_{30}$ and $Zr_{53}Cu_{29}Al_{12}Ni_6$ TFMGs. The experimental results clearly show that, as compared to the single-crystal Si, the amorphous structures in the TFMGs are heterogeneous at the nano-scale, which can be revealed through their anelastic deformation. Here, it should be mentioned that, in principle, the repulsive tip-surface interaction results in an elastic stress field which spans across a much larger size underneath the surface than the tip-surface contact itself. Therefore, it should be always kept in mind that the structure contrast as seen in the DAFM images is a volume averaging result projected on a 2-D plane.

6.5 References

C. Fan, P.K. Liaw and C. T. Liu (2009). "Atomistic model of amorphous materials." Intermetallics **17**: 2.

D.B. Miracle (2004). "A structural model for metallic glasses." Nature Materials **3**: 6.

Dasgupta, R., S. Karmakar and I. Procaccia (2012). "Universality of the Plastic Instability in Strained Amorphous Solids." Phys Rev. Lett. **108**: 075701.

Fujita, T., Z. Wang, Y. Liu, H. Sheng, W. H. Wang and M. W. Chen (2012). "Low temperature uniform plastic deformation of metallic glasses during elastic iteration." Acta Mater. **60**: 3741-3747.

Garcia, R. (2010). Amplitude modulation atomic force microscopy, Wiley-VCH.

Garcia R and Perez R. (2002). "Dynamic atomic force microscopy methods." Surface Science Reports **47**: 105.

H. W. Sheng, W. K. L UO, F. M. Alamgir, J. M. Bai and E. Ma (2006). "Atomic Packing and Short-to-medium Range Order in Metallic Glasses." Nature **439**: 7.

J. C. Ye, C. T. Liu, Q. Wang and Y. Yang (2010). "Atomistic Free-Volume Zones and Inelastic Deformation of Metallic Glasses." Nature Materials **9**(8): 5.

J. C. Ye, J. P. Chu, Y. C. Chen, Q. Wang and Y. Yang (2012). "Hardness, yield strength, and plastic flow in thin film metallic-glass." Journal of Applied Physics **112**: 9.

J. P. Cleveland, B. Anczykowski, A. E. Schmid and V. B. Elings (1998). "Energy dissipation in tapping-mode atomic force microscopy." Appl. Phys. Lett. **72**(20): 3.

Javier Tamayo and Ricardo Garc á (1998). "Relationship between phase shift and energy dissipation in tapping-mode scanning force microscopy." Appl. Phys. Lett. **73**(20): 3.

Nicol ás F Mart´ınez and Ricardo Garc´ıa (2006). "Measuring phase shifts and energy dissipation with amplitude modulation atomic force microscopy." Nanotechnology **17**: 6.

P. J. James, M. Antognozzi, J. Tamayo, T. J. McMaster, J. M. Newton and M. J. Miles (2001). "Interpretation of Contrast in Tapping Mode AFM and Shear Force Microscopy. A Study of Nafion." Langmuir **17**: 12.

Q. Wang, C. T. Liu, Y. Yang, Y. D. Dong and J. Lu (2011). "Atomic-Scale Structural Evolution and Stability of Supercooled Liquid of a Zr-Based Bulk Metallic Glass." Physical Review Letters **106**: 4.

R. Garcia, C. J. Go ́mez, N. F. Martinez, S. Patil, C. Dietz and R. Magerle (2006). "Identification of Nanoscale Dissipation Processes by Dynamic Atomic Force Microscopy." Phys Rev. Lett. **97**: 4.

W. Dmowski, T. Iwashita, C.-P. Chuang, J. Almer and T. Egami (2010). "Elastic Heterogeneity in Metallic Glasses." Phys. Rev. Lett. **105**.

Y. Yang, J. F. Zeng, J. C. Ye and J. Lu (2010). "Structural inhomogeneity and anelastic deformation in metallic glasses revealed by spherical nanoindentation." Appl. Phys. Lett. **97**: 3.

Y. Yang, J.C. Ye, J. Lu, P.K. Liaw and C. T. Liu (2010). "Characteristic length scales governing plasticity/brittleness of bulk metallic glasses at ambient temperature." Appl. Phys. Lett. **96**(3): 011905.

Y. Yang, J.F. Zeng, A. Volland, J.J. Blandin, S. Gravier and C.T. Liu (2012). "Fractal growth of the dense-packing phase in annealed metallic glass imaged by high-resolution atomic force microscopy." Acta Materialia **60**: 13.

Y.H. Liu, D. Wang, K. Nakajima, W. Zhang, A. Hirata, T. Nishi, A. Inoue and M.W. Chen (2011). "Experimental Characterization of Nanoscale Mechanical Heterogeneity in a Metallic Glass." Physical Review Letters **106**: 17.

Zhiyong Suo, Xinghong Yang, Recep Avci, Laura Kellerman, David W. Pascual, Marc Fries and Andrew Steele (2007). "HEPES-stabilized encapsulation of Salmonella typhimutium." Langmuir **23**: 10.

7. Conclusions and Suggested Future Work

In my PhD study, I have attempted to reveal the structure-property relation of metallic glasses by investigating their micro-mechanical properties using spherical and Berkovich nanoindentation as well as micro-compression. I also uncovered the evolution process of atomic packing in an annealed Zr-Ni metallic glass thin film with the amplitude-modulation atomic force microscopy.

At the beginning, a simple spherical nanoindentation approach is used to reveal and characterize the anelastic behavior of metallic glasses (MGs) at ambient temperature. To explain these observed anelasticity, the Kelvin-Voigt rheological model and a general three-parameter rheological model were utilized to fit the experimental data. Each of these models can be linked with a certain topology of the atomic structure of MGs. As a result, the structural heterogeneity of MGs was 'captured' in our experiments, which entails the application of 'elastic' loadings at a very high loading rate before shear banding occurs. According to our experimental data, the structural heterogeneity in MGs can be viewed as a core-shell structural model, consisting of a 'soft' or viscous core and a 'hard' or elastic shell. Despite that the current experiments were conducted on the Zr-based MGs, the anelastic behaviors of Fe-based, La-based and other MGs can be investigated following the same spherical-indentation based approach. These future experiments may provide the critical evidence to distinguish different amorphous structures and, thus, further our understanding of the structure-property relation in MGs.

The second part of my work involves a systematic study of the micromechanical properties of Zr-based bulk metallic-glass (BMG) plates, which were plastically bent towards

different curvatures. First of all, the experimental data from nanoindentation across the plate width showed that, above a critical bending curvature, the local yield strengths or hardness on the compression side of the BMG plate could be altered by shear bands while those on the tension side remain almost invariant. In contrast, the measurements of Young's modulus remain nearly at a constant regardless of the indentation location. By comparison, the micro-pillar compression results show that the local elastic moduli and yield strengths of the BMG plates are kept more or less at a constant before and after plastic bending. This implies, at least for the BMG under study, the witnessed mechanical softening is caused more by residual stress than by the commonly conceived structural mechanism of 'defect' accumulation.

Based on our nanoindentation results, we conceived a core-shell type structural heterogeneity in MGs, but the direct experimental evidence is still lacking. For an experimental verification of the theoretical modeling, we employed a high-resolution atomic force microscopy (HRAFM) technique to reveal the nanoscale structural heterogeneity in a Zr-Ni MG thin film. In this work, we first annealed the MG thin film to various degrees in order to obtain different glassy structures with the same chemical composition. Through this HRAFM technique, we are able to uncover the annealing-induced fractal growth of the dense-packing phases in the binary MG thin film. In line with a two-dimensional diffusion limited aggregation process, the fractal dimension of our annealed MG thin film is around ~1.7. (Compared with previous findings, which showed the fractal dimension of ~2.3 in many types of BMGs, the cooling rate may play a vital role in the fractal growth of the dense-packing phases. In other words, as compared to a fast cooling rate, a slow cooling rate tends to promote the fractal growth of the dense-packing phases and enhances local structural heterogeneities.) We need to discuss this!

Although the direct evidence for a two-dimensional heterogeneous structure in the binary MG thin film has been obtained by the high-resolution AFM, additional studies are worthwhile for other MGs with different chemical compositions. Furthermore, revealing the structural evolution at a relatively high temperature (close to or even larger than a glass transition temperature) is a possible research direction that can yield valuable information on the glass formability of MGs.

Because of the limitation of our current instruments, our recent studies are only focused on the AM-AFM mode at ambient temperature with a slow scan speed. However, recent research work showed that local energy dissipation, adhesion and modulus can be mapped out simultaneously by using the peak force tapping technique, which entails fast data recording and a controllable force for each single pixel to be probed. In addition, the peak force tapping technique enables the study of the force-induced structural relaxation or rejuvenation in MGs, of which the outcome may provide compelling evidence to decode the structure-property relation of MGs.